

Euclid preparation

3D reconstruction of the cosmic web with simulated Euclid Deep spectroscopic samples

Euclid Collaboration: K. Kraljic¹, C. Laigle², M. Balogh^{3,4}, P. Jablonka⁵, U. Kuchner⁶, N. Malavasi⁷, F. Sarron^{8,9}, C. Pichon^{2,10}, G. De Lucia¹¹, M. Bethermin¹, F. Durret¹², M. Fumagalli^{11,13}, C. Gouin², M. Magliocchetti¹⁴, J. G. Sorce^{15,16}, O. Cucciati¹⁷, F. Fontanot^{11,18}, M. Hirschmann¹⁹, Y. Kang²⁰, M. Spinelli^{21,11,22}, N. Aghanim¹⁶, A. Amara²³, S. Andreon²⁴, N. Auricchio¹⁷, C. Baccigalupi^{18,11,25,26}, M. Baldi^{27,17,28}, S. Bardelli¹⁷, A. Biviano^{11,18}, E. Branchini^{29,30,24}, M. Brescia^{31,32}, J. Brinchmann^{33,34,35}, S. Camera^{36,37,38}, G. Cañas-Herrera^{39,40,41}, V. Capobianco³⁸, C. Carbone⁴², J. Carretero^{43,44}, R. Casas^{45,46}, S. Casas⁴⁷, F. J. Castander^{46,45}, M. Castellano⁴⁸, G. Castignani¹⁷, S. Cavuoti^{32,49}, K. C. Chambers⁵⁰, A. Cimatti⁵¹, C. Colodro-Conde⁵², G. Congedo⁵³, C. J. Conselice⁵⁴, L. Conversi^{55,56}, Y. Copin⁵⁷, F. Courbin^{58,59}, H. M. Courtois⁶⁰, A. Da Silva^{61,62}, H. Degaudenzi²⁰, S. de la Torre⁶³, H. Dole¹⁶, M. Douspis¹⁶, F. Dubath²⁰, C. A. J. Duncan^{53,54}, X. Dupac⁵⁶, S. Dusini⁶⁴, S. Escoffier⁶⁵, M. Farina¹⁴, R. Farinelli¹⁷, S. Ferriol⁵⁷, F. Finelli^{17,66}, P. Fosalba^{45,46}, N. Fourmanoit⁶⁵, M. Frailis¹¹, E. Franceschi¹⁷, M. Fumana⁴², S. Galeotta¹¹, K. George⁶⁷, W. Gillard⁶⁵, B. Gillis⁵³, C. Giocoli^{17,28}, J. Gracia-Carpio⁷, A. Grazian⁶⁸, F. Grupp^{7,67}, S. V. H. Haugan⁶⁹, W. Holmes⁷⁰, F. Hormuth⁷¹, A. Hornstrup^{72,73}, K. Jahnke⁷⁴, M. Jhabvala⁷⁵, B. Joachimi⁷⁶, E. Keihänen⁷⁷, S. Kermiche⁶⁵, A. Kiessling⁷⁰, M. Kilbinger⁷⁸, B. Kubik⁵⁷, M. Kümmel⁶⁷, M. Kunz⁷⁹, H. Kurki-Suonio^{80,81}, A. M. C. Le Brun⁸², S. Ligori³⁸, P. B. Lilje⁶⁹, V. Lindholm^{80,81}, I. Lloro⁸³, G. Mainetti⁸⁴, D. Maino^{85,42,86}, E. Maiorano¹⁷, O. Mansutti¹¹, S. Marcin⁸⁷, O. Marggraf⁸⁸, M. Martinelli^{48,89}, N. Martinet⁶³, F. Marulli^{90,17,28}, R. Massey⁹¹, S. Maurogordato²¹, E. Medinaceli¹⁷, S. Mei^{92,93}, Y. Mellier^{12,2}, M. Meneghetti^{17,28}, E. Merlin⁴⁸, G. Meylan⁵, A. Mora⁹⁴, M. Moresco^{90,17}, L. Moscardini^{90,17,28}, R. Nakajima⁸⁸, C. Neissner^{95,44}, S.-M. Niemi³⁹, C. Padilla⁹⁵, S. Paltani²⁰, F. Pasian¹¹, K. Pedersen⁹⁶, W. J. Percival^{4,3,97}, V. Pettorino³⁹, S. Pires⁷⁸, G. Polenta⁹⁸, M. Poncet⁹⁹, L. A. Popa¹⁰⁰, L. Pozzetti¹⁷, F. Raison⁷, R. Rebolo^{52,101,102}, A. Renzi^{103,64}, J. Rhodes⁷⁰, G. Riccio³², E. Romelli¹¹, M. Roncarelli¹⁷, C. Rosset⁹², E. Rossetti²⁷, R. Saglia^{67,7}, Z. Sakr^{104,105,106}, A. G. Sánchez⁷, D. Sapone¹⁰⁷, B. Sartoris^{67,11}, P. Schneider⁸⁸, T. Schrabback¹⁰⁸, M. Scudiego⁴², A. Secroun⁶⁵, E. Sefusatti^{11,18,25}, G. Seidel⁷⁴, M. Seiffert⁷⁰, S. Serrano^{45,109,46}, P. Simon⁸⁸, C. Sirignano^{103,64}, G. Sirri²⁸, L. Stanco⁶⁴, J. Steinwagner⁷, P. Tallada-Crespi^{43,44}, A. N. Taylor⁵³, H. I. Teplitz¹¹⁰, I. Tereno^{61,111}, N. Tessore⁷⁶, S. Toft^{112,113}, R. Toledo-Moreo¹¹⁴, F. Torradeflot^{44,43}, I. Tutusaus¹⁰⁵, L. Valenziano^{17,66}, J. Valiviita^{80,81}, T. Vassallo^{67,11}, G. Verdoes Kleijn¹¹⁵, A. Veropalumbo^{24,30,29}, D. Vibert⁶³, Y. Wang¹¹⁰, J. Weller^{67,7}, A. Zachei^{11,18}, G. Zamorani¹⁷, E. Zucca¹⁷, V. Allevato³², M. Ballardini^{116,117,17}, M. Bolzonella¹⁷, E. Bozzo²⁰, C. Burigana^{118,66}, R. Cabanac¹⁰⁵, M. Calabrese^{119,42}, A. Cappi^{17,21}, D. Di Ferdinando²⁸, J. A. Escartin Vigo⁷, L. Gabarra¹²⁰, W. G. Hartley²⁰, J. Martín-Fleitas¹²¹, S. Matthew⁵³, N. Mauri^{51,28}, R. B. Metcalf^{90,17}, A. A. Nucita^{122,123,124}, A. Pezzotta^{125,7}, M. Pöntinen⁸⁰, C. Porciani⁸⁸, I. Risso¹²⁶, V. Scottez^{12,127}, M. Sereno^{17,28}, M. Tenti²⁸, M. Viel^{18,11,26,25,128}, M. Wiesmann⁶⁹, Y. Akrami^{129,130}, S. Alvi¹¹⁶, I. T. Andika^{131,132}, S. Anselmi^{64,103,133}, M. Archidiacono^{85,86}, F. Atrio-Barandela¹³⁴, A. Balaguera-Antolinez^{52,135}, P. Bergamini^{85,17}, D. Bertacca^{103,68,64}, A. Blanchard¹⁰⁵, L. Blot^{136,82}, H. Böhringer^{7,137,138}, S. Borgani^{139,18,11,25,128}, M. L. Brown⁵⁴, S. Bruton¹⁴⁰, A. Calabro⁴⁸, B. Camacho Quevedo^{18,26,11,45,46}, F. Caro⁴⁸, C. S. Carvalho¹¹¹, T. Castro^{11,25,18,128}, R. Chary^{110,141}, F. Cogato^{90,17}, S. Conseil⁵⁷, T. Contini¹⁰⁵, A. R. Cooray¹⁴², S. Davini³⁰, F. De Paolis^{122,123,124}, G. Desprez¹¹⁵, A. Díaz-Sánchez¹⁴³, J. J. Diaz⁵², S. Di Domizio^{29,30}, J. M. Diego¹⁴⁴, P. Dimauro^{145,48}, P.-A. Duc¹, A. Enia^{27,17}, Y. Fang⁶⁷, A. G. Ferrari²⁸, A. Finoguenov⁸⁰, A. Fontana⁴⁸, A. Franco^{123,122,124}, K. Ganga⁹², J. García-Bellido¹²⁹, T. Gasparotto¹¹, R. Gavazzi^{63,2}, E. Gaztanaga^{46,45,146}, F. Giacomini²⁸, F. Gianotti¹⁷, G. Gozaliasl^{147,80}, M. Guidi^{27,17}, C. M. Gutierrez¹⁴⁸, A. Hall⁵³, H. Hildebrandt¹⁴⁹, J. Hjorth⁹⁶, S. Joudaki⁴³, J. J. E. Kajava^{150,151}, V. Kansal^{152,153}, D. Karagiannis^{116,22}, K. Kiiveri⁷⁷, C. C. Kirkpatrick⁷⁷, S. Kruk⁵⁶, M. Lattanzi¹¹⁷, V. Le Brun⁶³, J. Le Graet⁶⁵, L. Legrand^{154,155}, M. Lembo¹², F. Lepori¹⁵⁶, G. Leroy^{157,91}, G. F. Lesci^{90,17}, J. Lesgourgues⁴⁷,

L. Leuzzi¹⁷, T. I. Liaudat¹⁵⁸, S. J. Liu¹⁴, A. Loureiro^{159, 160}, J. Macias-Perez¹⁶¹, G. Maggio¹¹, E. A. Magnier⁵⁰, F. Mannucci¹⁶², R. Maoli^{163, 48}, C. J. A. P. Martins^{164, 33}, L. Maurin¹⁶, M. Miluzio^{56, 165}, P. Monaco^{139, 11, 25, 18}, C. Moretti^{26, 128, 11, 18, 25}, G. Morgante¹⁷, S. Nadathur¹⁴⁶, K. Naidoo¹⁴⁶, A. Navarro-Alsina⁸⁸, S. Nesseris¹²⁹, L. Pagano^{116, 117}, F. Passalacqua^{103, 64}, K. Paterson⁷⁴, L. Patrizii²⁸, A. Pisani⁶⁵, D. Potter¹⁵⁶, S. Quai^{90, 17}, M. Radovich⁶⁸, P.-F. Rocci¹⁶, G. Rodighiero^{103, 68}, S. Sacquegna^{122, 123, 124}, M. Sahlén¹⁶⁶, D. B. Sanders⁵⁰, A. Schneider¹⁵⁶, D. Sciotti^{48, 89}, E. Sellentin^{167, 41}, L. C. Smith¹⁶⁸, K. Tanidis¹²⁰, C. Tao⁶⁵, G. Testera³⁰, R. Teyssier¹⁶⁹, S. Tosi^{29, 30, 24}, A. Troja^{103, 64}, M. Tucci²⁰, C. Valieri²⁸, A. Venhola¹⁷⁰, D. Vergani¹⁷, G. Verza¹⁷¹, P. Vielzeuf⁶⁵, and N. A. Walton¹⁶⁸

(Affiliations can be found after the references)

ABSTRACT

The ongoing *Euclid* mission aims to measure spectroscopic redshifts for approximately two million galaxies using the H α line emission detected in near-infrared slitless spectroscopic data from the Euclid Deep Fields, leveraging both the red and blue grisms. These measurements will reach a flux limit of 5×10^{-17} erg cm $^{-2}$ s $^{-1}$ in the redshift range $0.4 < z < 1.8$, opening the door to numerous scientific investigations involving galaxy evolution, extending well beyond the mission's core objectives. The achieved H α luminosity depth will lead to a sufficiently high sampling, enabling the reconstruction of the large-scale galaxy environment. We assess the quality of the reconstruction of the galaxy cosmic web environment with the expected spectroscopic dataset in Euclid Deep Fields. The analysis is carried out on the Flagship and GAEA galaxy mock catalogues. The quality of the reconstruction is first evaluated using simple geometrical and topological statistics measured on the cosmic web network, namely the length of filaments, the area of walls, the volume of voids, and its connectivity and multiplicity. We then quantify how accurately gradients in galaxy properties with distance from filaments can be recovered. As expected, the small-scale redshift-space distortions, such as Fingers-of-God, have a strong impact on filament lengths and connectivity, but can be mitigated by compressing galaxy groups, identified with an anisotropic group finder, before skeleton extraction. The cosmic web reconstruction is biased when relying solely on H α emitters. This limitation can be mitigated by applying stellar mass weighting during the cosmic web reconstruction. However, this approach introduces non-trivial biases that need to be accounted for when comparing to theoretical predictions. Redshift uncertainties pose the greatest challenge in recovering the expected dependence of galaxy properties, though the well-established stellar mass transverse gradients towards filaments can still be observed, albeit with reduced significance.

Key words. Cosmology: observations – large-scale structure of the Universe – Galaxies: evolution

1. Introduction

Since the first observations in the late 1970s, revealing the existence of coherent patterns on scales larger than those of galaxy clusters, mapping the large-scale structure of the Universe has become possible thanks to large galaxy redshift surveys.

Early observations of the nearby Universe uncovering complex structures of interconnected superclusters (e.g., Davis et al. 1982), and enabling the unexpected discoveries of the first large cosmic voids (e.g., Kirshner et al. 1981), provided an initial hint that the spatial distribution of galaxies is highly inhomogeneous. It was quickly confirmed that this is a general feature of the large-scale distribution of galaxies, once observations from surveys covering wider areas on the sky started to become available. Beginning with the first redshift slices of the Center of Astrophysics redshift survey (CfA, de Lapparent et al. 1986), the progressively increasing depth and coverage offered by the next generations of surveys such as the Las Campanas Redshift Survey (LCRS, Shectman et al. 1996), the 2dF Galaxy Redshift Survey (2dFGRS, Colless et al. 2001), the Sloan Digital Sky Survey (SDSS, York et al. 2000; Abazajian et al. 2009, for DR7), the 6dF Galaxy Survey (6dFGS, Jones et al. 2004, 2009), and the Galaxy and Mass Assembly (GAMA, Driver et al. 2011) survey, allow us today to map the large-scale structure of the nearby Universe ($z \lesssim 0.3$) in unprecedented detail. These surveys revealed a cosmic landscape where galaxies were distributed within high-density peaks, intermediate-density filaments, and walls, which enclose low-density, nearly empty voids. This view has been extended up to $z \simeq 1$ by the VIMOS Public Extragalactic Redshift Survey (VIPERS, Guzzo et al. 2014) that encompasses a vol-

ume and galaxy sampling density comparable to those of spectroscopic surveys of the local Universe. Further improvement, in terms of significantly increased galaxy number density and depth compared to any of these surveys in the comparable redshift range, will be achieved by the ongoing Dark Energy Spectroscopic Instrument (DESI; DESI Collaboration et al. 2016) collaboration, which already collected high-confidence spectroscopic redshifts (McCullough et al. 2024) for more than ten million galaxies (DESI Collaboration et al. 2025).

Mapping the large-scale structure in three dimensions at even higher redshifts ($z \gtrsim 1$) is currently impossible with existing spectroscopic surveys, due to their rapidly decreasing completeness and sampling number density. For the time being, the density field at high redshifts is observationally accessible only through the tomographic reconstruction using the Lyman- α forest absorption of light from bright background sources, such as quasars, typically at $z \sim 2.5-3$ (e.g., Lee & White 2016; Ravoux et al. 2020). The redshift range $1 \lesssim z \lesssim 2$, near the peak epoch of star formation (e.g., Madau & Dickinson 2014) – the period when star formation in the Universe was at its highest – remains largely uncharted territory in understanding the co-evolution of galaxies and large-scale structures.

The web-like pattern observed in the distribution of galaxies, spanning scales from a few to over a hundred megaparsecs and revealed by large galaxy redshift surveys, is now understood within the framework of the so-called cosmic web (e.g., Klypin & Shandarin 1983, 1993; Bond et al. 1996). This structure connects observed galaxy clusters through a network of filaments, which arise from initial fluctuations in the primordial density field and are amplified by anisotropic gravitational collapse (Lynden-Bell 1964; Zel'dovich 1970) during later cosmic times. One of the most important features of this network is that

* e-mail: katarina.kraljic@astro.unistra.fr

it naturally sets the large-scale environment within which galaxies form and evolve. Since more than a decade now, interest has been shifting from extensively studied high-density regions, such as galaxy groups and clusters (e.g., [Davis & Geller 1976](#); [Dressler 1980](#); [Dressler et al. 1997](#); [Goto et al. 2003](#); [Blanton et al. 2003a](#); [Baldry et al. 2006](#); [Bamford et al. 2009](#); [Cucciati et al. 2010](#); [Burton et al. 2013](#); [Cucciati et al. 2017](#), and references therein), toward intermediate-density filaments and walls. These anisotropic large-scale environments seem to play a role in shaping at least some of the galaxy properties. Indeed, observational studies of the local and higher- z Universe ($z \lesssim 0.9$) have demonstrated that more massive and/or passive galaxies tend to reside closer to large-scale filaments compared to their lower-mass and/or star-forming counterparts (e.g., [Chen et al. 2017](#); [Kuutma et al. 2017](#); [Malavasi et al. 2017](#); [Kraljic et al. 2018](#); [Laigle et al. 2018](#); [Winkel et al. 2021](#)). This trend aligns qualitatively with results from large hydrodynamical simulations ([Kraljic et al. 2018](#); [Laigle et al. 2018](#); [Hasan et al. 2023](#); [Bullichi et al. 2024](#)) and with theoretical expectations ([Musso et al. 2018](#)), since the assembly history of galaxies encoded in a conditional excursion set is biased by the eigenvalues and eigenvectors of anisotropic tides.

The role of the cosmic web in modulating other galaxy properties, i.e. beyond stellar mass and star-formation activity, could also be modelled in this framework, but has so far only been explored at low redshifts ($z \lesssim 0.2$). In particular, it was found that after controlling for stellar mass, halo mass, or density, a clear signature of the impact of the cosmic filaments, walls, and nodes can be found for galaxy age, stellar metallicity, and element abundance ratio $[\alpha/\text{Fe}]$ ([Winkel et al. 2021](#)), gas-phase metallicity ([Donnan et al. 2022](#)), or $\text{H}\alpha$ fraction ([Kleiner et al. 2017](#); [Crone Odekon et al. 2018](#)). Another property of galaxies that shows a dependence on their large-scale environment, as expected by the tidal torque theory (for a review, see [Schäfer 2009](#) and [Codis et al. 2015](#) for the corresponding theory of constrained tidal torques near filaments), is their angular momentum (or spin) orientation, as identified in low- z observations (e.g. [Lee & Erdogdu 2007](#); [Tempel et al. 2013](#); [Tempel & Libeskind 2013](#); [Zhang et al. 2013, 2015](#); [Pahwa et al. 2016](#); [Krolewski et al. 2019](#); [Kraljic et al. 2021](#); [Barsanti et al. 2022](#)).

An alternative approach to studying the impact of the cosmic network on galaxy properties involves analysing its connectivity, i.e., the number of filaments connected to a given node of the cosmic web. This serves as a probe for the geometry of accretion at halo and galaxy scales ([Codis et al. 2018b](#)). When applied to SDSS data (see also, e.g., [Darragh Ford et al. 2019](#); [Sarrou et al. 2019](#); [Einasto et al. 2020, 2021](#); [Smith et al. 2023](#), for measurements on galaxy groups and cluster scales), more massive galaxies were found to exhibit higher connectivity ([Kraljic et al. 2020b](#)), a result consistent with theoretical predictions ([Codis et al. 2018b](#)). At fixed stellar mass, galaxy properties such as star-formation activity and morphology also show some dependence on connectivity: less star-forming and less rotation-supported galaxies tend to be more connected. This trend is qualitatively consistent with the findings of hydrodynamical simulations ([Kraljic et al. 2020b](#)).

Our understanding of how the anisotropic large-scale environment shapes galaxy properties remains observationally constrained to the low-redshift Universe ($z \lesssim 0.9$), with the majority of studies focusing on the nearby Universe ($z \lesssim 0.2$). However, ongoing and upcoming surveys, such as *Euclid* ([Laureijs et al. 2011](#)), the PFS (Prime Focus Spectrograph) Galaxy Evolution survey ([Greene et al. 2022](#)) at the Subaru Telescope, MOONRISE (the main GTO MOONS extra-galactic survey, [Maiolino et al. 2020](#)) at the Very Large Telescope (VLT), and Nancy Grace Roman Space Telescope (Roman; [Akeson et al. 2019](#)), will enable us to extend these analyses to redshifts between 1 and 2. This epoch is critical for unravelling the details of gas accretion onto galaxies, its conversion into stars, and the physical processes responsible for the quenching of star formation.

The ongoing *Euclid* survey ([Euclid Collaboration: Mellier et al. 2025](#)) will primarily focus on characterising the nature of dark energy and understanding the distribution of dark matter in the Universe. However, while *Euclid* has been specifically prepared to meet these core science objectives, it will also address a wide range of other scientific questions. This “by-product” research will be notably made possible by an extensive database of approximately two million galaxies observed over a 53 deg^2 area (the so-called *Euclid* Deep Fields, EDFs hereafter). This will, for the first time, enable detailed tracing of the large-scale environment of galaxies between redshifts 1 and 2, providing new insights into its connection to galaxy growth and properties.

In this paper, we examine to what extent the cosmic web environment of galaxies can be reconstructed using the upcoming spectroscopic dataset in EDFs. We use *Euclid* Deep mock galaxy catalogues to evaluate the quality of cosmic web reconstruction. Specifically, we investigate how factors such as the selection function, redshift-space distortions, and the anticipated uncertainties in redshift measurements affect the reconstruction quality. This analysis is conducted using various geometrical and topological properties of the cosmic web. We also examine how accurately stellar-mass gradients toward cosmic web filaments can be recovered. A key objective of this study is to provide practical guidelines for cosmic web reconstruction using the EDF dataset. While this paper focuses on the three-dimensional reconstruction of the cosmic web, its two-dimensional counterpart is discussed in [Euclid Collaboration: Malavasi et al. \(2025\)](#), and the reconstruction of cluster-scale filaments is addressed in [Sarrou et al. \(in prep.\)](#). In the present approach, the skeleton is used as an effective summary statistics. An alternative is simulation-based inference via forward modelling, which aims to match the full data set to mocks without constructing specific estimators (e.g., [Cranmer et al. 2020](#)). These methods have recently gained some traction given the available computing power (e.g., [Angulo et al. 2021](#); [Kobayashi et al. 2022](#); [Hou et al. 2024](#)). Similarly, alternative approaches exist for the reconstruction of the large-scale environment (see [Libeskind et al. 2018](#), for a detailed comparison of different estimators).

The paper is organised as follows. Section 2 presents the *Euclid* Deep Survey and simulated galaxy catalogues, together with methods used to create mock data and extract the cosmic web. Section 3 quantifies the quality of the cosmic web reconstruction and its ability to recover the stellar-mass gradients with respect to cosmic filaments. Section 4 provides guidelines for cosmic web reconstruction with the *Euclid* Deep dataset, outlines possible science cases, and discusses possible synergies with other surveys. Section 5 summarises the key results and concludes. Finally, Appendix A investigates the impact of the selection function of galaxies and reduced sampling on the distribution of filament lengths, while Appendix B focuses on their impact on connectivity and multiplicity. Appendix C complements the analysis of stellar mass gradients.

2. Data

2.1. The Euclid Deep Survey (EDS)

The EDS is described in [Euclid Collaboration: Mellier et al. \(2025\)](#), but we summarise its main characteristics below. In brief, it includes three non-contiguous fields: the EDF North (EDF-N, 20 deg^2), the EDF Fornax (EDF-F, 10 deg^2) and the EDF South (EDF-S, 23 deg^2). All together, they cover 53 deg^2 and will reach a 5σ point source depth of at least two magnitudes deeper than the Euclid Wide Survey (EWS, [Euclid Collaboration: Scaramella et al. 2022](#)), i.e. ~ 28.2 AB mag in I_{E} and 26.4 AB mag in Y_{E} , J_{E} , and H_{E} . These fields will be complemented by deep photometry from the Cosmic DAWN survey in the UV, optical, and IR that will be very valuable for deriving reliable masses and star-formation histories for the observed galaxies ([Euclid Collaboration: McPartland et al. 2025](#); [Euclid Collaboration: Zalesky et al. 2025](#)). In addition, the Euclid Auxiliary Fields (EAF), designed to serve the calibration of the VIS and NISP instruments, will reach an almost similar depth to the EDF, with the special case of the self-calibration field which will be ultra-deep (29.4 AB mag in I_{E} and 27.7 AB mag in Y_{E} , J_{E} , and H_{E} in 2.5 deg^2). The EAF will cover a total of 9 deg^2 distributed over seven fields, all of them already having deep multi-wavelength coverage in a large number of bands covering the whole electromagnetic spectrum. The forecasts presented in this paper are relevant for both the EDF and at least the three largest EAF (COSMOS, SXDS, and the self-calibration field).

On the spectroscopic side, the red grisms will allow the detection of $\text{H}\alpha$ emitters over $0.84 < z < 1.88$ and will operate over the full survey (EWS, EDS, and EAF). The blue grism will operate only on the EDF and EAF, and will allow the $\text{H}\alpha$ detection down to $z = 0.41$. Since the forecasts presented in the present work concern the EDS, we adopt the redshift range $0.4 < z < 1.8$ throughout this paper. The expected flux limit in the EDFs is $5 \times 10^{-17} \text{ erg cm}^{-2} \text{ s}^{-1}$ for sources with $\text{S/N} > 3.5$. These objects virtually all meet the expected photometric magnitude limits of the EDS.

2.2. Performances of the EDS for cosmic web mapping

Redshift accuracy: The red grisms have a resolving power of $\mathcal{R}_{\text{RG}} \geq 480$ for sources with $0.5'$ diameter, and the blue grism has a resolving power of $\mathcal{R}_{\text{BG}} \geq 400$. The expected redshift accuracy is $\sigma(z) < 0.001(1+z)$, confirmed by the analysis using the first *Euclid* Quick Data Release (Q1) ([Euclid Collaboration: Le Brun et al. 2025](#)).

Completeness and purity: Slitless spectroscopy is essentially dispersed imaging. The features of the various overlapping spectra must be separated from each other by taking advantage of the fact that the same field is observed with several dispersion angles. A complex extraction and decontamination process produces 1D spectra, performed with the OU-SIR unit ([Euclid Collaboration: Copin et al. 2025](#)). The probability distribution function of the redshift is then determined from these spectra using a spectral template fitting algorithm, performed by the OU-SPE unit ([Euclid Collaboration: Le Brun et al. 2025](#)). The algorithm returns the most probable redshift as the first solution, which is then used for cosmic web reconstruction. In addition, a reliability score is assigned to each galaxy and a threshold is determined to

obtain a good compromise between the completeness and purity of the galaxy sample¹.

This threshold will exclude a significant fraction of galaxies above the flux limit, leading to incompleteness and a higher flux cut. For the cosmic web reconstruction, we will need high purity, and thus a very high OSU-SPE reliability cut. Similarly to [Hamaus et al. \(2022\)](#), we assume that it will lead to a completeness of 60% and a higher flux limit (see Sect. 2.3.3). This high purity will in turn allow us to neglect the existence of catastrophic redshift failures in our current analysis.

2.3. Mock catalogues

In order to make forecasts about the quality of the cosmic web reconstruction with the upcoming Euclid data, we rely on two simulated sets, the Euclid Flagship 2 and the GAEA simulations.

2.3.1. The Flagship galaxy mock catalogues

The Euclid Flagship Simulation (Flagship, hereafter) is described in great detail in [Euclid Collaboration: Castander et al. \(2025\)](#). Here, we only summarise its main features.

The Flagship lightcone, produced on the fly out to $z = 3$, is based on an N -body dark matter simulation of four trillion dark matter particles in a periodic box of $3600 h^{-1} \text{ Mpc}$ on a side, leading to the particle mass resolution of $\sim 10^9 h^{-1} M_{\odot}$. The simulation was performed using the code PKDGRAV3 ([Potter & Stadel 2016](#)), with cosmological parameters $h = 0.67$, $\Omega_{\text{m}} = 0.319$, $\Omega_{\text{b}} = 0.049$, $n_{\text{s}} = 0.96$, $A_{\text{s}} = 2.1 \times 10^{-9}$.

Dark matter halos, identified with the ROCKSTAR halo finder ([Behroozi et al. 2013](#)), were populated by galaxies using a combination of halo occupation distribution (HOD) and abundance matching (AM) techniques, satisfying some of the observed relations between galaxy properties. Following the HOD prescription, each halo was assigned a central galaxy and a number of satellites depending on the halo mass, reproducing observational constraints of galaxy clustering in the local Universe ([Zehavi et al. 2011](#)). Luminosities were assigned to galaxies by performing abundance matching between the halo mass function and the galaxy luminosity function, calibrated on the local observations ([Blanton et al. 2003b, 2005](#)) in a way to match the observed clustering of galaxies as a function of color ([Zehavi et al. 2011](#)).

The star-formation rate (SFR) was computed from the rest-frame ultraviolet luminosity, following the [Kennicutt \(1998\)](#) relation for a Chabrier initial mass function (IMF; [Chabrier 2003](#)). The stellar mass was computed from the galaxy luminosity and the stellar mass-to-luminosity ratio. The $\text{H}\alpha$ line flux was computed from the SFR using the [Kennicutt \(1998\)](#) relation adapted to the [Chabrier \(2003\)](#) IMF, using the un-extincted ultraviolet absolute magnitude. The dust extinguished $\text{H}\alpha$ flux was then computed following [Calzetti et al. \(2000\)](#) and [Saito et al. \(2020\)](#). Finally, the resulting $\text{H}\alpha$ flux distribution was calibrated to the empirical models of [Pozzetti et al. \(2016\)](#), namely model 1 and model 3 (named m1 and m3, hereafter).

Validation of the Flagship galaxy catalogue by comparing it with observations is presented in [Euclid Collaboration: Castander et al. \(2025\)](#), showing good agreement for many galaxy properties, distributions, and relations. Among them, the stellar

¹ Completeness is defined as the fraction of objects recovered with a correct redshift from a full sample above a certain intrinsic flux limit and in a certain redshift range, while purity is the fraction of correctly measured redshifts in the recovered sample.

mass function and the SFR-stellar mass relation show good consistency when compared to observational data up to $z \sim 3$.

The full galaxy catalogue covers one octant of the sky ($\sim 5157 \text{ deg}^2$) centred at approximately the North Galactic Pole ($145 \text{ deg} < \text{RA} < 235 \text{ deg}$, $0 \text{ deg} < \text{Dec} < 90 \text{ deg}$), and samples a redshift range $0 < z < 3$. However, only a limited area ($150 \text{ deg} < \text{RA} < 155 \text{ deg}$, $5 \text{ deg} < \text{Dec} < 10 \text{ deg}$), with no magnitude or line flux cut, can be used to simulate the EDF (see Sect. 2.3.3). Flagship catalogues were accessed through Cosmo-Hub (Carretero et al. 2017; Tallada et al. 2020).

2.3.2. The GAEA lightcone

GAEA (Galaxy Evolution and Assembly)² is a semi-analytic model (see e.g., De Lucia et al. 2014; Hirschmann et al. 2016; Fontanot et al. 2017) run on the Millennium simulation (Springel et al. 2005) containing 2160^3 dark matter particles in a periodic box of $500 h^{-1} \text{ Mpc}$ on one side, leading to a particle mass resolution of $8.6 \times 10^8 h^{-1} M_\odot$. The Millennium simulation was performed using the code GADGET (Springel et al. 2001) with cosmological parameters $h = 0.73$, $\Omega_m = 0.25$, $\Omega_b = 0.045$, $n_s = 1$, $\sigma_8 = 0.9$. From this simulation, a lightcone was created following Zoldan et al. (2017).

The GAEA semi-analytic model traces the evolution of galaxy populations inside DM halos by self-consistently treating gas, metal and energy recycling, as well as chemical enrichment, using physically or observationally motivated prescriptions. Two versions of this model have been implemented. These are described in Hirschmann et al. (2016) and Fontanot et al. (2020), and named respectively ECLH and ECLQ in the following. One of the major differences between these two models is an improved prescription for AGN feedback in ECLQ. While both ECLH and ECLQ models include radio-mode AGN feedback, ECLQ also includes a quasar-driven wind component, following an improved modelling of cold-gas accretion onto the supermassive black hole, based on both analytic approaches and high-resolution simulations.

To compute the dust-attenuated $\text{H}\alpha$ flux, the non-attenuated $\text{H}\alpha$ luminosity was derived from the SFR following the Kennicutt et al. (1994) relation (rescaled to follow the Chabrier 2003 IMF). The obtained $\text{H}\alpha$ flux has then been attenuated by dust following the dust attenuation curve of Calzetti et al. (2000).

GAEA was shown to well reproduce a number of observations, such as the evolution of the galaxy stellar mass function and the cosmic SFR density up to $z \sim 7$ (Fontanot et al. 2017), or the evolution of the stellar mass-gas metallicity relation up to $z \sim 2$ (Hirschmann et al. 2016).

The full galaxy catalogue covers a region on the plane of the sky with a diameter of 5.27 deg ($\sim 22 \text{ deg}^2$), samples a redshift range $0 < z < 4$, and includes all galaxies with magnitude $H \leq 25$ (i.e. deep enough to allow for the construction of EDF mocks; see Sect. 2.3.3).

2.3.3. Mocking the EDS

To mimic the EDFs, we select from the full Flagship volume the $\sim 25 \text{ deg}^2$ region that has no magnitude or line flux cut, in the redshift range $0.4 < z < 1.8$. The same redshift selection is applied to the GAEA galaxy catalogues, having comparable sky coverage.

Flux limit: In this work, we select all galaxies with an $\text{H}\alpha$ flux limit of $6 \times 10^{-17} \text{ erg cm}^{-2} \text{ s}^{-1}$, which is a more conservative threshold compared to the predicted limit (see Sect. 2.1). This selection ensures that, as expected, all objects satisfy the EDS photometric magnitude limits. To assess the impact of galaxy selection on the quality of cosmic web reconstruction, we also consider a stellar mass-limited sample of galaxies for each mock. In order to keep the same total number density, we select from each mock, ordered in decreasing stellar mass, the same number of galaxies as in its flux-limited counterpart. The resulting stellar mass limits are $10^{9.5} M_\odot$, $10^{9.8} M_\odot$, for the Flagship m1 and m3 models, respectively, and $10^{9.8} M_\odot$ for both GAEA models. The M_* - and $\text{H}\alpha$ flux-limited samples therefore contain by construction different populations of galaxies. $\text{H}\alpha$ flux-limited samples have fewer satellites (and therefore more centrals), and miss an important fraction of quiescent massive galaxies compared to M_* -limited catalogues.

In the following, flux-limited catalogues are denoted \mathcal{D} , while mass-limited catalogues are denoted with ‘ M_* ’ in the subscript, i.e. \mathcal{D}_{M_*} .

Completeness: To mimic the expected sample completeness of 60 % due to observational effects (see Sect. 2.2), we randomly discard 40 % of our galaxies (as done in e.g., Hamaus et al. 2022). We note that the incompleteness will not be truly random. However, since the incompleteness has not been characterised in detail against parameters, such as the local projected density, a more precise model remains currently unavailable. In the following, the corresponding catalogues are denoted with ‘60 %’ in the subscript, for example, $\mathcal{D}_{60\%}$.

Redshift uncertainties: To model the redshift uncertainties associated with Euclid measurement, we perturb galaxy redshifts, as taken from the mocks, using a Gaussian redshift-dependent error with an RMS of $\sigma_z = 0.001(1+z)$. For each model, we make five realisations and the corresponding catalogues are denoted with ‘noise’ in the subscript in the following, for example, $\mathcal{D}_{\text{noise}}$.

Fiducial realisation: Applying all these constraints to the selection of galaxies, i.e. $\text{H}\alpha$ flux limit of $6 \times 10^{-17} \text{ erg cm}^{-2} \text{ s}^{-1}$, redshift uncertainty $\sigma_z = 0.001(1+z)$, and completeness of 60%, leads to fiducial realisations mimicking the EDFs, denoted in the following $\mathcal{D}_{\text{noise},60\%}$.

2.3.4. Qualitative assessment of the mocks

Being based on different N -body simulations and using different methods to assign galaxies to dark matter halos and to compute their properties, the Flagship and GAEA simulations are expected to provide different predictions in terms of galaxy distribution, galaxy clustering and their dependence on stellar mass or $\text{H}\alpha$ flux. In this section, we provide a qualitative assessment of the mock catalogues without additional observational biases, i.e. using true redshifts and a full sampling, by focusing on their mean intergalactic separation, stellar mass and $\text{H}\alpha$ luminosity functions, main sequence and $\text{H}\alpha$ -dependent galaxy clustering.

Mean intergalactic separation: The mean number density of $\text{H}\alpha$ -selected galaxies across the entire redshift range is higher in GAEA compared to Flagship, $1.2 \times 10^{-2} (h^{-1} \text{ Mpc})^{-3}$ and

² <https://sites.google.com/inaf.it/gaea/>

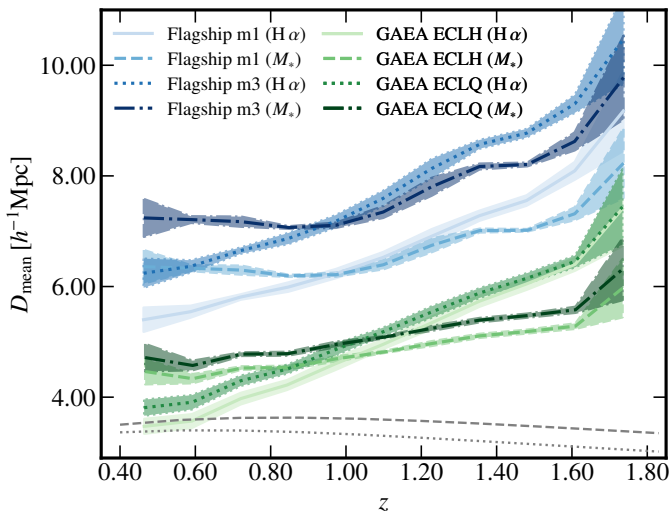


Fig. 1. Mean intergalactic separation in Flagship (blue colours) and GAEA (green colours) simulations for all considered models (m1 and m3 for Flagship, ECLH and ECLQ for GAEA). For each model, the fiducial galaxy selection based on the $H\alpha$ flux ($H\alpha$) is compared to the stellar mass-based selection (M_*). Shaded regions correspond to the standard deviation across five mocks for each model. Grey dotted and dashed lines represent the corresponding redshift uncertainties converted into distances for Flagship and GAEA simulations, respectively. GAEA models show smaller differences between each other and compared to the Flagship simulation models, in particular for the $H\alpha$ selection of galaxies. Above $z \sim 0.9$, the $H\alpha$ selection follows more closely the selection based on stellar mass for the Flagship simulation, with respect to GAEA.

$9.7 \times 10^{-3} (h^{-1} \text{Mpc})^{-3}$ for ECLH and ECLQ GAEA models, respectively, and $3.9 \times 10^{-3} (h^{-1} \text{Mpc})^{-3}$ and $2.5 \times 10^{-3} (h^{-1} \text{Mpc})^{-3}$ for the two Flagship models m1 and m3, respectively. This translates into the smaller mean intergalactic separations for GAEA compared to Flagship, shown in Fig. 1. The two GAEA models show very little difference in mean intergalactic separations in particular when galaxy selection is based on the $H\alpha$ flux and above $z \sim 0.9$. The two Flagship models show larger differences in the mean intergalactic separation compared to GAEA, regardless of galaxy selection, which is roughly constant across the entire redshift range considered in this work. For comparison, the mean galaxy separations are shown also for the M_* -limited samples for all mocks. As expected, they show a flatter redshift dependence compared to $H\alpha$ galaxy selection for all the mocks, especially at redshifts below $z \sim 1.4$. We anticipate that the expected large redshift uncertainties (see the dotted lines in Fig. 1) are going to play a major role in reducing the quality of the cosmic web reconstruction.

Stellar mass and $H\alpha$ luminosity functions: The stellar mass (SMF) and $H\alpha$ luminosity functions (LF) for all Flagship and GAEA models are displayed in Fig. 2 in three different redshift bins. To highlight the impact of $H\alpha$ flux selection on these observables, we also show the results for samples without any $H\alpha$ flux limit. The SMFs of Flagship and GAEA models are compared with the COSMOS2020 observational dataset (Shutov et al. 2022), while for the LFs the models are compared to data from the Emission Line COSMOS catalogue (Saito et al. 2020), HST-NICMOS (Shim et al. 2009), HST WISP (Colbert et al. 2013), and HiZELS (Sobral et al. 2013).

Overall, the SMFs of Flagship and GAEA galaxies without the $H\alpha$ flux limit (dashed lines) agree well with the observational measurements in all redshift bins.³ This is not surprising, particularly for GAEA, since the SMF was used to calibrate their models.

The application of an $H\alpha$ flux limit translates non-trivially to the change in the SMF in a model-dependent way. The SMFs for the $H\alpha$ flux-limited samples show a reduced amplitude at all stellar masses for all models except GAEA ECLH for which the SMFs overlap at the high-mass end (the stellar mass at which the deviation occurs depends on the redshift). Overall, the SMFs follow a qualitatively similar trend for all models. The steep increase at the high-mass end is followed by a shallower slope at intermediate masses and a downturn of the SMF at low masses. The stellar mass at which the SMFs start to decrease at the low-mass end increases with increasing redshift and depends on the model. For Flagship it corresponds to $\sim 10^{9.5} M_\odot$, $10^{9.5} M_\odot$, and $10^{9.65} M_\odot$ in the three increasing redshift bins, while for GAEA the corresponding masses are slightly higher, particularly in the two highest redshift bins ($10^{9.75} M_\odot$ and $10^{10.15} M_\odot$).

The $H\alpha$ LF of observed galaxies at low redshifts ($0.4 < z < 0.9$; Colbert et al. 2013; Saito et al. 2020) is well reproduced by Flagship, the model m3 in particular. This is expected, given that the LF of galaxies was among the observables used to calibrate the Flagship mocks. GAEA mocks reproduce reasonably well the LF of galaxies at the faint end, whereas they over-predict the number of observed galaxies at the bright end. At intermediate redshifts ($0.9 < z < 1.3$), the $H\alpha$ LF of the observed galaxies (Shim et al. 2009; Colbert et al. 2013) lies well within the range spanned by the four galaxy mocks, making them a fairly good representation of galaxies at luminosities $L_{H\alpha} \gtrsim 10^{41.8} \text{ erg s}^{-1}$, corresponding to the $H\alpha$ flux limit of EDS at $z = 1.3$. At higher redshifts ($1.3 < z < 1.7$), the $H\alpha$ LFs of all mocks under-predict observations (Colbert et al. 2013; Saito et al. 2020) below $L_{H\alpha} \sim 10^{42.8} \text{ erg s}^{-1}$, while at higher luminosities, most models agree well with observations. GAEA in particular reproduces well the observed LF at the bright end in spite of the fact that this observable has not been used to calibrate the models.

We note that the drop (down turn) of the LF at the faint end for the $H\alpha$ flux-limited sample is a consequence of the relatively large width of the redshift bins. The luminosity at which the two LFs (for full and $H\alpha$ flux-limited samples) start to deviate corresponds to the $H\alpha$ flux limit of the upper bound of each redshift bin. This corresponds to the $H\alpha$ luminosity of $10^{40.51} \text{ erg s}^{-1}$, $10^{41.37} \text{ erg s}^{-1}$, $10^{41.77} \text{ erg s}^{-1}$, and $10^{42.07} \text{ erg s}^{-1}$, at redshifts 0.4, 0.9, 1.3, and 1.7, respectively.

Main sequence: Figure 3 shows the relation between the stellar mass and star-formation rate of galaxies in the Flagship and GAEA simulations in two redshift bins, $0.4 < z < 0.9$ (top panels) and $0.9 < z < 1.8$ (bottom panels). We only show models m3 and ECLH, but the results are similar for m1 and ECLQ. All galaxy mocks recover the expected correlation between the SFR and $H\alpha$ luminosity. Comparison with the compilation of observational data from Popesso et al. (2023) confirms that, in general, there is good agreement between observations and simulations. The shape of the star-forming main sequence for $H\alpha$ flux-limited sample (solid black lines) is better reproduced in GAEA compared to Flagship across a wide range of stellar masses in

³ We note that we have not transformed the stellar masses of mock galaxies to units of the Hubble constant used in the observed galaxy catalogues.

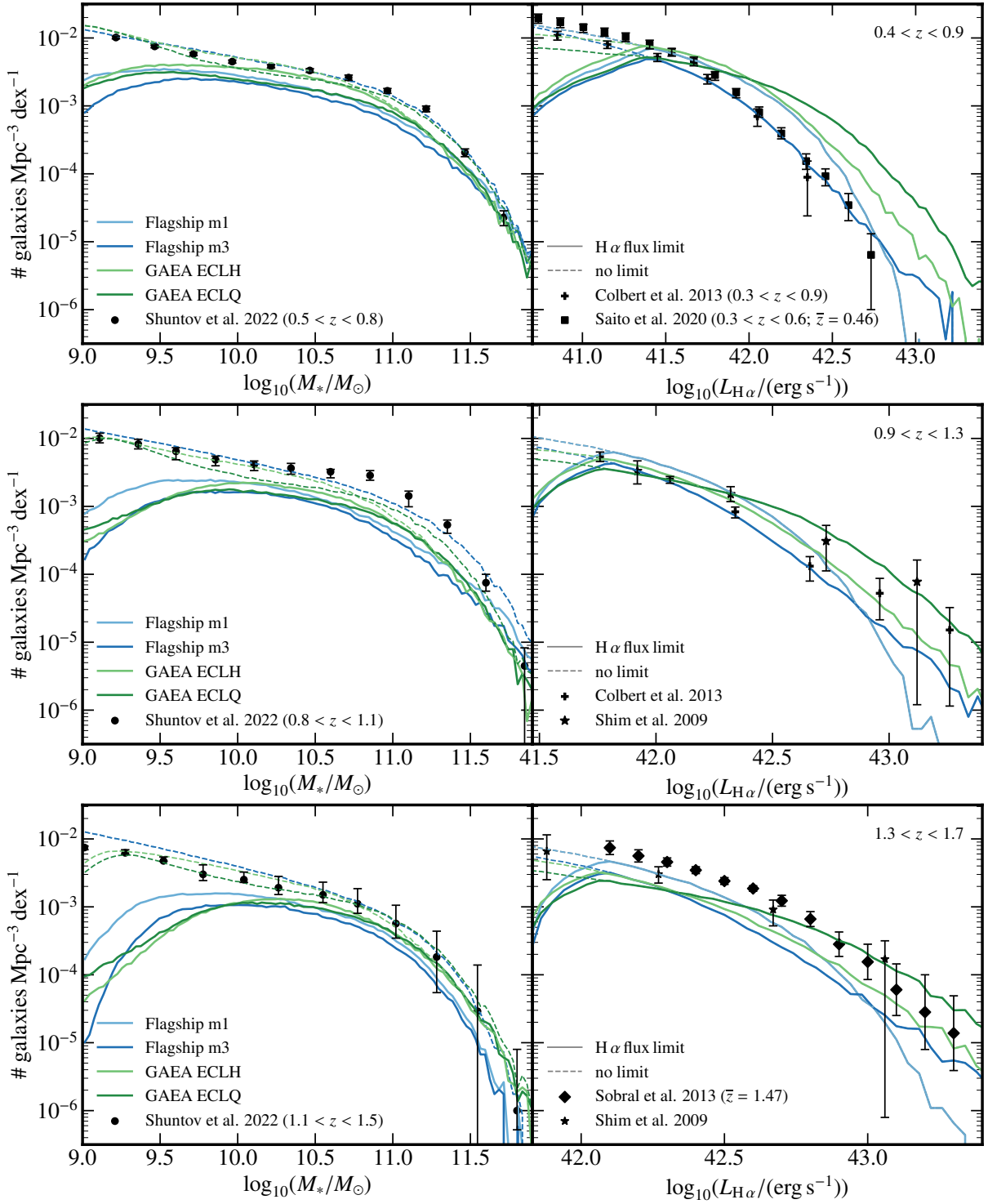


Fig. 2. Stellar mass (left) and H α luminosity functions (right) in three redshift bins, $0.4 < z < 0.9$ (top), $0.9 < z < 1.3$ (middle), and $1.3 < z < 1.7$ (bottom), in all models considered in this work for H α flux limited samples (coloured solid lines) and for samples without any limit (coloured dashed lines). Black symbols correspond to observational data at these redshifts, COSMOS2020 (Shuntov et al. 2022) for stellar mass functions and the Emission Line COSMOS catalogue (Saito et al. 2020), HST-NICMOS (Shim et al. 2009), HST WISP (Colbert et al. 2013), and HiZELS (Sobral et al. 2013) for H α luminosity functions.

both redshift bins. However, both models show a shift compared to the observed main sequence. In GAEA, galaxies lie below, whereas in Flagship, they tend to be above the observed relation.

Galaxy clustering: Figure 4 shows the two-point correlation functions of galaxies, relying on the Landy–Szalay estimator

(Landy & Szalay 1993), in the redshift range $0.8 < z < 1.3$ for the 5 % H α flux-brightest and the 5 % least bright galaxies in the Flagship m3 and GAEA ECLH mocks. Similar results are found in Flagship m1 and GAEA ECLQ. In both simulations, the clustering is generally higher for the 5 % brightest galaxies compared to their 5 % lowest H α flux counterparts at large separations

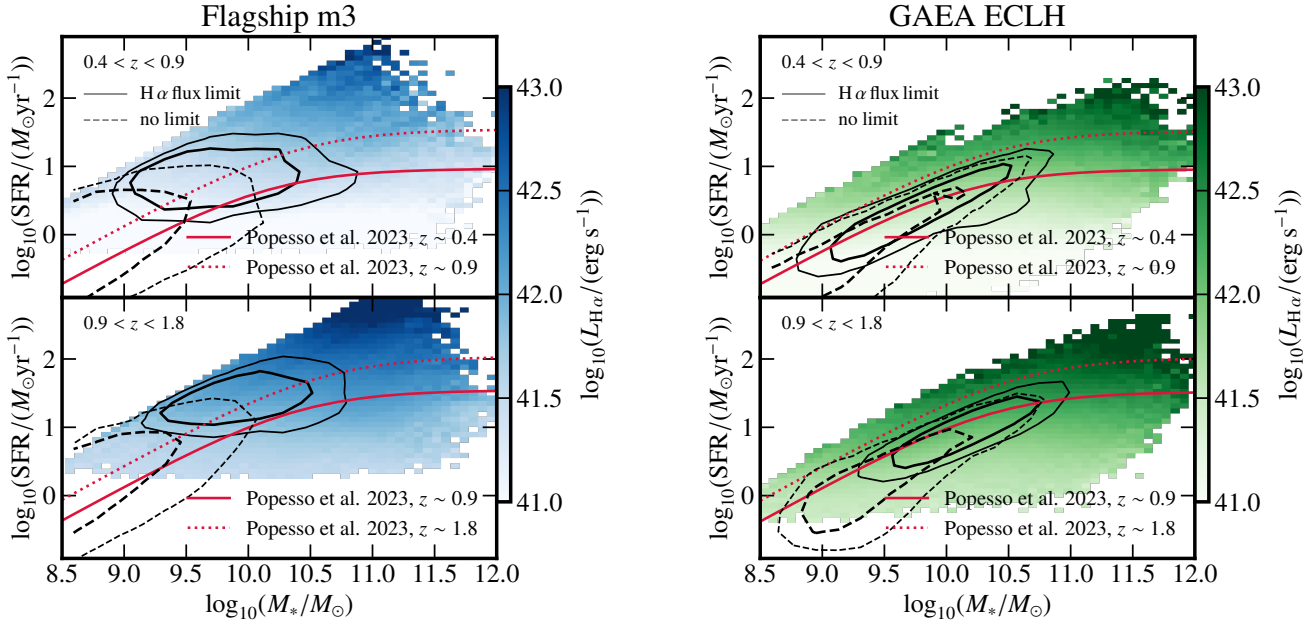


Fig. 3. The star-forming main sequence in the Flagship (left) and GAEA (right) simulations (models m3 and ECLH, respectively) at $0.4 < z < 0.9$ (top) and $0.9 < z < 1.8$ (bottom), color-coded by the $H\alpha$ luminosity, which essentially correlates with SFR. The red lines correspond to the compilation of observational data presented in Popesso et al. (2023). The contours encompass 50% and 75% of the galaxy distribution for $H\alpha$ flux-limited sample (solid lines) and for the sample without any limit (dashed lines).

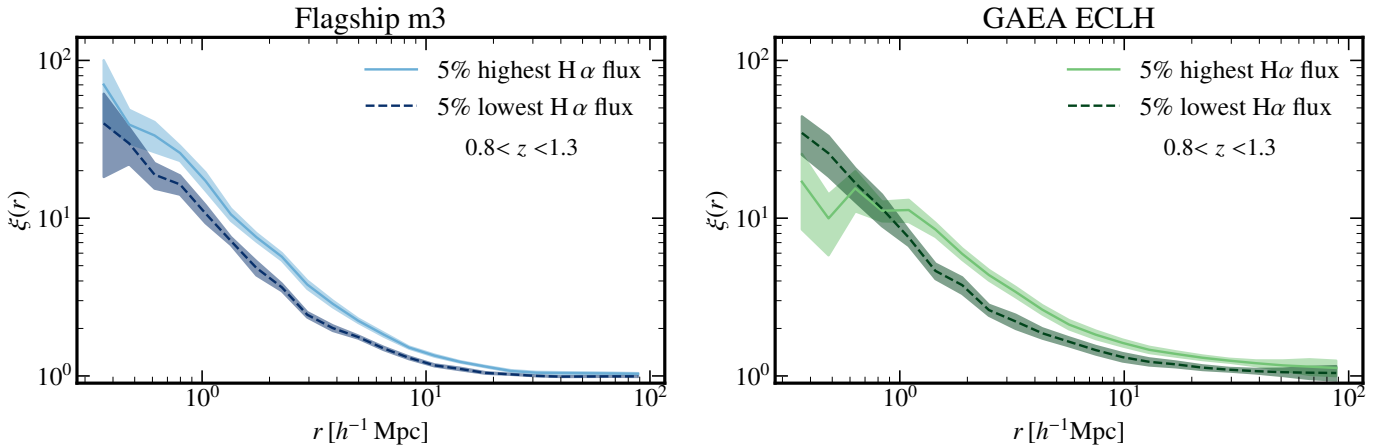


Fig. 4. Two-point correlation functions of galaxies in the redshift range $0.8 < z < 1.3$ for galaxies with the 5 % highest and lowest $H\alpha$ flux in the Flagship m3 (left) and GAEA ECLH (right) mocks. Shaded regions correspond to jackknife error bars. At small separations ($\lesssim 1 h^{-1} \text{Mpc}$), brightest galaxies show enhanced clustering in Flagship compared to their low $H\alpha$ flux counterparts, while brightest galaxies in GAEA show comparable (or reduced) clustering to their lower brightness counterparts. At larger separations ($\gtrsim 1 h^{-1} \text{Mpc}$), brightest galaxies are more clustered compared to their low $H\alpha$ flux counterparts in all mocks.

($\gtrsim 1 h^{-1} \text{Mpc}$). At separations $\lesssim 1 h^{-1} \text{Mpc}$, the 5 % brightest galaxies in GAEA show reduced clustering with respect to their lower-brightness counterparts, whereas in Flagship, the clustering of the brightest galaxies continues to be higher, presumably better tracing the substructures. We note that galaxy clustering was among the constraints used during the construction of Flagship mocks to set the number of satellites and assign colour types to galaxies, while this information was not considered at all for the GAEA models. We note also that the considered redshift range bin is quite large. However, the median (and also mean) redshifts of the 5 % highest and lowest $H\alpha$ flux galaxies are comparable ($\bar{z} \sim 1.0$ for Flagship m3 and GAEA ECLH; $\bar{z} \sim 1.0$ for the 5 % highest and $\bar{z} \sim 1.1$ for the 5 % lowest $H\alpha$ flux sample in Flagship m1 and GAEA ECLQ). Therefore, the observed differences in the clustering of these populations are unlikely to be driven by their redshifts alone. We finally note that qualitatively similar results are found when considering 10 % cut in the $H\alpha$ flux, and/or for higher redshift range, e.g. $1.3 < z < 1.8$.

ferences in the clustering of these populations are unlikely to be driven by their redshifts alone. We finally note that qualitatively similar results are found when considering 10 % cut in the $H\alpha$ flux, and/or for higher redshift range, e.g. $1.3 < z < 1.8$.

2.4. Cosmic web reconstruction

To extract the cosmic web network, we rely on the publicly available and widely used structure finder DisPerSE (Sousbie 2011; Sousbie et al. 2011). To account for the redshift-space distortions that affect any three-dimensional galaxy distribution relying on redshift-based distance measurements, we follow the method outlined in Kraljic et al. (2018). This approach has been previously adopted for the cosmic web reconstruction in three-

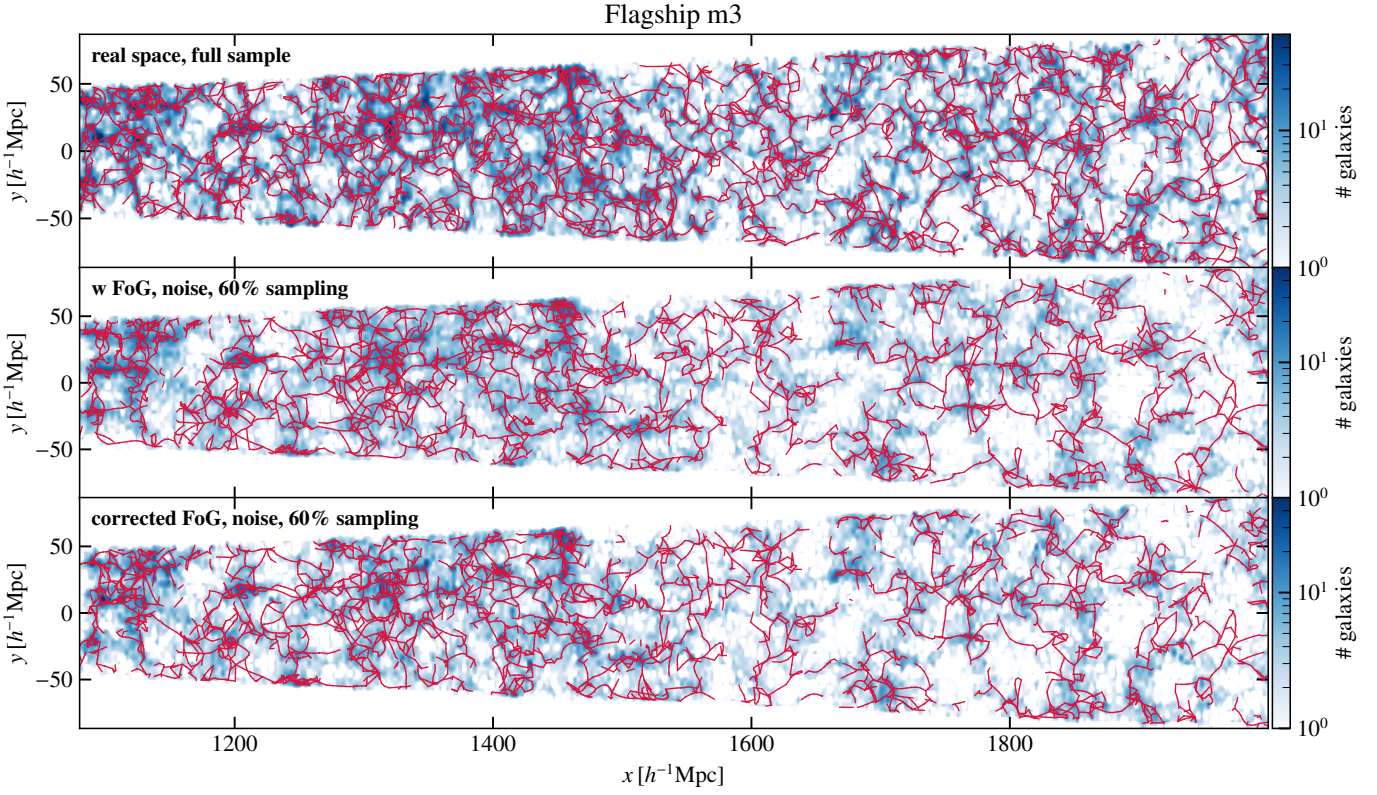


Fig. 5. Visualisation of a $\sim 40 h^{-1}$ Mpc thick slice of the galaxy distribution from the Flagship m3 mock and the corresponding cosmic web skeleton reconstructed without weighting Delaunay tessellation for the reference catalogue without the FoG effect, without added noise and with 100 % completeness (top; \mathcal{D}), with the FoG, added redshift error and 60 % sampling (middle; $\mathcal{D}_{\text{noise},60\%}^{\text{wFoG}}$) and after correcting for the FoG effect (bottom; $\mathcal{D}_{\text{noise},60\%}^{\text{FoG,corr}}$). For the sake of clarity, only $0.4 < z < 0.85$ range of the lightcone is shown.

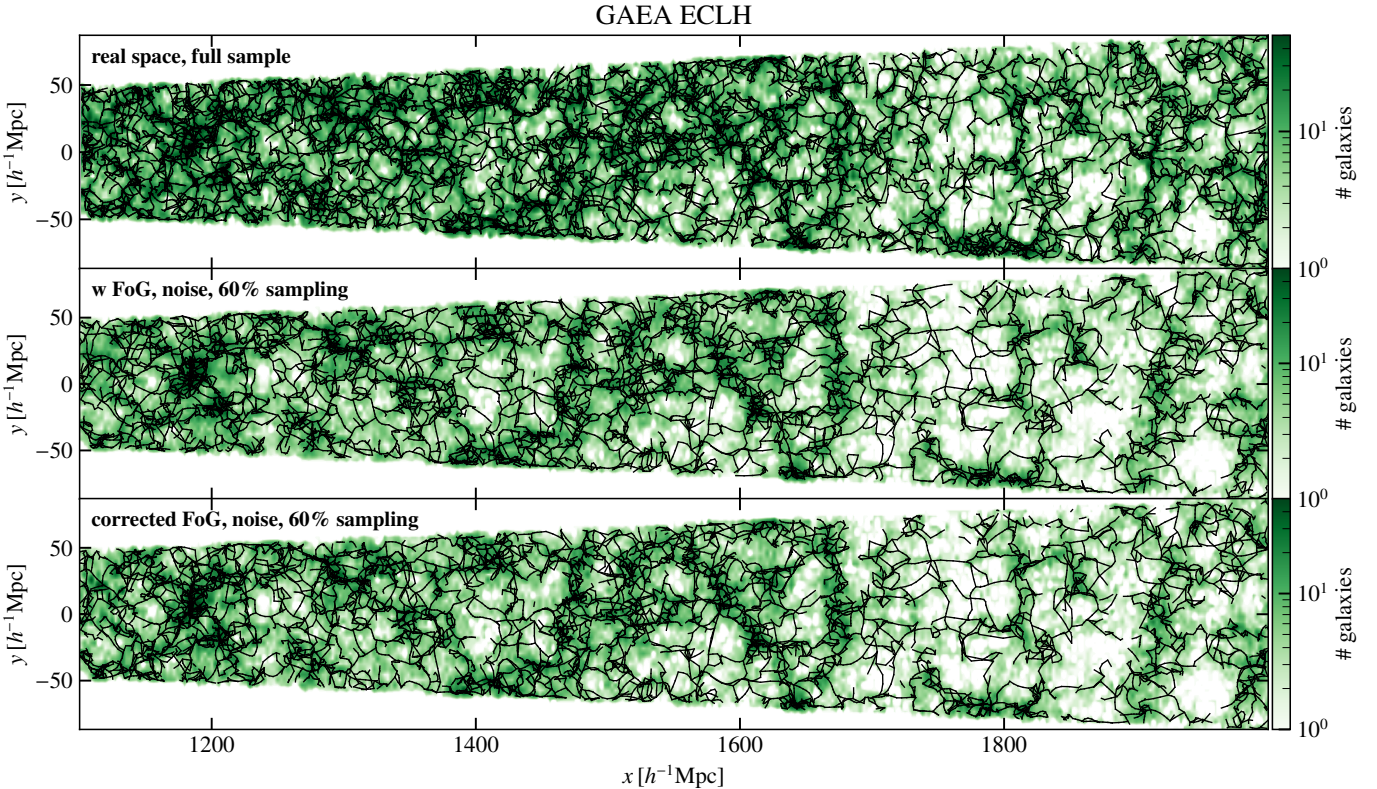


Fig. 6. As in Fig. 5, but for the GAEA ECLH mock. The higher galaxy number density of the GAEA ECLH mock compared to Flagship m3 (Fig. 5) can be clearly seen.

Table 1. Optimal linking lengths (in units of the mean intergalactic separation).

	Flagship		GAEA	
	m3	m1	ECLH	ECLQ
\mathcal{D}	(0.07,14)	(0.07,15)	(0.09,19)	(0.09,20)
\mathcal{D}_{M_*}	(0.07,12)	(0.07,14)	(0.09,16)	(0.09,17)
^a $\mathcal{D}_{\text{noise,60\%}}$	(0.07,25)	(0.07,28)	(0.09,29)	(0.09,29)

Notes. Values in parenthesis (b_{\perp} , R) indicate the linking length perpendicular to the line-of-sight b_{\perp} and the radial expansion factor $R = b_{\parallel}/b_{\perp}$, relating the projected (b_{\perp}) and line-of-sight (b_{\parallel}) linking lengths.

^(a) Same values for linking lengths are applied for M_* and $H\alpha$ -limited samples.

dimensional space using spectroscopic surveys, such as GAMA or SDSS (Kraljic et al. 2018, 2020b). Here we only briefly describe its main steps.

To minimise the impact of redshift-space distortions induced by the random motions of galaxies within virialized haloes, the so-called Fingers-of-God (FoG) effect (e.g., Jackson 1972), we first identify the galaxy groups. This is done using an anisotropic Friends-of-Friends (FoF) algorithm that operates on the projected perpendicular and parallel separations of galaxies (see Treyer et al. 2018, for details on the group finder algorithm) calibrated on the Flagship and GAEA mock catalogues. Table 1 shows the resulting optimal linking lengths, in units of the mean intergalactic separation, for all models used in this work.

The next step consists of the radial compression of the groups such that the dispersions of their member galaxies in transverse and radial directions are equal (see also e.g., Tegmark et al. 2004). The resulting isotropic galaxy distribution within the groups about their centres minimises the impact of elongated structures along the line-of-sight (the FoG effect) that could be misidentified as filaments of the cosmic web.

Finally, DisPerSE is used to coherently identify all the components of the cosmic web, i.e., voids, walls, filaments, and nodes, directly from the inhomogeneous distribution of galaxies, relying on discrete Morse theory (Forman 2001). To deal with such a discrete data set, DisPerSE builds on the Delaunay tessellation allowing one to provide a scale-free Delaunay Tessellation Field Estimator (DTFE; Schaap & van de Weygaert 2000) density and reconstruct the local topology. In this work we will consider the cosmic web reconstruction relying on both the non-weighted and stellar mass-weighted Delaunay tessellation. To deal with noisy data, such as galaxy catalogues, DisPerSE implements the concept of the topological persistence allowing to effectively filter out the topologically less robust features, i.e. features that would disappear or change after resampling of or adding a noise to the underlying field of the galaxy distribution. The level of filtering is controlled by the persistence threshold N_{σ} , such that higher values of N_{σ} select structures that are topologically more robust with respect to noise. The fiducial value used throughout this work is $N_{\sigma} = 5$. This higher value, compared to the more commonly used $N_{\sigma} = 3$, allows us to better highlight challenges of reconstructing cosmic web structures when working with $H\alpha$ flux-limited, rather than stellar mass-limited, noisy data (see Sect. 3). Lastly, the cosmic web skeleton was smoothed in post-processing three times.

For illustration, Figs. 5 and 6 show a $\sim 40 h^{-1}$ Mpc thick slice of the distribution of galaxies within the redshift range $0.4 < z < 0.85$ from the Flagship and GAEA mock catalogues

(models m3 and ECLH, respectively) together with the corresponding network of filaments, reconstructed using unweighted Delaunay tessellation, for the reference catalogue, i.e. without FoG effect and with 100% completeness (top), after adding redshift error, 60 % sampling and FoG effect (middle), and after correcting for the FoG effect (bottom). This visual inspection allows us to already identify some of the key factors impacting the quality of the cosmic web reconstruction, namely, the FoG effect, redshift uncertainty, and the incompleteness of the underlying galaxy sample.

In the following, catalogues including redshift-space distortions are denoted with ‘wFoG’ in the superscript, for example $\mathcal{D}^{\text{wFoG}}$, while catalogues with applied correction for the FoG effect have ‘FoG,corr’ in the superscript, such as $\mathcal{D}^{\text{FoG,corr}}$.

3. Results

To assess the quality of the cosmic web reconstruction expected for the EDFs, we consider three different measures. These involve geometrical and topological properties of the cosmic web and transverse stellar-mass gradients of galaxies with respect to filaments of the cosmic web, i.e. the observed and theoretically expected trend of increasing galaxies’ stellar mass with their decreasing distance from filaments.

3.1. The geometrical cosmic web measures

Geometrical measures of individual cosmic web components, such as the length of filaments, the area of walls, and the volume of voids, provide a straightforward way to assess the impact of different parameters on the quality of the cosmic web reconstruction. We explore in particular the impact of the FoG effect, redshift errors, and incompleteness of the galaxy sample.

Figure 7 shows the probability distribution function (PDF) of the lengths of filaments⁴, areas of walls, and volumes of voids for Flagship mock, m3 model (m1 model leads to the same conclusions) for the cosmic web reconstruction with (left) and without (right) the stellar mass-weighted Delaunay tessellation. Similarly, Fig. 8 presents the PDF of the filaments’ lengths for GAEA mock, model ECLH (the same conclusions apply to the ECLQ model). For walls and voids (not shown), qualitatively similar results and conclusions to those of Flagship are obtained.

As expected, the FoG effect has a strong impact on the filaments of the cosmic web, and much less so on its other components. When this effect is not corrected for, the reconstructed filaments tend to be too long as manifested by the shift of the distribution of filaments’ lengths toward larger values ($\mathcal{D}_{\text{noise,60\%}}^{\text{wFoG}}$) compared to the reference sample without redshift-space distortions ($\mathcal{D}_{60\%}$). After correcting for the FoG effect ($\mathcal{D}_{\text{noise,60\%}}^{\text{FoG,corr}}$), the distributions of filaments’ lengths are in excellent agreement, both in terms of medians and overall shape for Flagship. For GAEA, the correction is not perfect, showing some residual deficit of long and excess of intermediate length filaments. We note, however, that the medians of the distributions are comparable.

Weighting the Delaunay tessellation by the stellar mass of galaxies turns out to be important for recovering a better agreement between the distributions before and after correcting for the FoG effect when the galaxy sample is not stellar mass-limited, as is the case for the EDS. As can be seen, the agreement between

⁴ In practice, half length of filaments, measured as the curvilinear distance between filament-type saddle points and maxima, the nodes of the cosmic web.

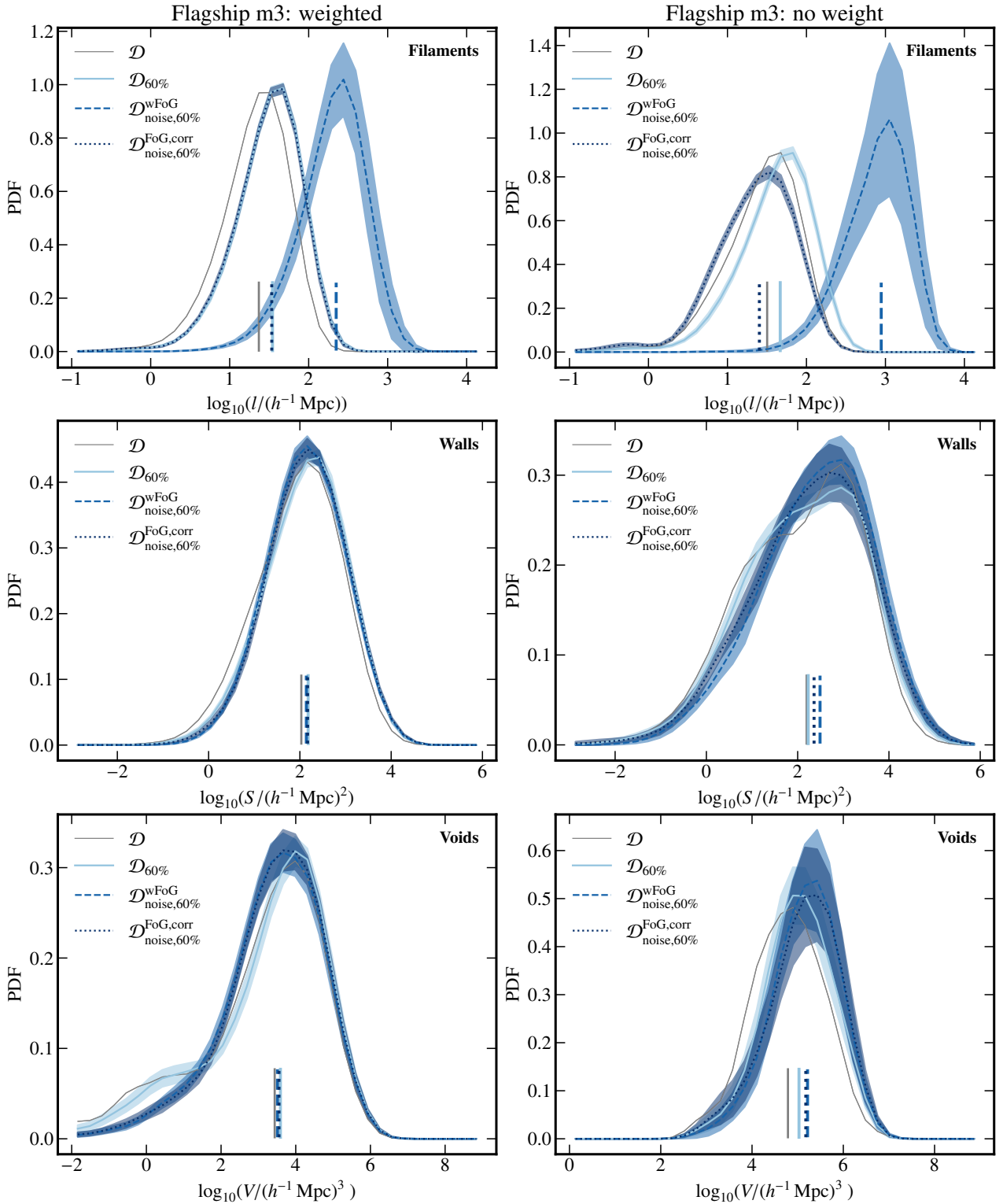


Fig. 7. PDF of filament lengths (top), wall areas (middle) and void volumes (bottom) for EDS mocks without redshift-space distortions for full (\mathcal{D} ; solid grey lines), and 60% ($\mathcal{D}_{60\%}$; solid coloured lines) sampling, including the FoG effect ($\mathcal{D}^{w\text{FoG}}$; dashed coloured lines) and after the compression of FoG ($\mathcal{D}^{\text{FoG,corr}}_{\text{noise,60\%}}$; coloured dotted lines) for the Flagship (model m3) simulation. PDFs obtained using the stellar mass-weighted Delaunay tessellation for the cosmic web reconstruction (left) are compared with the reconstruction without weighting (right). Vertical lines indicate the medians of the distributions. Shaded regions correspond to the standard deviation across five mocks. The FoG mainly impacts the length of filaments which tend to be longer. After the compression of groups, the PDFs are in a good agreement with the reference distribution. Weighting the tessellation helps bringing in better agreement the distributions of the reference catalogue without the FoG effect ($\mathcal{D}_{60\%}$) and after the correction for the FoG effect ($\mathcal{D}^{\text{FoG,corr}}_{\text{noise,60\%}}$). For the PDFs of void volumes obtained for the reconstruction without weighted tessellation, to avoid spurious border effects, only voids with volume larger than the volume corresponding to the mean intergalactic separation are considered.

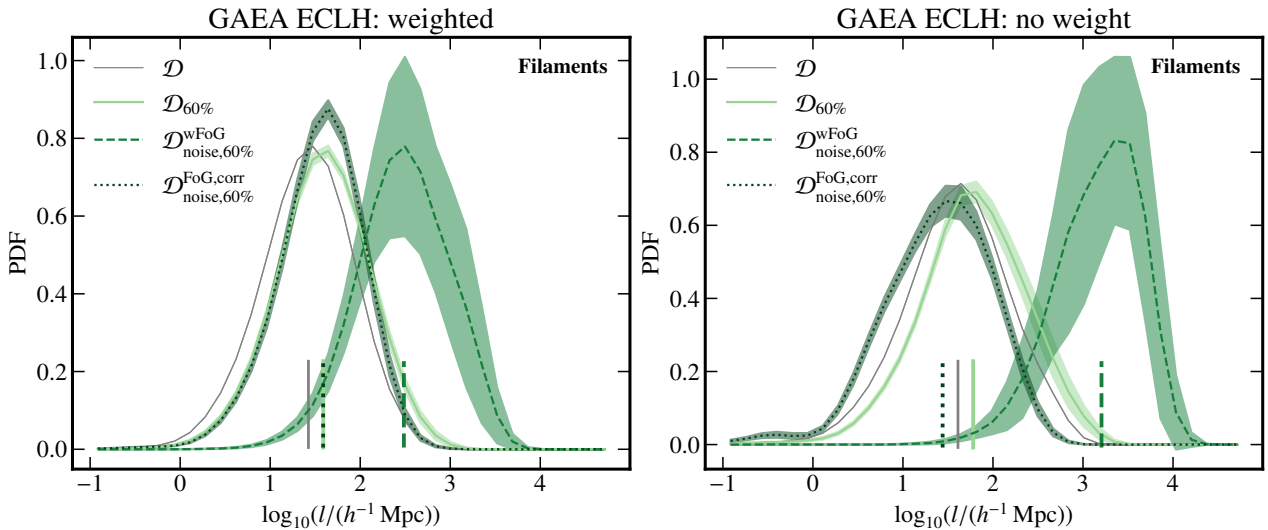


Fig. 8. As in Fig. 7 but for GAEA mocks (model ECLH) and filament lengths alone.

the distributions of filaments' lengths does improve once the correction of the FoG effect is applied, but it is not as good as in the case of weighting. This is a direct consequence of the galaxy sample being $H\alpha$ flux- rather than stellar mass-limited (see Fig. A.1). For stellar mass-limited galaxy samples the method used to deal with the FoG is efficient even without weighting the tessellation. The sample selection based on the $H\alpha$ flux is also responsible for our failure to correct completely for the FoG effect seen for GAEA. The underlying reason is the inability to properly reconstruct galaxy groups, virialized structures responsible for small-scale redshift-space distortions, when the sample is not stellar mass-limited. As discussed in Sect. 2.3.4, Flagship and GAEA mocks show different clustering on small scales, with brightest galaxies tracing presumably more closely substructures in Flagship models, therefore resembling more the stellar mass selection.

The incompleteness of the galaxy sample manifests, as expected, by a shift of the distributions toward higher values (compare $\mathcal{D}_{60\%}$ vs. \mathcal{D} in Figs. 7 and 8), in particular for the filaments' lengths. Walls and voids are impacted to a much lesser degree, especially when weighting is applied.

Redshift error, on top of the sample selection (whether it is stellar mass or $H\alpha$ flux selected), impacts strongly our ability to correct for the FoG effect (see Fig. A.3). However, the correction works better for the stellar mass-limited sample.

In summary, the small-scale redshift-space distortions strongly impact the cosmic web reconstruction, filamentary network in particular, regardless of the sample selection and regardless of the weighting of the tessellation. The applied correction for the FoG effect works better for stellar mass-limited samples. On top of the sample selection, the redshift uncertainties hinder our ability to correct for the FoG effect.

3.2. Connectivity and multiplicity

The connectivity and multiplicity of the cosmic web, i.e. the number of filaments respectively globally and locally connected to the nodes of the cosmic web, where massive galaxy groups and clusters predominantly reside, are interesting topological measures. They are expected to depend on the underlying cosmology and to impact the assembly of galaxies and hence their properties. It is therefore important to assess our ability to re-

cover these quantities from the expected configuration for the EDFs.

Let us start by considering the distribution of connectivity, defined as the number of filaments connected to a given node of the cosmic web. Figure 9 shows the histograms of connectivity of central galaxies⁵ in the $H\alpha$ flux-limited sample measured in the Flagship and GAEA mocks (models m3 and ECLH, respectively, but qualitatively similar results are obtained for models m1 and ECLQ). The FoG effect has a strong impact on the connectivity of galaxies at the nodes of the cosmic web ($\mathcal{D}^{w\text{FoG}}$), modifying both the shape of the distribution, but also its median (indicated by a vertical line), regardless of the sample selection, i.e., including M_* -limited samples ($\mathcal{D}_{M_*}^{w\text{FoG}}$; see Fig. B.1). Correction of the FoG effect works very well for the M_* -limited sample and reasonably well for the $H\alpha$ flux-limited sample in terms of the overall shape of distributions, but also their mean and median values (see Tables B.1 and B.2). The weighting of the tessellation by stellar mass for the $H\alpha$ flux-based selection (left panels of Fig. 9) tends to artificially increase connectivity even in the absence of redshift-space distortions, for example, with a median value of 8 (11) as opposed to a median value of 3 (5) without weighting for Flagship m3 (GAEA ECLH). For the M_* -limited selection, the impact of weighting of the tessellation by stellar mass on the connectivity is very weak (see Fig. B.1). Adding redshift errors and incompleteness decreases the quality of the cosmic web reconstruction, in particular for the $H\alpha$ -based selection (Fig. 10) due to the reduced ability to correct for FoG. In this configuration, stellar mass weighting of the tessellation improves the cosmic web reconstruction (see Tables B.1 and B.2).

Let us now explore the multiplicity and our ability to recover this local property of the cosmic web, defined as the connectivity minus the number of bifurcation points (i.e. points where filaments split, even though they are not extrema, Pogosyan et al. 2009), associated with each node. Figure 11 shows the multiplicity of central galaxies in Flagship and GAEA mocks (models m3 and ECLH, respectively, but almost identical results are obtained for the Flagship model m1 and the GAEA model ECLQ) for

⁵ We focus on central galaxies to limit the complications due to the non-linear nature of the satellite population and to ease the comparison with theoretical predictions (for a more detailed discussion on the effect of satellites on connectivity, see Kraljic et al. 2020b).

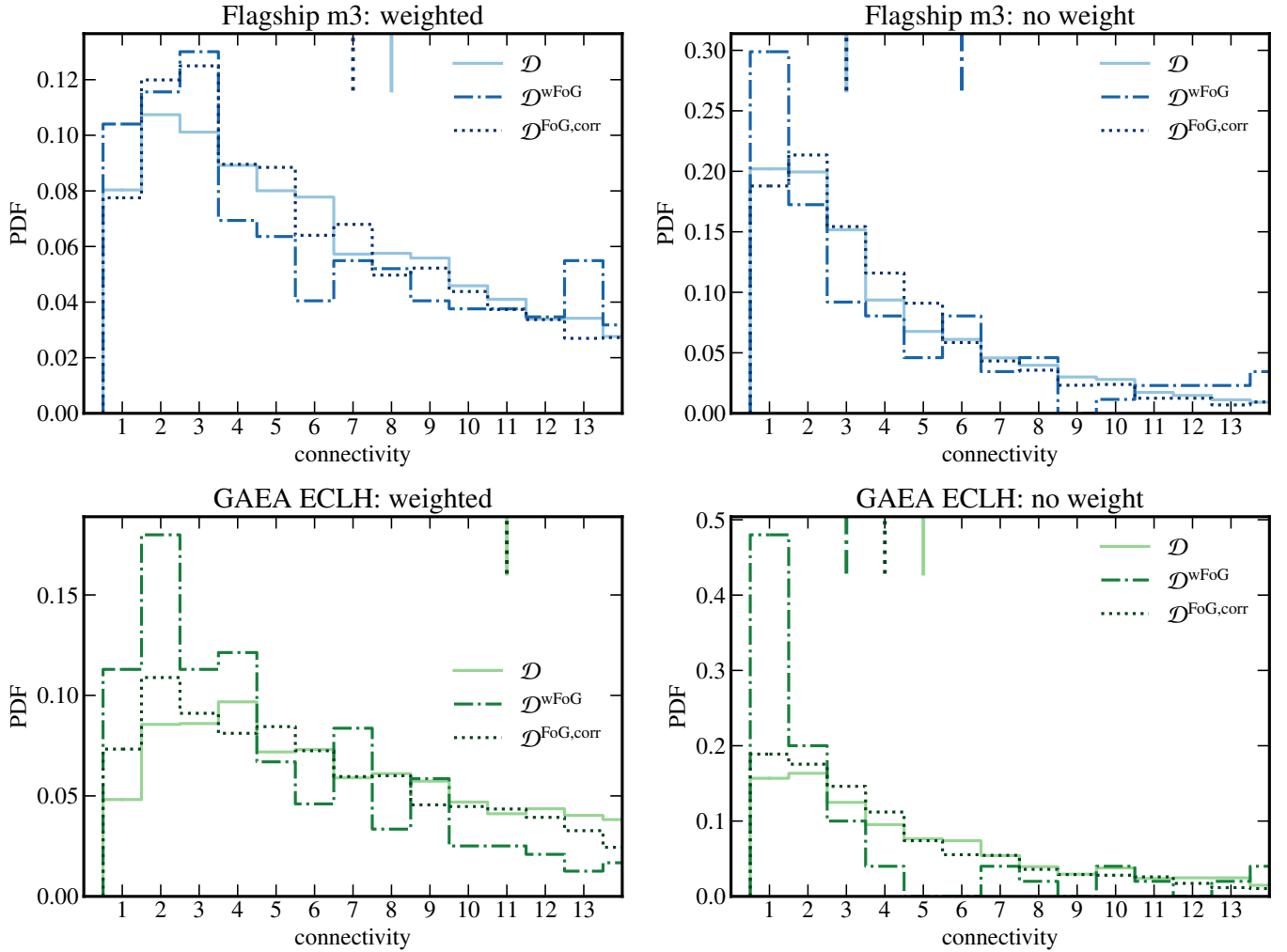


Fig. 9. PDFs of the connectivity of central galaxies for the $H\alpha$ -limited selection of galaxies in the full sample without redshift error (\mathcal{D}) for Flagship (model m3, top panels) and GAEA (model ECLH, bottom panels), with stellar mass weighting of the skeleton (left) and without weighting (right). In each panel, vertical lines indicate the medians of distributions. For a better visibility, the histograms are limited to the connectivity values below 14. Mean and median values for all distributions are reported in Tables B.1 and B.2. The redshift-space distortions have a strong impact on the connectivity of galaxies, but this effect can be reasonably well corrected for.

the fiducial sample ($\mathcal{D}_{\text{noise},60\%}$). Similarly to the connectivity, not correcting for the FoG effect modifies the distribution of multiplicity, but to a much lesser extent, in particular when the Delaunay tessellation is weighted by stellar mass. The mean and median values of the multiplicity agree very well across all mocks for weighted tessellation. For cosmic web reconstruction without weighting the tessellation, the correction of the FoG effect is needed to obtain good agreement between the distributions of multiplicity (Tables B.3-B.4). Qualitatively similar conclusions apply to the M_* -limited samples. The multiplicity of the cosmic web therefore appears to be a more robust topological property compared to connectivity given its weak sensitivity to the FoG effect, redshift error, sample completeness, and its selection.

Beyond the statistical measurements of connectivity and multiplicity, it is of interest to explore these quantities as a function of different galaxy properties. In this work, we focus on stellar mass. Figure 12 shows the connectivity of central galaxies as a function of their stellar mass for the Flagship and GAEA mocks (models m3 and ECLH, respectively, with qualitatively similar conclusions for m1 and ECLQ) for the fiducial sample ($\mathcal{D}_{\text{noise},60\%}$). Regardless of the sample selection, i.e. $H\alpha$ - or M_* -limited (see Fig. B.2), central galaxies in the reference sample

follow the expected trend, where the connectivity increases with increasing stellar mass, for the probed stellar mass range and when no weighting is applied prior to the cosmic web reconstruction (right panels of Fig. 12). Weighting of the Delaunay tessellation introduces a bias at lower stellar masses, in particular for the $H\alpha$ -based galaxy selection, leading to an increase of the connectivity with decreasing stellar mass (left panels of Fig. 12). As already seen from the global distributions, the redshift-space distortions have a strong impact on the connectivity of the cosmic web. This leaves a clear signature in the form of a shift of the M_* -connectivity relation toward higher values of connectivity, for mocks with FoG compared to the reference sample, regardless of the tessellation weighting. The applied correction of the FoG effect allows us to recover reasonably well the M_* -connectivity relation of the reference samples, in particular for weighted tessellations. Weighting the tessellation by stellar mass is crucial for recovering the M_* -connectivity trend if the sample is $H\alpha$ flux-limited, in the presence of the redshift errors, and for reduced sampling, albeit with an introduced bias at lower masses.

Figure 13 shows the multiplicity of central galaxies as a function of their stellar mass for the Flagship and GAEA mocks

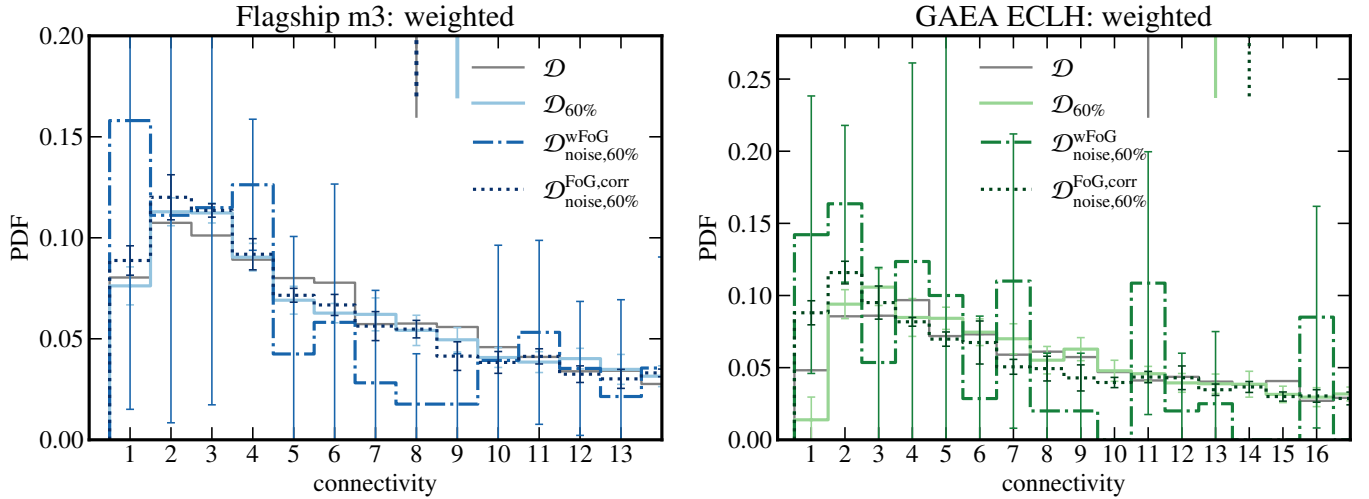


Fig. 10. PDFs of the connectivity of central galaxies for the $H\alpha$ -limited selection of galaxies in the fiducial sample ($\mathcal{D}_{\text{noise},60\%}$; coloured lines) for Flagship (model m3, left panel) and GAEA (model ECLH, right panel), with stellar mass weighting of the skeleton. The full sample without noise (\mathcal{D}) is shown for comparison (grey lines). In each panel, vertical lines indicate the medians of distributions and error bars correspond to the standard deviation across five mocks. For a better visibility, the histograms are limited to the connectivity values below 14. Mean and median values for all distributions are reported in Tables B.1 and B.2. Redshift errors and incompleteness of the sample decrease the quality of the cosmic web reconstruction, which can be improved by stellar mass weighting.

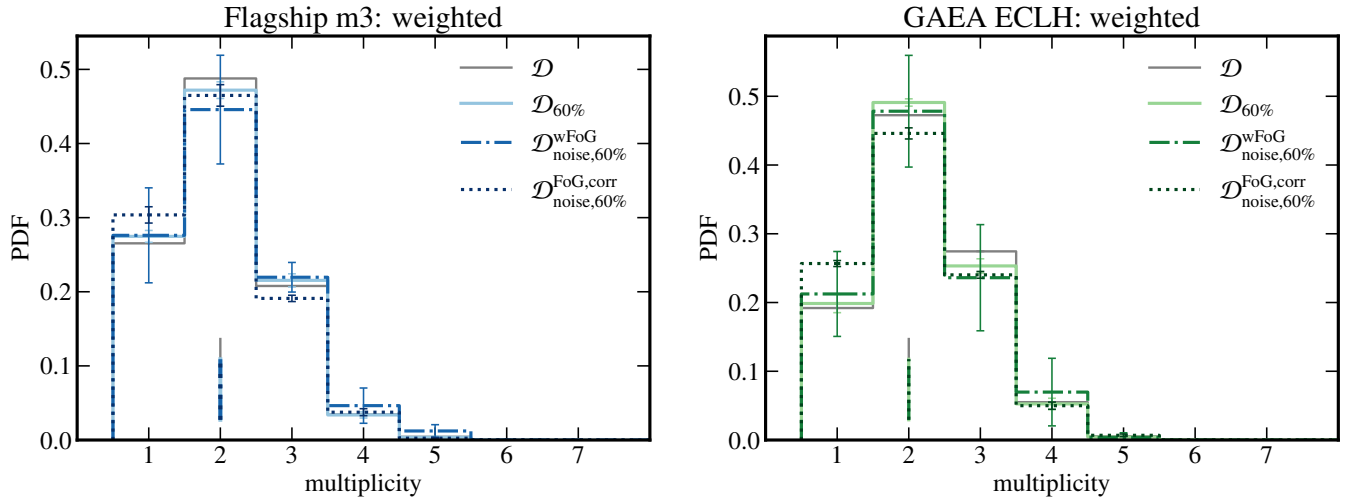


Fig. 11. PDFs of the multiplicity of central galaxies for an $H\alpha$ -limited selection of galaxies in the fiducial sample ($\mathcal{D}_{\text{noise},60\%}$; coloured lines) for Flagship (model m3, left panel) and GAEA (model ECLH, right panel), with stellar mass weighting of the skeleton. The full sample without noise (\mathcal{D}) is shown for a comparison (grey lines). In each panel, vertical lines indicate the medians of distributions and error bars correspond to the standard deviation across five mocks. The mean and median values for all distributions are reported in Tables B.3 and B.4. The multiplicity of the cosmic web shows only a weak sensitivity to the FoG effect, redshift error, and sample completeness.

(models m3 and ECLH, respectively, with qualitatively similar conclusions for m1 and ECLQ) for the fiducial sample ($\mathcal{D}_{\text{noise},60\%}$). As in the case of connectivity, the multiplicity of central galaxies increases with increasing stellar mass for galaxies in all reference catalogues (\mathcal{D}) regardless of sample selection (see Fig. B.3 for the M_* -limited sample; \mathcal{D}_{M_*}) and without tessellation weighting (see Fig. B.4). At the lowest stellar mass end (below $10^{9.5} M_\odot$), accessible only in the $H\alpha$ flux-selected samples, multiplicity tends to increase when stellar mass-weighted tessellation is used for the cosmic web reconstruction. Contrary to connectivity, the redshift-space distortions do not strongly modify the amplitude of the M_* -multiplicity relation. The impact of FoG on this relation is overall very limited for the reconstruction with the stellar mass-weighted tessellation, but critically reduces our ability to recover the trend when the sample is

$H\alpha$ flux-limited ($\mathcal{D}^{\text{wFoG}}$, $\mathcal{D}_{\text{noise},60\%}^{\text{wFoG}}$) and no weighting is applied. The applied FoG correction significantly improves our ability to recover the M_* -multiplicity relation in all mocks, but as for connectivity, the quality of this correction decreases with added redshift errors.

In summary, for $H\alpha$ flux-limited samples, as in the case of EDF, the multiplicity appears to be a more robust quantity, compared to connectivity. Indeed, even without weighting the tessellation, and after applying a correction for the FoG effect, we are able to recover the M_* -multiplicity relation in the presence of redshift error and reduced sampling. However, given that the range of multiplicity values is quite restrained, we anticipate that it might still be difficult to retrieve correlations between the multiplicity of galaxies located at nodes of the cosmic web and

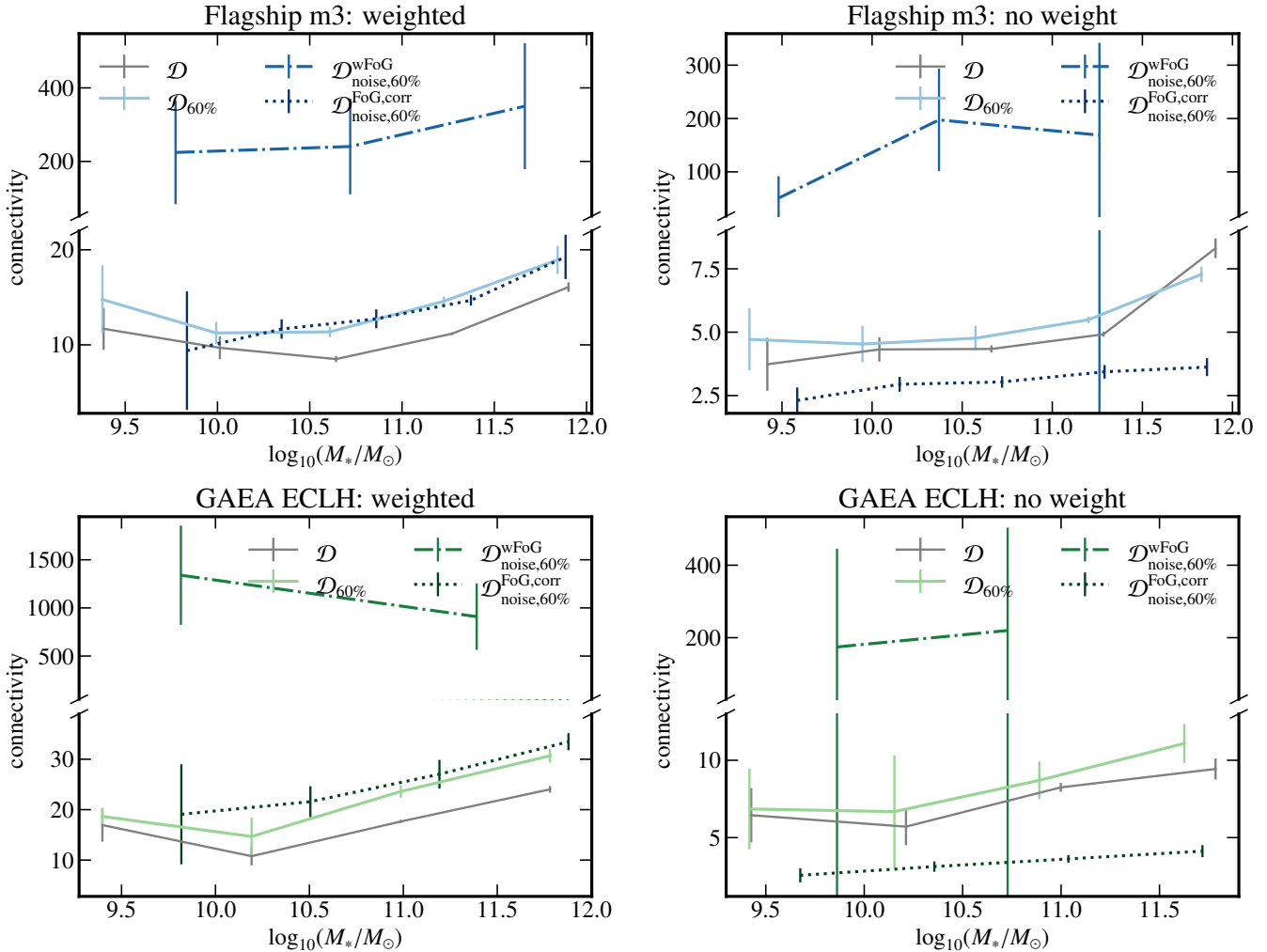


Fig. 12. Connectivity of central galaxies as a function of their stellar mass in Flagship (model m3, top panels) and GAEA (model ECLH, bottom panels) mocks for the fiducial galaxy sample $\mathcal{D}_{\text{noise},60\%}$, with stellar mass weighting of the skeleton (left) and without weighting (right). As expected, connectivity increases with stellar mass, with weighting of the Delaunay tessellation introducing a bias at lower stellar masses leading to reversed trend. Correction for the FoG effect is needed to recover reasonably well the M_* -connectivity relation, in particular for weighted tessellations.

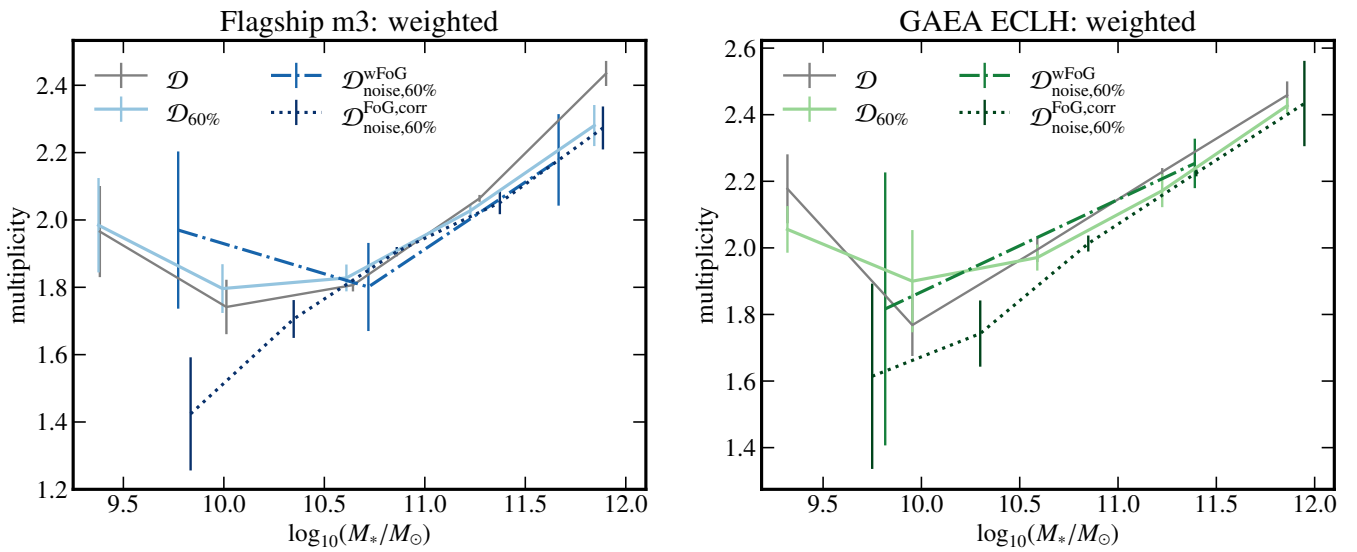


Fig. 13. Multiplicity of central galaxies as a function of their stellar mass in Flagship (model m3, left panel) and GAEA mocks (model ECLH, right panel) for the fiducial sample, with stellar mass weighting of the skeleton. As for connectivity, multiplicity increases with M_* , with a reversed trend at low M_* . In contrast to connectivity, the redshift-space distortions do not strongly modify the amplitude of the M_* -multiplicity relation.

their properties beyond stellar mass (e.g., morphology or star-formation activity).

3.3. Stellar-mass gradients

As explained by the theory of biased clustering (e.g., [Kaiser 1984](#); [Efstathiou et al. 1988](#)), the mass of galaxies is expected to depend on their large-scale environment, such that more massive galaxies are preferentially formed in over-dense regions (e.g., [Bond & Myers 1996](#); [Pogosyan et al. 1996](#); [Malavasi et al. 2017](#); [Kraljic et al. 2018](#); [Laigle et al. 2018](#)).

Let us now explore the stellar-mass gradients with respect to filaments of the cosmic web and our ability to recover this trend with the EDS.

[Figure 14](#) shows the PDFs of the distances of galaxies to their closest filament for the Flagship m3 model and for the reconstruction of the cosmic web with weighted tessellation as a function of stellar mass and redshift. The equivalent PDFs for the reconstruction without weighting are presented in [Fig. C.2](#). Similar results are obtained for the Flagship m1 model and both GAEA models. The distances are normalised by the mean intergalactic separation to take into account the effect of decreasing the density of galaxies with increasing redshift. After accounting for these redshift variations, stellar-mass gradients, where more massive galaxies are preferentially located closer to filaments compared to their lower-mass counterparts, exhibit only minimal evolution in the redshift range $0.4 < z < 1.8$, with galaxies typically found closer to the filaments of the cosmic web at lower redshifts.

Stellar-mass gradients towards filaments of the cosmic web are recovered in the reference sample (\mathcal{D} , first rows of [Figs. 14](#) and [C.2](#)) regardless of whether the weighting of Delaunay tessellation is applied or not. We note that the bimodality seen for the distributions without weights is due to our choice for a relatively high value of the persistence threshold N_σ applied to select filaments. This is caused by the removal of topologically less significant filaments for higher N_σ , which leaves some galaxies associated with filaments further away.

Reducing sample completeness weakens this signal ($\mathcal{D}_{60\%}$, [Figs. C.1](#) and [C.2](#)), especially when the cosmic web is reconstructed without stellar mass-weighted tessellation. Redshift errors further reduce our ability to detect the stellar-mass gradients across the entire mass range ($\mathcal{D}_{\text{noise},60\%}^{\text{wFoG}}$, [Fig. C.1](#)), in particular for reconstructions without tessellation weighting. Correcting for the FoG effect does not significantly improve the strength of the signal ($\mathcal{D}_{\text{noise},60\%}^{\text{FoG,corr}}$, second rows of [Figs. 14](#) and [C.2](#)).

4. Discussion

4.1. Guidelines for cosmic web reconstruction with the spectroscopic Euclid Deep dataset

One of the major difficulties identified in this work hampering the reconstruction of the cosmic web in three dimensions is the galaxy selection function. An $H\alpha$ flux-limited, rather than a stellar mass-limited selection of galaxies, is suboptimal for the reconstruction of the cosmic web in three dimensions. On top of that, the redshift errors expected for the EDS further reduce the quality of the cosmic web reconstruction. In this section, we summarise and discuss possible choices to deal with these issues together with their implications.

Any cosmic web reconstruction in three dimensions employing galaxy redshift-based distances needs to account for the redshift-space distortions. Widely used methods to correct for

such an effect on small scales depend on a reliable detection of galaxy groups and clusters. The optimisation of a group finder is typically performed on galaxy mocks designed to capture the specificities of a given survey. We have at our disposal two sets of mock catalogues, the Flagship and GAEA simulations, each providing two models of $H\alpha$ flux of galaxies. As all these models reasonably represent galaxy populations at $0.4 < z < 1.8$, based on comparisons with observational datasets of the galaxies' main sequence, stellar mass, and $H\alpha$ luminosity functions, we used them to optimise the anisotropic group finder.

However, due to inherent differences in the modelling of $H\alpha$ flux, Flagship and GAEA show some fundamental differences, for example in the clustering of galaxies on small scales (below $\sim 1 h^{-1} \text{Mpc}$; see [Fig. 4](#)), or number density of galaxies across the entire redshift range (see [Fig. 1](#)). All of these non-trivial differences make it difficult to homogenise the cosmic web reconstruction. Consequently, we decided to treat each model as a plausible representation of our Universe and optimised the reconstruction process individually. The resulting optimal linking lengths are reported in [Table 1](#). We note that these values are different for the Flagship and GAEA mocks, but they are reasonably close, not only to each other but also to the values adopted for the FoF algorithm-based group reconstruction method concentrating on lower redshift spectroscopic surveys (e.g., [Robotham et al. 2011](#); [Duarte & Mamon 2014](#); [Treyer et al. 2018](#)). This means that the exact choice of the linking lengths for the reconstruction of galaxy groups in the EDS will have to be made once the data are available on the basis of the comparison with the two mocks.

When reconstructing the cosmic web from discrete galaxy samples that are $H\alpha$ flux- rather than stellar mass-limited, weighting the Delaunay tessellation by stellar mass of galaxies might improve the quality of the reconstruction, in particular in the presence of redshift errors with an RMS of $0.001(1+z)$. However, this only holds for certain quantities. Among those explored in this work, geometrical cosmic web quantities, i.e. the length of filaments, the area of walls, and the volume of voids, are better recovered when stellar mass weighting is applied.

For topological cosmic web measurements, such as connectivity and multiplicity, the recommendation to apply weighting is less obvious. The main reason is that the stellar mass-weighted tessellation modifies the connectivity of the reconstructed filamentary network by typically shifting it towards higher values. Hence, the comparison with theoretical predictions and existing measurements from hydrodynamical simulations (e.g. [Kraljic et al. 2020b](#); [Galárraga-Espinosa et al. 2024](#)) and low-redshift mass- or volume-limited samples (e.g. [Kraljic et al. 2020b](#)) becomes less obvious; this should be properly taken into account when interpreting any such connectivity measurement. However, stellar mass weighting helps to recover the M_* -connectivity correlation. Interestingly, the multiplicity of the cosmic web seems to be very weakly affected by weighting, allowing us to reconstruct the correlation between the stellar mass of central galaxies and the number of locally connected filaments, as well as the global measure of the multiplicity such as its PDF. We therefore recommend using multiplicity rather than connectivity.

Finally, the segregation of galaxies by stellar mass with respect to their distance to the filaments of the cosmic web, as explored in this work, is found to be strongly impacted by the redshift error expected for the EDS. The stellar-mass gradients are recovered even without weighting by the stellar mass of galaxies. However, this signal is quite weak, and we anticipate that measuring gradients of quantities beyond stellar mass of galaxies, for example, sSFR gradients, would be very challenging. A signifi-

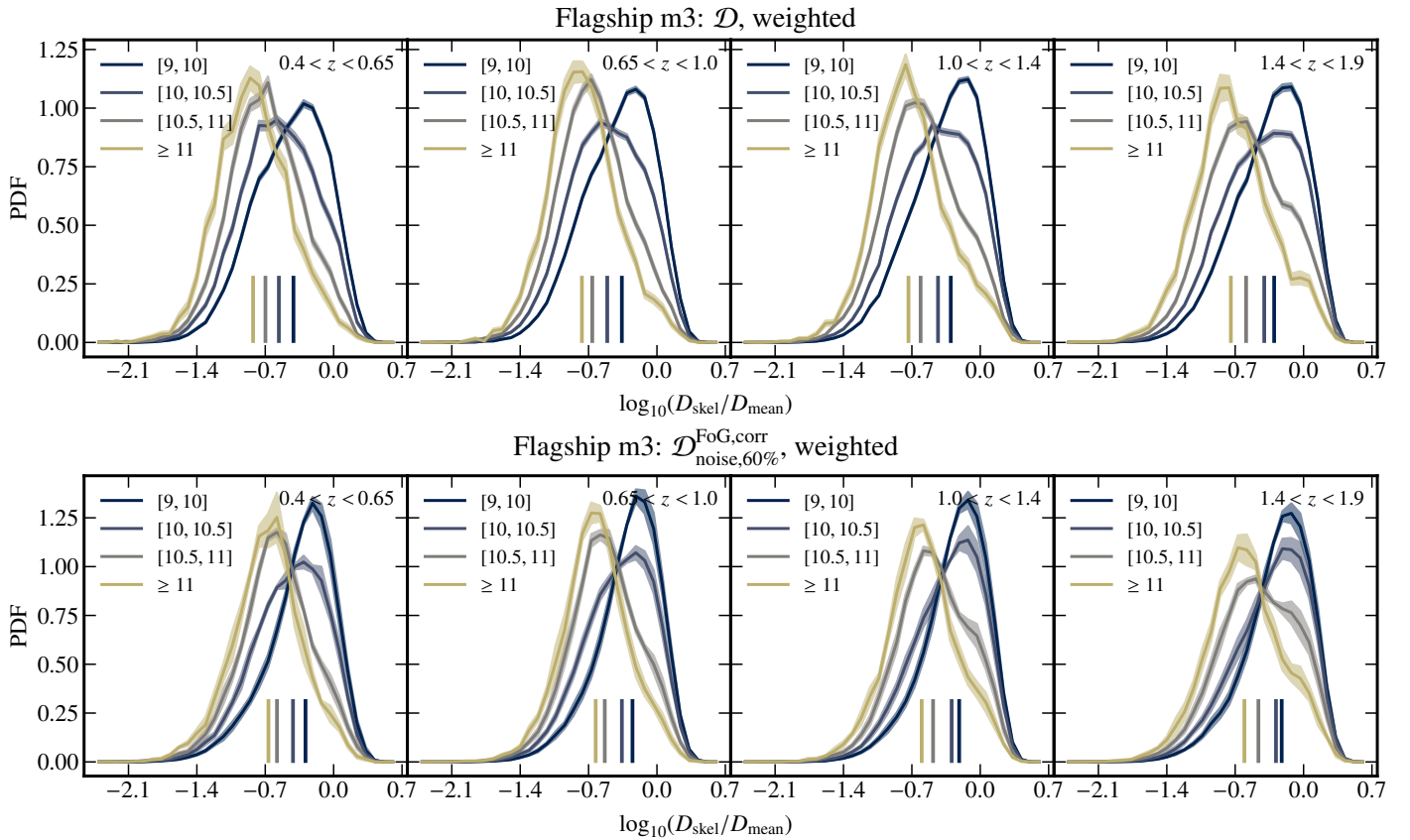


Fig. 14. PDFs of the closest filament's distance, normalised by the redshift dependent mean intergalactic separation, for galaxies in the Flagship mock (model m3) in different stellar mass bins (coloured lines; with numbers indicating $\log_{10}(M_*/M_\odot)$ values) and the cosmic web reconstructed using the stellar mass-weighted Delaunay tessellation. Stellar-mass gradients are shown as a function of redshift from the lowest redshift bin (left) to the highest one (right). Stellar-mass gradients, with more massive galaxies located closer to the filaments than their lower mass counterparts, present in the reference $H\alpha$ flux-limited sample (\mathcal{D} , first row), are recovered when the FoG correction is performed ($\mathcal{D}_{\text{noise},60\%}^{\text{Fog,corr}}$, second row) for the sample with reduced completeness and added redshift error. Vertical lines indicate medians, and the shaded regions are the bootstrap errors for the \mathcal{D} catalogue and the standard deviation across five mocks for the remaining ones.

cant improvement can be obtained by weighting the tessellation by stellar mass. Weighting the tessellation by stellar mass may seem to lead to stellar-mass gradients somewhat by construction. However, the stellar-mass gradients with respect to the filaments are naturally present and recovered in the reference sample without any weighting for the cosmic web reconstruction. In addition, the tests we conducted revealed that weighting by stellar masses randomly assigned to galaxies from the same catalogue significantly reduces the presence of stellar-mass gradients. We therefore conclude that while the stellar mass weighting of the tessellation clearly biases to some extent the cosmic web reconstruction (by construction more massive galaxies will follow the cosmic web more closely), the stellar-mass gradients are inherently present in the distribution of galaxies on large scales.

4.2. Science cases with *Euclid* Deep Survey

The current study focuses on the technical aspects of cosmic web reconstruction within EDS, with the aim of providing basic guidelines for future analysis. Validation has been performed by analysing some of the more fundamental properties of the cosmic web, with correlations involving filaments on the one hand and stellar mass of galaxies on the other. *Euclid* data provide the foundation to extend this analysis to other properties beyond their stellar mass, potentially allowing us to study the

co-evolution of galaxies and the cosmic web at epochs close to cosmic noon.

It will be of particular interest to assess the impact of the cosmic web on the star formation of galaxies. Through measurements of the $H\alpha$ flux of galaxies, *Euclid* will provide access to their star-formation rate (SFR) for the spectroscopic sample within the EDS. It will therefore be possible to perform the analysis of the gradients of the specific star-formation rate (sSFR) of galaxies with respect to the distance to filaments and walls of the cosmic web. At low redshifts, galaxies with lower sSFR (or redder colours) are found to be located closer to filaments and walls, compared to galaxies with higher sSFR (or bluer colours) at fixed M_* . Qualitatively similar trends are found in cosmological hydrodynamical simulations, with such a behaviour persisting up to at least redshift $z \sim 1$, and weakening or vanishing at $z \sim 2$ (e.g. Xu et al. 2020; Hasan et al. 2023; Bulichi et al. 2024), with a hint of a reversal with increasing sSFR in the vicinity of filaments (Bulichi et al. 2024). *Euclid* will allow us to test these predictions, and extend to higher redshifts our knowledge on the impact of the cosmic web on the star-formation activity of galaxies.

Low-redshift studies, both observational and numerical, also highlight the important role of connectivity (and multiplicity) of the cosmic web in shaping galaxy properties beyond their stellar mass. At fixed M_* , galaxies at the nodes of the cosmic web with higher number of connected filaments tend to have lower

sSFR and to be less rotationally supported compared to galaxies with lower connectivity (Kraljic et al. 2020b). As connectivity is a practical observational proxy for past and present accretion of galaxies and therefore controls their assembly history, it is of great importance to extend this kind of study to higher redshifts. *Euclid* will allow us to infer the cosmic evolution of connectivity (and multiplicity) of the cosmic web and its impact on various galaxy properties, such as sSFR, morphology, but also metallicity, to name a few. In particular, detailed morphological information will be obtained from photometry (with various methods: profile-fitting, non-parametric estimates, deep learning; *Euclid* Collaboration: Bretonnière et al. 2023) provided by the VIS instrument (Euclid Collaboration: Cropper et al. 2025). The Euclid pipeline includes a model-fitting algorithm evaluated through the Euclid Morphology Challenge using simulated datasets. *Euclid* is expected to deliver robust structural parameters for more than 400 million galaxies, with a less than 10% scatter for single Sérsic profiles down to $I_E = 23$ and double Sérsic profiles down to $I_E = 21$. For complex morphologies, performance can be improved using the Zoobot CNN and larger crowd-sourced datasets. Zoobot's adaptability to new morphological labels was demonstrated with peculiar galaxies, highlighting its utility for detailed Euclid catalogues (Euclid Collaboration: Aussel et al. 2024).

Besides morphology measurements, the VIS instrument will provide precise estimates of the position angle of galaxies that jointly with access to large-scale structure will enable us to investigate the alignment of angular momentum (or spin) of galaxies with respect to the filaments and walls of the cosmic web. At low redshifts ($z \lesssim 0.2$), statistical studies using data from the SDSS, SDSS-IV MaNGA and SAMI surveys revealed that rotationally supported, disk-dominated low-mass galaxies tend to have their spin aligned with their neighbouring filaments and walls, while bulge-dominated (S0-type) massive galaxies have their spin preferentially in the perpendicular direction (e.g., Tempel et al. 2013; Tempel & Libeskind 2013; Welker et al. 2020; Kraljic et al. 2021). As suggested by hydrodynamical cosmological simulations, such a spin alignment signal is expected to be stronger at $z \gtrsim 1$ (e.g., Dubois et al. 2014; Codis et al. 2018a; Wang et al. 2018; Kraljic et al. 2020a), making the EDS an ideal data set for measuring the 3D orientation of galaxies' angular momentum with respect to large-scale filaments and walls at high redshift.

Understanding the co-evolution of galaxies and large-scale structure is of interest not only in the context of galaxy formation and evolution, but it is also of paramount importance for cosmology. An important example is the spin alignment of galaxies with regard to large-scale structure, as it is a known source of contamination for weak-lensing-based dark energy surveys (e.g., Chisari et al. 2017). Another example is cosmic connectivity and its evolution that is expected to depend on cosmology (e.g., Codis et al. 2018b; Mainieri et al. 2024; Boldrini & Laigle 2025) and therefore may be an interesting probe of cosmological models beyond Λ CDM. Beyond connectivity, other cosmic web properties, such as exclusion zones present in the cross-correlations of critical points of the density field that were found to behave as standard rulers, represent a promising tool for constraining cosmological parameters (Shim et al. 2024).

4.3. Synergies with other surveys

Connecting the evolution of galaxies and the large-scale cosmic web requires spectroscopic surveys with high spatial sampling across a wide area in order to properly sample a wide range of

cosmic environments. The EDS will in this regard be complementary to the PFS Galaxy Evolution survey (PFS hereafter; Greene et al. 2022). The PFS main continuum-selected sample of $\sim 3 \times 10^5$ galaxies with $J < 22.8$ in the redshift range $0.7 \lesssim z \lesssim 1.7$ will allow one to capture $\sim 90\%$ of the population with $M_* \gtrsim 10^{10} M_\odot$. With 70% average completeness, PFS will enable the observation of multiple galaxies in groups with halo masses down to $\sim 10^{13} M_\odot$. This makes it ideal not only for studying the assembly history of galaxy groups, but also for the cosmic web-related analysis, thanks to an improved reconstruction of the large-scale structure (Kraljic et al. in prep.).

The EDS is also complementary to MOONRISE (the main Guaranteed Time Observation MOONS extra-galactic survey at the VLT; Maiolino et al. 2020), an upcoming massively multiplexed spectroscopic survey that enables the study of galaxy properties with rest-frame optical line coverage up to $z \sim 2$. With its unique observing capabilities and strategy, MOONS is expected to capture the environment of galaxies across four orders of magnitude in over-density, from large under-dense void regions to high-density groups and clusters at $z \sim 1$ –2. This will, in turn, allow for the reconstruction of the cosmic web, particularly the filaments connected to galaxy clusters, and facilitate the study of their impact on galaxy properties at the peak of the cosmic star-formation rate in the Universe.

In the comparable redshift range $z \sim 1$ –2, additional complementarity will be provided by the planned Nancy Grace Roman Space Telescope (Roman; Akeson et al. 2019). Galaxy samples from Roman's deeper observations with the High-Latitude Wide-Area Survey (HLWAS; Wang et al. 2022), in particular its "Deep" and "Ultra-Deep" tiers covering respectively ~ 19 and $\sim 5 \text{ deg}^2$ areas, are expected to allow for a reconstruction of the cosmic web with a mean galaxy number density comparable to that of EDS (Hasan et al. 2025). However, thanks to the larger wavelength coverage of Roman grisms, the emission lines [OIII] will be detectable beyond $z \sim 1.9$, extending the Roman redshift coverage to $z \sim 2.8$ (Zhai et al. 2021). This represents a true complementarity to Euclid, pushing potentially the cosmic web reconstruction in 3D to even higher redshifts.

Another potential complementarity with the EDS will be offered, at lower redshifts, by DESI, which is already collecting spectra (e.g., DESI Collaboration et al. 2024, 2025). In particular, the DESI magnitude-limited Bright Galaxy Survey (BGS; Hahn et al. 2023), comprising approximately ten million galaxies over the redshift range $0 < z < 0.6$, will provide a galaxy sample up to two magnitudes fainter than the SDSS Main Galaxy Sample (Strauss et al. 2002), with doubled median redshift ($z \approx 0.2$). With significantly higher number density than any previous survey in this redshift range, spectra and photometry for ten million galaxies, BGS will enable measurements of their physical properties and the reconstruction of the cosmic web in three dimensions. This will in turn enable studies of the connection between the large-scale environment and galaxies, by focusing on their properties and statistics, e.g. the mass-metallicity relation, the star-forming main sequence, stellar mass and luminosity functions at lower redshifts.

Finally, the Spectro-Photometer for the History of the Universe, Epoch of Reionization and Ices Explorer (SPHEREx, Bock et al. 2025) and the Vera C. Rubin Observatory's Legacy Survey of Space and Time (LSST, Ivezic et al. 2019) will both provide photometric data on wavelength range complementary to the Euclid ground-based and NIR photometric filters. On the one hand, SPHEREx, launched on 11 March 2025, will provide an all-sky low-resolution spectro-photometric survey in 102 narrow-bands from 0.75 to 5.0 μm , at a depth comparable to the

Euclid spectroscopic survey but with much lower spatial (6''.2 pixels) and spectral ($\lambda/\Delta\lambda = 35 - 130$) resolutions. The EDFs and SPHEREx deep fields are planned to overlap (Doré et al. 2018), making SPHEREx a tool of choice to mitigate the fraction of catastrophic outliers in the *Euclid* spectroscopic survey, by providing additional constraints for line identification on a larger wavelength range. On the other hand, LSST, will provide a 18000 deg² coverage of the south hemisphere, hence overlapping with EDFs and EDFF. In these fields, LSST will provide deep optical photometry in six filters *ugrizy* covering the wavelength range 0.32 to 1.05 μm (in a range where *Euclid* has only one broad-band). This photometry could also be used to help tuning the spectroscopic solution of galaxies in the spectroscopic EDS. Beyond constraining the redshifts, these photometric data will be valuable to improve the stellar mass measurements of the *Euclid* galaxies, which in turn is pivotal to weight the density field at the stage of skeleton extraction.

5. Conclusions

In this study, we have investigated the quality of the reconstruction of the cosmic web with the expected spectroscopic dataset of galaxies in the EDFs in the redshift range $0.4 < z < 1.8$, and with an H α flux limit of $6 \times 10^{-17} \text{ erg cm}^{-2} \text{ s}^{-1}$. This analysis was carried out using the Flagship and GAEA mock galaxy catalogues.

Our main findings are the following:

- Geometry of the cosmic web: The small-scale redshift-space distortions strongly impact the cosmic web reconstruction, its filamentary network in particular, regardless of the sample selection (H α flux- or M_* -limited) and regardless of what weighting of the tessellation by the stellar mass of galaxies is chosen. The correction applied for the FoG effect works better for stellar mass-limited samples. In addition to sample selection, the redshift uncertainties hinder our ability to correct for the FoG effect.
- Connectivity of the cosmic web: For the overall properties of the PDF of the connectivity, the correction of the FoG effect works very well for the M_* -limited sample and reasonably well for the H α flux-limited sample. Weighting the tessellation by stellar mass for the H α flux-based selection artificially enhances the connectivity, even in the absence of redshift-space distortions. Adding noise and incompleteness reduces the quality of the cosmic web reconstruction for both H α -based and M_* -based galaxy selections, due to the diminished ability to correct for FoG effects. In this configuration, stellar mass weighting of the tessellation significantly improves the cosmic web reconstruction, particularly for an H α -based galaxy selection. Weighting is similarly crucial to recover the M_* -connectivity relation when the sample is H α flux-limited, in the presence of redshift errors, and for reduced sampling.
- Multiplicity of the cosmic web: For H α flux-limited samples, rather than M_* -limited samples, the multiplicity appears to be a more robust quantity compared to the connectivity. Even without weighting the tessellation, the applied correction for the FoG effect enables us to recover the M_* -multiplicity relation. This holds true even in the presence of redshift errors and reduced sampling.
- Stellar-mass gradients: Stellar-mass gradients, where more massive galaxies are preferentially located closer to filaments compared to their lower-mass counterparts, are recovered regardless of whether the tessellation is weighted by

stellar mass. However, the redshift error and limited sampling significantly weaken the strength of the measured signal for the H α flux-limited sample in the absence of tessellation weighting.

In this work, we performed the cosmic web reconstruction in three dimensions, using simulated spectroscopic redshifts in the range $0.4 < z < 1.8$, expected in EDFs. The reconstruction methodology will therefore be applicable once the EDS data will be available and the performance of spectroscopic measurements fully assessed in this redshift range. The first results using the *Euclid* Quick Data Release (Q1) of the Spectroscopic Processing Functions of the *Euclid* pipeline (Euclid Collaboration: Le Brun et al. 2025) in the redshift range $0.9 < z < 1.8$ are promising. It was shown that a success rate above 80%, and excellent redshift precision ($\sim 10^{-3}$) and accuracy (better than 3×10^{-5}) can be reached in only one visit. The final EDS will be made of about 40 visits and with much better performance.

The analysis of the cosmic web in two dimensions using photometric redshifts from the Q1 release, focused on the galaxy morphology and shape alignments at $0.5 < z < 0.9$, is presented in Euclid Collaboration: Laigle et al. (2025), while in Euclid Collaboration: Gouin et al. (2025), the focus is on cosmic connectivity of galaxy clusters at $0.2 < z < 0.7$.

This work was focused on the technical aspects of cosmic web reconstruction, with the goal of providing guidelines for future applications to real data. For this reason, we specifically only considered trends with the stellar mass of galaxies, leaving the exploration of the impact of the cosmic web on other galaxy properties for future studies. *Euclid* will enable such an investigation for the first time across cosmic time, up to $z \approx 1.8$.

Acknowledgements. The Euclid Consortium acknowledges the European Space Agency and a number of agencies and institutes that have supported the development of *Euclid*, in particular the Agenzia Spaziale Italiana, the Austrian Forschungsförderungsgesellschaft funded through BMIMI, the Belgian Science Policy, the Canadian Euclid Consortium, the Deutsches Zentrum für Luft- und Raumfahrt, the DTU Space and the Niels Bohr Institute in Denmark, the French Centre National d'Etudes Spatiales, the Fundação para a Ciência e a Tecnologia, the Hungarian Academy of Sciences, the Ministerio de Ciencia, Innovación y Universidades, the National Aeronautics and Space Administration, the National Astronomical Observatory of Japan, the Nederlandse Onderzoekschool Voor Astronomie, the Norwegian Space Agency, the Research Council of Finland, the Romanian Space Agency, the State Secretariat for Education, Research, and Innovation (SERI) at the Swiss Space Office (SSO), and the United Kingdom Space Agency. A complete and detailed list is available on the *Euclid* web site (www.euclid-ec.org). This work has made use of CosmoHub, developed by PIC (maintained by IFAE and CIEMAT) in collaboration with ICE-CSIC. CosmoHub received funding from the Spanish government (MCIN/AEI/10.13039/501100011033), the EU NextGeneration/PRTR (PRTR-C17.II), and the Generalitat de Catalunya. This work is partially supported by the grant *SEGAL* ANR-19-CE31-0017 of the French Agence Nationale de la Recherche. This research has made use of computing facilities operated by CeSAM data centre at LAM, Marseille, France. We thank Stéphane Rouberol for the smooth running of the Infinity cluster, where part of the computations was performed.

References

Abazajian, K. N., Adelman-McCarthy, J. K., Agüeros, M. A., et al. 2009, ApJS, 182, 543
 Akeson, R., Armus, L., Bachelet, E., et al. 2019, arXiv e-prints, arXiv:1902.05569
 Angulo, R. E., Zennaro, M., Contreras, S., et al. 2021, MNRAS, 507, 5869
 Baldry, I. K., Balogh, M. L., Bower, R. G., et al. 2006, MNRAS, 373, 469
 Bamford, S. P., Nichol, R. C., Baldry, I. K., et al. 2009, MNRAS, 393, 1324
 Barsanti, S., Colless, M., Welker, C., et al. 2022, MNRAS, 516, 3569
 Behroozi, P. S., Wechsler, R. H., & Wu, H.-Y. 2013, ApJ, 762, 109
 Blanton, M. R., Hogg, D. W., Bahcall, N. A., et al. 2003a, ApJ, 594, 186
 Blanton, M. R., Hogg, D. W., Bahcall, N. A., et al. 2003b, ApJ, 592, 819

Blanton, M. R., Lupton, R. H., Schlegel, D. J., et al. 2005, *ApJ*, 631, 208

Bock, J. J., Aboobaker, A. M., Adamo, J., et al. 2025, accepted by *ApJ*, arXiv:2511.02985

Boldrini, P. & Laigle, C. 2025, *A&A*, 700, A182

Bond, J. R., Kofman, L., & Pogosyan, D. 1996, *Nature*, 380, 603

Bond, J. R. & Myers, S. T. 1996, *ApJS*, 103, 1

Bulichi, T.-E., Davé, R., & Kraljic, K. 2024, *MNRAS*, 529, 2595

Burton, C. S., Jarvis, M. J., Smith, D. J. B., et al. 2013, *MNRAS*, 433, 771

Calzetti, D., Armus, L., Bohlin, R. C., et al. 2000, *ApJ*, 533, 682

Carretero, J., Tallada, P., Casals, J., et al. 2017, in *Proceedings of the European Physical Society Conference on High Energy Physics*. 5-12 July, 488

Chabrier, G. 2003, *PASP*, 115, 763

Chen, Y.-C., Ho, S., Mandelbaum, R., et al. 2017, *MNRAS*, 466, 1880

Chisari, N. E., Koukoufilippas, N., Jindal, A., et al. 2017, *MNRAS*, 472, 1163

Codis, S., Jindal, A., Chisari, N. E., et al. 2018a, *MNRAS*, 481, 4753

Codis, S., Pichon, C., & Pogosyan, D. 2015, *MNRAS*, 452, 3369

Codis, S., Pogosyan, D., & Pichon, C. 2018b, *MNRAS*, 479, 973

Colbert, J. W., Teplitz, H., Atek, H., et al. 2013, *ApJ*, 779, 34

Colless, M., Dalton, G., Maddox, S., et al. 2001, *MNRAS*, 328, 1039

Cranmer, K., Brehmer, J., & Louppe, G. 2020, *Proceedings of the National Academy of Science*, 117, 30055

Crone Odekon, M., Hallenbeck, G., Haynes, M. P., et al. 2018, *ApJ*, 852, 142

Cucciati, O., Davidzon, I., Bolzonella, M., et al. 2017, *A&A*, 602, A15

Cucciati, O., Iovino, A., Kovač, K., et al. 2010, *A&A*, 524, A2

Darragh Ford, E., Laigle, C., Gozaliasl, G., et al. 2019, *MNRAS*, 489, 5695

Davis, M. & Geller, M. J. 1976, *ApJ*, 208, 13

Davis, M., Huchra, J., Latham, D. W., & Tonry, J. 1982, *ApJ*, 253, 423

de Lapparent, V., Geller, M. J., & Huchra, J. P. 1986, *ApJ*, 302, L1

De Lucia, G., Tornatore, L., Frenk, C. S., et al. 2014, *MNRAS*, 445, 970

DESI Collaboration, Abdul-Karim, M., Adame, A. G., Aguado, D., et al. 2025, submitted to *ApJ*, arXiv:2503.14745

DESI Collaboration, Adame, A. G., Aguilera, J., et al. 2024, *AJ*, 168, 58

DESI Collaboration, Aghamousa, A., Aguilera, J., et al. 2016, arXiv e-prints, arXiv:1611.00036

Donnan, C. T., Tojeiro, R., & Kraljic, K. 2022, *Nature Astronomy*, 6, 599

Doré, O., Werner, M. W., Ashby, M. L. N., et al. 2018, arXiv e-prints, arXiv:1805.05489

Dressler, A. 1980, *ApJ*, 236, 351

Dressler, A., Oemler, Augustus, J., Couch, W. J., et al. 1997, *ApJ*, 490, 577

Driver, S. P., Hill, D. T., Kelvin, L. S., et al. 2011, *MNRAS*, 413, 971

Duarte, M. & Mamon, G. A. 2014, *MNRAS*, 440, 1763

Dubois, Y., Pichon, C., Welker, C., et al. 2014, *MNRAS*, 444, 1453

Efstathiou, G., Frenk, C. S., White, S. D. M., & Davis, M. 1988, *MNRAS*, 235, 715

Einasto, M., Deshev, B., Tenjes, P., et al. 2020, *A&A*, 641, A172

Einasto, M., Kipper, R., Tenjes, P., et al. 2021, *A&A*, 649, A51

Euclid Collaboration: Aussel, B., Kruk, S., Walmsley, M., et al. 2024, *A&A*, 689, A274

Euclid Collaboration: Bretonnière, H., Kuchner, U., Huertas-Company, M., et al. 2023, *A&A*, 671, A102

Euclid Collaboration: Castander, F., Fosalba, P., Stadel, J., et al. 2025, *A&A*, 697, A5

Euclid Collaboration: Copin, Y., Fumana, M., Mancini, C., et al. 2025, *A&A*, in press (Euclid Q1 SI), <https://doi.org/10.1051/0004-6361/202554627>, arXiv:2503.15307

Euclid Collaboration: Cropper, M., Al-Bahlawan, A., Amiaux, J., et al. 2025, *A&A*, 697, A2

Euclid Collaboration: Gouin, C., Laigle, C., Sarron, F., et al. 2025, *A&A*, submitted (Euclid Q1 SI), arXiv:2503.15332

Euclid Collaboration: Laigle, C., Gouin, C., Sarron, F., et al. 2025, *A&A*, in press (Euclid Q1 SI), <https://doi.org/10.1051/0004-6361/202554651>, arXiv:2503.15333

Euclid Collaboration: Le Brun, V., Bethermin, M., Moresco, M., et al. 2025, *A&A*, accepted (Euclid Q1 SI), arXiv:2503.15308

Euclid Collaboration: Malavasi, N., Sarron, F., Kuchner, U., et al. 2025, *A&A* submitted, arXiv:2508.15915

Euclid Collaboration: McPartland, C. J. R., Zalesky, L., Weaver, J. R., et al. 2025, *A&A*, 695, A259

Euclid Collaboration: Mellier, Y., Abdurro'uf, Acevedo Barroso, J., et al. 2025, *A&A*, 697, A1

Euclid Collaboration: Scaramella, R., Amiaux, J., Mellier, Y., et al. 2022, *A&A*, 662, A112

Euclid Collaboration: Zalesky, L., McPartland, C. J. R., Weaver, J. R., et al. 2025, *A&A*, 695, A229

Fontanot, F., De Lucia, G., Hirschmann, M., et al. 2020, *MNRAS*, 496, 3943

Fontanot, F., Hirschmann, M., & De Lucia, G. 2017, *ApJ*, 842, L14

Forman, R. 2001, Séminaire Lothar. Combin., 48

Galárraga-Espinosa, D., Cadiou, C., Gouin, C., et al. 2024, *A&A*, 684, A63

Goto, T., Yamauchi, C., Fujita, Y., et al. 2003, *MNRAS*, 346, 601

Greene, J., Bezanson, R., Ouchi, M., Silverman, J., & the PFS Galaxy Evolution Working Group. 2022, arXiv e-prints, arXiv:2206.14908

Guzzo, L., Scoglio, M., Garilli, B., et al. 2014, *A&A*, 566, A108

Hahn, C., Wilson, M. J., Ruiz-Macias, O., et al. 2023, *AJ*, 165, 253

Hamaus, N., Aubert, M., Pisani, A., et al. 2022, *A&A*, 658, A20

Hasan, F., Burchett, J. N., Abeyta, A., et al. 2023, *ApJ*, 950, 114

Hasan, F., Zhang, H., Pandya, V., et al. 2025, submitted to *ApJ*, arXiv:2509.23549

Hirschmann, M., De Lucia, G., & Fontanot, F. 2016, *MNRAS*, 461, 1760

Hou, J., Dizgah, A. M., Hahn, C., et al. 2024, *Phys. Rev. D*, 109, 103528

Ivezić, Ž., Kahn, S. M., Tyson, J. A., et al. 2019, *ApJ*, 873, 111

Jackson, J. C. 1972, *MNRAS*, 156, 1P

Jones, D. H., Read, M. A., Saunders, W., et al. 2009, *MNRAS*, 399, 683

Jones, D. H., Saunders, W., Colless, M., et al. 2004, *MNRAS*, 355, 747

Kaiser, N. 1984, *ApJ*, 284, L9

Kennicutt, Jr., R. C. 1998, *ARA&A*, 36, 189

Kennicutt, Jr., R. C., Tamblyn, P., & Congdon, C. E. 1994, *ApJ*, 435, 22

Kirshner, R. P., Oemler, A. J., Schechter, P. L., & Shectman, S. A. 1981, *ApJ*, 248, L57

Kleiner, D., Pimbblet, K. A., Jones, D. H., Koribalski, B. S., & Serra, P. 2017, *MNRAS*, 466, 4692

Klypin, A. & Shandarin, S. F. 1993, *ApJ*, 413, 48

Klypin, A. A. & Shandarin, S. F. 1983, *MNRAS*, 204, 891

Kobayashi, Y., Nishimichi, T., Takada, M., & Miyatake, H. 2022, *Phys. Rev. D*, 105, 083517

Kraljic, K., Arnouts, S., Pichon, C., et al. 2018, *MNRAS*, 474, 547

Kraljic, K., Davé, R., & Pichon, C. 2020a, *MNRAS*, 493, 362

Kraljic, K., Duckworth, C., Tojeiro, R., et al. 2021, *MNRAS*, 504, 4626

Kraljic, K., Pichon, C., Codis, S., et al. 2020b, *MNRAS*, 491, 4294

Krolewski, A., Ho, S., Chen, Y.-C., et al. 2019, *ApJ*, 876, 52

Kuutma, T., Tamm, A., & Tempel, E. 2017, *A&A*, 600, L6

Laigle, C., Pichon, C., Arnouts, S., et al. 2018, *MNRAS*, 474, 5437

Landy, S. D. & Szalay, A. S. 1993, *ApJ*, 412, 64

Laureijs, R., Amiaux, J., Arduini, S., et al. 2011, *ESA/SRE(2011)12*, arXiv:1110.3193

Lee, J. & Erdogdu, P. 2007, *ApJ*, 671, 1248

Lee, K.-G. & White, M. 2016, *ApJ*, 831, 181

Libeskind, N. I., van de Weygaert, R., Cautun, M., et al. 2018, *MNRAS*, 473, 1195

Lynden-Bell, D. 1964, *ApJ*, 139, 1195

Madau, P. & Dickinson, M. 2014, *ARA&A*, 52, 415

Mainieri, V., Anderson, R. I., Brinchmann, J., et al. 2024, arXiv e-prints, arXiv:2403.05398

Maiolino, R., Cirasuolo, M., Afonso, J., et al. 2020, *The Messenger*, 180, 24

Malavasi, N., Arnouts, S., Vibert, D., et al. 2017, *MNRAS*, 465, 3817

McCullough, J., Gruen, D., Amon, A., et al. 2024, *MNRAS*, 531, 2582

Musso, M., Cadiou, C., Pichon, C., et al. 2018, *MNRAS*, 476, 4877

Pahwa, I., Libeskind, N. I., Tempel, E., et al. 2016, *MNRAS*, 457, 695

Pogosyan, D., Bond, J. R., Kofman, L., & Wadsley, J. 1996, in *American Astronomical Society Meeting Abstracts*, Vol. 189, American Astronomical Society Meeting Abstracts, 13.03

Pogosyan, D., Pichon, C., Gay, C., et al. 2009, *MNRAS*, 396, 635

Popesso, P., Concas, A., Cresci, G., et al. 2023, *MNRAS*, 519, 1526

Potter, D. & Stadel, J. 2016, *PKDGRAV3: Parallel gravity code*, *Astrophysics Source Code Library*, record ascl:1609.016

Pozzetti, L., Hirata, C. M., Geach, J. E., et al. 2016, *A&A*, 590, A3

Ravoux, C., Armengaud, E., Walther, M., et al. 2020, *JCAP*, 07, 010

Robotham, A. S. G., Norberg, P., Driver, S. P., et al. 2011, *MNRAS*, 416, 2640

Saito, S., de la Torre, S., Ilbert, O., et al. 2020, *MNRAS*, 494, 199

Sarron, F., Adami, C., Durret, F., & Laigle, C. 2019, *A&A*, 632, A49

Schaap, W. E. & van de Weygaert, R. 2000, *A&A*, 363, L29

Schäfer, B. M. 2009, *International Journal of Modern Physics D*, 18, 173

Shectman, S. A., Landy, S. D., Oemler, A., et al. 1996, *ApJ*, 470, 172

Shim, H., Colbert, J., Teplitz, H., et al. 2009, *ApJ*, 696, 785

Shim, J., Pichon, C., Pogosyan, D., et al. 2024, *MNRAS*, 528, 1604

Shuntov, M., McCracken, H. J., Gavazzi, R., et al. 2022, *A&A*, 664, A61

Smith, R., Hwang, H. S., Kraljic, K., et al. 2023, *MNRAS*, 525, 4685

Sobral, D., Smail, I., Best, P. N., et al. 2013, *MNRAS*, 428, 1128

Sousbie, T. 2011, *MNRAS*, 414, 350

Sousbie, T., Pichon, C., & Kawahara, H. 2011, *MNRAS*, 414, 384

Springel, V., White, S. D. M., Jenkins, A., et al. 2005, *Nature*, 435, 629

Springel, V., Yoshida, N., & White, S. D. M. 2001, *New A*, 6, 79

Strauss, M. A., Weinberg, D. H., Lupton, R. H., et al. 2002, *AJ*, 124, 1810

Tallada, P., Carretero, J., Casals, J., et al. 2020, *Astronomy and Computing*, 32, 100391

Tegmark, M., Blanton, M. R., Strauss, M. A., et al. 2004, *ApJ*, 606, 702

Tempel, E. & Libeskind, N. I. 2013, *ApJ*, 775, L42

Tempel, E., Stoica, R. S., & Saar, E. 2013, *MNRAS*, 428, 1827

Treyer, M., Kraljic, K., Arnouts, S., et al. 2018, *MNRAS*, 477, 2684

Wang, P., Guo, Q., Kang, X., & Libeskind, N. I. 2018, *ApJ*, 866, 138

Wang, Y., Zhai, Z., Alavi, A., et al. 2022, *ApJ*, 928, 1
 Welker, C., Bland-Hawthorn, J., van de Sande, J., et al. 2020, *MNRAS*, 491, 2864
 Winkel, N., Pasquali, A., Kraljic, K., et al. 2021, *MNRAS*, 505, 4920
 Xu, W., Guo, Q., Zheng, H., et al. 2020, *MNRAS*, 498, 1839
 York, D. G., Adelman, J., Anderson, John E., J., et al. 2000, *AJ*, 120, 1579
 Zehavi, I., Zheng, Z., Weinberg, D. H., et al. 2011, *ApJ*, 736, 59
 Zel'dovich, Y. B. 1970, *A&A*, 5, 84
 Zhai, Z., Wang, Y., Benson, A., et al. 2021, arXiv e-prints, arXiv:2109.12216
 Zhang, Y., Yang, X., Wang, H., et al. 2015, *ApJ*, 798, 17
 Zhang, Y., Yang, X., Wang, H., et al. 2013, *ApJ*, 779, 160
 Zoldan, A., De Lucia, G., Xie, L., Fontanot, F., & Hirschmann, M. 2017, *MNRAS*, 465, 2236

¹ Université de Strasbourg, CNRS, Observatoire astronomique de Strasbourg, UMR 7550, 67000 Strasbourg, France
² Institut d'Astrophysique de Paris, UMR 7095, CNRS, and Sorbonne Université, 98 bis boulevard Arago, 75014 Paris, France
³ Department of Physics and Astronomy, University of Waterloo, Waterloo, Ontario N2L 3G1, Canada
⁴ Waterloo Centre for Astrophysics, University of Waterloo, Waterloo, Ontario N2L 3G1, Canada
⁵ Institute of Physics, Laboratory of Astrophysics, Ecole Polytechnique Fédérale de Lausanne (EPFL), Observatoire de Sauverny, 1290 Versoix, Switzerland
⁶ School of Physics and Astronomy, University of Nottingham, University Park, Nottingham NG7 2RD, UK
⁷ Max Planck Institute for Extraterrestrial Physics, Giessenbachstr. 1, 85748 Garching, Germany
⁸ Institut de Recherche en Informatique de Toulouse (IRIT), Université de Toulouse, CNRS, Toulouse INP, UT3, 31062 Toulouse, France
⁹ Laboratoire MCD, Centre de Biologie Intégrative (CBI), Université de Toulouse, CNRS, UT3, 31062 Toulouse, France
¹⁰ Kyung Hee University, Dept. of Astronomy & Space Science, Yongin-shi, Gyeonggi-do 17104, Republic of Korea
¹¹ INAF-Osservatorio Astronomico di Trieste, Via G. B. Tiepolo 11, 34143 Trieste, Italy
¹² Institut d'Astrophysique de Paris, 98bis Boulevard Arago, 75014, Paris, France
¹³ Dipartimento di Fisica "G. Occhialini", Università degli Studi di Milano Bicocca, Piazza della Scienza 3, 20126 Milano, Italy
¹⁴ INAF-Istituto di Astrofisica e Planetologia Spaziali, via del Fosso del Cavaliere, 100, 00100 Roma, Italy
¹⁵ Univ. Lille, CNRS, Centrale Lille, UMR 9189 CRISTAL, 59000 Lille, France
¹⁶ Université Paris-Saclay, CNRS, Institut d'astrophysique spatiale, 91405, Orsay, France
¹⁷ INAF-Osservatorio di Astrofisica e Scienza dello Spazio di Bologna, Via Piero Gobetti 93/3, 40129 Bologna, Italy
¹⁸ IFPU, Institute for Fundamental Physics of the Universe, via Beirut 2, 34151 Trieste, Italy
¹⁹ Institute of Physics, Laboratory for Galaxy Evolution, Ecole Polytechnique Fédérale de Lausanne, Observatoire de Sauverny, CH-1290 Versoix, Switzerland
²⁰ Department of Astronomy, University of Geneva, ch. d'Ecogia 16, 1290 Versoix, Switzerland
²¹ Université Côte d'Azur, Observatoire de la Côte d'Azur, CNRS, Laboratoire Lagrange, Bd de l'Observatoire, CS 34229, 06304 Nice cedex 4, France
²² Department of Physics and Astronomy, University of the Western Cape, Bellville, Cape Town, 7535, South Africa
²³ School of Mathematics and Physics, University of Surrey, Guildford, Surrey, GU2 7XH, UK
²⁴ INAF-Osservatorio Astronomico di Brera, Via Brera 28, 20122 Milano, Italy
²⁵ INFN, Sezione di Trieste, Via Valerio 2, 34127 Trieste TS, Italy
²⁶ SISSA, International School for Advanced Studies, Via Bonomea 265, 34136 Trieste TS, Italy
²⁷ Dipartimento di Fisica e Astronomia, Università di Bologna, Via Gobetti 93/2, 40129 Bologna, Italy
²⁸ INFN-Sezione di Bologna, Viale Berti Pichat 6/2, 40127 Bologna, Italy
²⁹ Dipartimento di Fisica, Università di Genova, Via Dodecaneso 33, 16146, Genova, Italy
³⁰ INFN-Sezione di Genova, Via Dodecaneso 33, 16146, Genova, Italy
³¹ Department of Physics "E. Pancini", University Federico II, Via Cinthia 6, 80126, Napoli, Italy
³² INAF-Osservatorio Astronomico di Capodimonte, Via Moiariello 16, 80131 Napoli, Italy
³³ Instituto de Astrofísica e Ciências do Espaço, Universidade do Porto, CAUP, Rua das Estrelas, PT4150-762 Porto, Portugal
³⁴ Faculdade de Ciências da Universidade do Porto, Rua do Campo de Alegre, 4150-007 Porto, Portugal
³⁵ European Southern Observatory, Karl-Schwarzschild-Str. 2, 85748 Garching, Germany
³⁶ Dipartimento di Fisica, Università degli Studi di Torino, Via P. Giuria 1, 10125 Torino, Italy
³⁷ INFN-Sezione di Torino, Via P. Giuria 1, 10125 Torino, Italy
³⁸ INAF-Osservatorio Astrofisico di Torino, Via Osservatorio 20, 10025 Pino Torinese (TO), Italy
³⁹ European Space Agency/ESTEC, Keplerlaan 1, 2201 AZ Noordwijk, The Netherlands
⁴⁰ Institute Lorentz, Leiden University, Niels Bohrweg 2, 2333 CA Leiden, The Netherlands
⁴¹ Leiden Observatory, Leiden University, Einsteinweg 55, 2333 CC Leiden, The Netherlands
⁴² INAF-IASF Milano, Via Alfonso Corti 12, 20133 Milano, Italy
⁴³ Centro de Investigaciones Energéticas, Medioambientales y Tecnológicas (CIEMAT), Avenida Complutense 40, 28040 Madrid, Spain
⁴⁴ Port d'Informació Científica, Campus UAB, C. Albareda s/n, 08193 Bellaterra (Barcelona), Spain
⁴⁵ Institut d'Estudis Espacials de Catalunya (IEEC), Edifici RDIT, Campus UPC, 08860 Castelldefels, Barcelona, Spain
⁴⁶ Institute of Space Sciences (ICE, CSIC), Campus UAB, Carrer de Can Magrans, s/n, 08193 Barcelona, Spain
⁴⁷ Institute for Theoretical Particle Physics and Cosmology (TTK), RWTH Aachen University, 52056 Aachen, Germany
⁴⁸ INAF-Osservatorio Astronomico di Roma, Via Frascati 33, 00078 Monteporzio Catone, Italy
⁴⁹ INFN section of Naples, Via Cinthia 6, 80126, Napoli, Italy
⁵⁰ Institute for Astronomy, University of Hawaii, 2680 Woodlawn Drive, Honolulu, HI 96822, USA
⁵¹ Dipartimento di Fisica e Astronomia "Augusto Righi" - Alma Mater Studiorum Università di Bologna, Viale Berti Pichat 6/2, 40127 Bologna, Italy
⁵² Instituto de Astrofísica de Canarias, Vía Láctea, 38205 La Laguna, Tenerife, Spain
⁵³ Institute for Astronomy, University of Edinburgh, Royal Observatory, Blackford Hill, Edinburgh EH9 3HJ, UK
⁵⁴ Jodrell Bank Centre for Astrophysics, Department of Physics and Astronomy, University of Manchester, Oxford Road, Manchester M13 9PL, UK
⁵⁵ European Space Agency/ESRIN, Largo Galileo Galilei 1, 00044 Frascati, Roma, Italy
⁵⁶ ESAC/ESA, Camino Bajo del Castillo, s/n., Urb. Villafranca del Castillo, 28692 Villanueva de la Cañada, Madrid, Spain
⁵⁷ Université Claude Bernard Lyon 1, CNRS/IN2P3, IP2I Lyon, UMR 5822, Villeurbanne, F-69100, France
⁵⁸ Institut de Ciències del Cosmos (ICCUB), Universitat de Barcelona (IEEC-UB), Martí i Franquès 1, 08028 Barcelona, Spain
⁵⁹ Institució Catalana de Recerca i Estudis Avançats (ICREA), Passeig de Lluís Companys 23, 08010 Barcelona, Spain
⁶⁰ UCB Lyon 1, CNRS/IN2P3, IUF, IP2I Lyon, 4 rue Enrico Fermi, 69622 Villeurbanne, France
⁶¹ Departamento de Física, Faculdade de Ciências, Universidade de Lisboa, Edifício C8, Campo Grande, PT1749-016 Lisboa, Portugal

⁶² Instituto de Astrofísica e Ciências do Espaço, Faculdade de Ciências, Universidade de Lisboa, Campo Grande, 1749-016 Lisboa, Portugal

⁶³ Aix-Marseille Université, CNRS, CNES, LAM, Marseille, France

⁶⁴ INFN-Padova, Via Marzolo 8, 35131 Padova, Italy

⁶⁵ Aix-Marseille Université, CNRS/IN2P3, CPPM, Marseille, France

⁶⁶ INFN-Bologna, Via Irnerio 46, 40126 Bologna, Italy

⁶⁷ Universitäts-Sternwarte München, Fakultät für Physik, Ludwig-Maximilians-Universität München, Scheinerstrasse 1, 81679 München, Germany

⁶⁸ INAF-Osservatorio Astronomico di Padova, Via dell'Osservatorio 5, 35122 Padova, Italy

⁶⁹ Institute of Theoretical Astrophysics, University of Oslo, P.O. Box 1029 Blindern, 0315 Oslo, Norway

⁷⁰ Jet Propulsion Laboratory, California Institute of Technology, 4800 Oak Grove Drive, Pasadena, CA, 91109, USA

⁷¹ Felix Hormuth Engineering, Goethestr. 17, 69181 Leimen, Germany

⁷² Technical University of Denmark, Elektrovej 327, 2800 Kgs. Lyngby, Denmark

⁷³ Cosmic Dawn Center (DAWN), Denmark

⁷⁴ Max-Planck-Institut für Astronomie, Königstuhl 17, 69117 Heidelberg, Germany

⁷⁵ NASA Goddard Space Flight Center, Greenbelt, MD 20771, USA

⁷⁶ Department of Physics and Astronomy, University College London, Gower Street, London WC1E 6BT, UK

⁷⁷ Department of Physics and Helsinki Institute of Physics, Gustaf Hällströmin katu 2, University of Helsinki, 00014 Helsinki, Finland

⁷⁸ Université Paris-Saclay, Université Paris Cité, CEA, CNRS, AIM, 91191, Gif-sur-Yvette, France

⁷⁹ Université de Genève, Département de Physique Théorique and Centre for Astroparticle Physics, 24 quai Ernest-Ansermet, CH-1211 Genève 4, Switzerland

⁸⁰ Department of Physics, P.O. Box 64, University of Helsinki, 00014 Helsinki, Finland

⁸¹ Helsinki Institute of Physics, Gustaf Hällströmin katu 2, University of Helsinki, 00014 Helsinki, Finland

⁸² Laboratoire d'étude de l'Univers et des phénomènes eXtremes, Observatoire de Paris, Université PSL, Sorbonne Université, CNRS, 92190 Meudon, France

⁸³ SKAO, Jodrell Bank, Lower Withington, Macclesfield SK11 9FT, United Kingdom

⁸⁴ Centre de Calcul de l'IN2P3/CNRS, 21 avenue Pierre de Coubertin 69627 Villeurbanne Cedex, France

⁸⁵ Dipartimento di Fisica "Aldo Pontremoli", Università degli Studi di Milano, Via Celoria 16, 20133 Milano, Italy

⁸⁶ INFN-Sezione di Milano, Via Celoria 16, 20133 Milano, Italy

⁸⁷ University of Applied Sciences and Arts of Northwestern Switzerland, School of Computer Science, 5210 Windisch, Switzerland

⁸⁸ Universität Bonn, Argelander-Institut für Astronomie, Auf dem Hügel 71, 53121 Bonn, Germany

⁸⁹ INFN-Sezione di Roma, Piazzale Aldo Moro, 2 - c/o Dipartimento di Fisica, Edificio G. Marconi, 00185 Roma, Italy

⁹⁰ Dipartimento di Fisica e Astronomia "Augusto Righi" - Alma Mater Studiorum Università di Bologna, via Piero Gobetti 93/2, 40129 Bologna, Italy

⁹¹ Department of Physics, Institute for Computational Cosmology, Durham University, South Road, Durham, DH1 3LE, UK

⁹² Université Paris Cité, CNRS, Astroparticule et Cosmologie, 75013 Paris, France

⁹³ CNRS-UCB International Research Laboratory, Centre Pierre Binétruy, IRL2007, CPB-IN2P3, Berkeley, USA

⁹⁴ Telespazio UK S.L. for European Space Agency (ESA), Camino bajo del Castillo, s/n, Urbanizacion Villafranca del Castillo, Villanueva de la Cañada, 28692 Madrid, Spain

⁹⁵ Institut de Física d'Altes Energies (IFAE), The Barcelona Institute of Science and Technology, Campus UAB, 08193 Bellaterra (Barcelona), Spain

⁹⁶ DARK, Niels Bohr Institute, University of Copenhagen, Jagtvej 155, 2200 Copenhagen, Denmark

⁹⁷ Perimeter Institute for Theoretical Physics, Waterloo, Ontario N2L 2Y5, Canada

⁹⁸ Space Science Data Center, Italian Space Agency, via del Politecnico snc, 00133 Roma, Italy

⁹⁹ Centre National d'Etudes Spatiales – Centre spatial de Toulouse, 18 avenue Edouard Belin, 31401 Toulouse Cedex 9, France

¹⁰⁰ Institute of Space Science, Str. Atomistilor, nr. 409 Măgurele, Ilfov, 077125, Romania

¹⁰¹ Consejo Superior de Investigaciones Científicas, Calle Serrano 117, 28006 Madrid, Spain

¹⁰² Universidad de La Laguna, Departamento de Astrofísica, 38206 La Laguna, Tenerife, Spain

¹⁰³ Dipartimento di Fisica e Astronomia "G. Galilei", Università di Padova, Via Marzolo 8, 35131 Padova, Italy

¹⁰⁴ Institut für Theoretische Physik, University of Heidelberg, Philosophenweg 16, 69120 Heidelberg, Germany

¹⁰⁵ Institut de Recherche en Astrophysique et Planétologie (IRAP), Université de Toulouse, CNRS, UPS, CNES, 14 Av. Edouard Belin, 31400 Toulouse, France

¹⁰⁶ Université St Joseph; Faculty of Sciences, Beirut, Lebanon

¹⁰⁷ Departamento de Física, FCFM, Universidad de Chile, Blanco Encalada 2008, Santiago, Chile

¹⁰⁸ Universität Innsbruck, Institut für Astro- und Teilchenphysik, Technikerstr. 25/8, 6020 Innsbruck, Austria

¹⁰⁹ Satlantis, University Science Park, Sede Bld 48940, Leioa-Bilbao, Spain

¹¹⁰ Infrared Processing and Analysis Center, California Institute of Technology, Pasadena, CA 91125, USA

¹¹¹ Instituto de Astrofísica e Ciências do Espaço, Faculdade de Ciências, Universidade de Lisboa, Tapada da Ajuda, 1349-018 Lisboa, Portugal

¹¹² Cosmic Dawn Center (DAWN)

¹¹³ Niels Bohr Institute, University of Copenhagen, Jagtvej 128, 2200 Copenhagen, Denmark

¹¹⁴ Universidad Politécnica de Cartagena, Departamento de Electrónica y Tecnología de Computadoras, Plaza del Hospital 1, 30202 Cartagena, Spain

¹¹⁵ Kapteyn Astronomical Institute, University of Groningen, PO Box 800, 9700 AV Groningen, The Netherlands

¹¹⁶ Dipartimento di Fisica e Scienze della Terra, Università degli Studi di Ferrara, Via Giuseppe Saragat 1, 44122 Ferrara, Italy

¹¹⁷ Istituto Nazionale di Fisica Nucleare, Sezione di Ferrara, Via Giuseppe Saragat 1, 44122 Ferrara, Italy

¹¹⁸ INAF, Istituto di Radioastronomia, Via Piero Gobetti 101, 40129 Bologna, Italy

¹¹⁹ Astronomical Observatory of the Autonomous Region of the Aosta Valley (OAVdA), Loc. Lignan 39, I-11020, Nus (Aosta Valley), Italy

¹²⁰ Department of Physics, Oxford University, Keble Road, Oxford OX1 3RH, UK

¹²¹ Aurora Technology for European Space Agency (ESA), Camino bajo del Castillo, s/n, Urbanizacion Villafranca del Castillo, Villanueva de la Cañada, 28692 Madrid, Spain

¹²² Department of Mathematics and Physics E. De Giorgi, University of Salento, Via per Arnesano, CP-193, 73100, Lecce, Italy

¹²³ INFN, Sezione di Lecce, Via per Arnesano, CP-193, 73100, Lecce, Italy

¹²⁴ INAF-Sezione di Lecce, c/o Dipartimento Matematica e Fisica, Via per Arnesano, 73100, Lecce, Italy

¹²⁵ INAF - Osservatorio Astronomico di Brera, via Emilio Bianchi 46, 23807 Merate, Italy

¹²⁶ INAF-Osservatorio Astronomico di Brera, Via Brera 28, 20122 Milano, Italy, and INFN-Sezione di Genova, Via Dodecaneso 33, 16146, Genova, Italy

¹²⁷ ICL, Junia, Université Catholique de Lille, LITL, 59000 Lille, France

¹²⁸ ICSC - Centro Nazionale di Ricerca in High Performance Computing, Big Data e Quantum Computing, Via Magnanelli 2, Bologna, Italy

¹²⁹ Instituto de Física Teórica UAM-CSIC, Campus de Cantoblanco, 28049 Madrid, Spain

¹³⁰ CERCA/ISO, Department of Physics, Case Western Reserve University, 10900 Euclid Avenue, Cleveland, OH 44106, USA

¹³¹ Technical University of Munich, TUM School of Natural Sciences, Physics Department, James-Franck-Str. 1, 85748 Garching, Germany

¹³² Max-Planck-Institut für Astrophysik, Karl-Schwarzschild-Str. 1, 85748 Garching, Germany

¹³³ Laboratoire Univers et Théorie, Observatoire de Paris, Université PSL, Université Paris Cité, CNRS, 92190 Meudon, France

¹³⁴ Departamento de Física Fundamental, Universidad de Salamanca, Plaza de la Merced s/n, 37008 Salamanca, Spain

¹³⁵ Instituto de Astrofísica de Canarias (IAC); Departamento de Astrofísica, Universidad de La Laguna (ULL), 38200, La Laguna, Tenerife, Spain

¹³⁶ Center for Data-Driven Discovery, Kavli IPMU (WPI), UTIAS, The University of Tokyo, Kashiwa, Chiba 277-8583, Japan

¹³⁷ Ludwig-Maximilians-University, Schellingstrasse 4, 80799 Munich, Germany

¹³⁸ Max-Planck-Institut für Physik, Boltzmannstr. 8, 85748 Garching, Germany

¹³⁹ Dipartimento di Fisica - Sezione di Astronomia, Università di Trieste, Via Tiepolo 11, 34131 Trieste, Italy

¹⁴⁰ California Institute of Technology, 1200 E California Blvd, Pasadena, CA 91125, USA

¹⁴¹ University of California, Los Angeles, CA 90095-1562, USA

¹⁴² Department of Physics & Astronomy, University of California Irvine, Irvine CA 92697, USA

¹⁴³ Departamento Física Aplicada, Universidad Politécnica de Cartagena, Campus Muralla del Mar, 30202 Cartagena, Murcia, Spain

¹⁴⁴ Instituto de Física de Cantabria, Edificio Juan Jordá, Avenida de los Castros, 39005 Santander, Spain

¹⁴⁵ Observatorio Nacional, Rua General Jose Cristino, 77-Bairro Imperial de Sao Cristovao, Rio de Janeiro, 20921-400, Brazil

¹⁴⁶ Institute of Cosmology and Gravitation, University of Portsmouth, Portsmouth PO1 3FX, UK

¹⁴⁷ Department of Computer Science, Aalto University, PO Box 15400, Espoo, FI-00 076, Finland

¹⁴⁸ Instituto de Astrofísica de Canarias, c/ Via Lactea s/n, La Laguna 38200, Spain. Departamento de Astrofísica de la Universidad de La Laguna, Avda. Francisco Sanchez, La Laguna, 38200, Spain

¹⁴⁹ Ruhr University Bochum, Faculty of Physics and Astronomy, Astronomical Institute (AIRUB), German Centre for Cosmological Lensing (GCCL), 44780 Bochum, Germany

¹⁵⁰ Department of Physics and Astronomy, Vesilinnantie 5, University of Turku, 20014 Turku, Finland

¹⁵¹ Serco for European Space Agency (ESA), Camino bajo del Castillo, s/n, Urbanizacion Villafranca del Castillo, Villanueva de la Cañada, 28692 Madrid, Spain

¹⁵² ARC Centre of Excellence for Dark Matter Particle Physics, Melbourne, Australia

¹⁵³ Centre for Astrophysics & Supercomputing, Swinburne University of Technology, Hawthorn, Victoria 3122, Australia

¹⁵⁴ DAMTP, Centre for Mathematical Sciences, Wilberforce Road, Cambridge CB3 0WA, UK

¹⁵⁵ Kavli Institute for Cosmology Cambridge, Madingley Road, Cambridge, CB3 0HA, UK

¹⁵⁶ Department of Astrophysics, University of Zurich, Winterthurerstrasse 190, 8057 Zurich, Switzerland

¹⁵⁷ Department of Physics, Centre for Extragalactic Astronomy, Durham University, South Road, Durham, DH1 3LE, UK

¹⁵⁸ IRFU, CEA, Université Paris-Saclay 91191 Gif-sur-Yvette Cedex, France

¹⁵⁹ Oskar Klein Centre for Cosmoparticle Physics, Department of Physics, Stockholm University, Stockholm, SE-106 91, Sweden

¹⁶⁰ Astrophysics Group, Blackett Laboratory, Imperial College London, London SW7 2AZ, UK

¹⁶¹ Univ. Grenoble Alpes, CNRS, Grenoble INP, LPSC-IN2P3, 53, Avenue des Martyrs, 38000, Grenoble, France

¹⁶² INAF-Osservatorio Astrofisico di Arcetri, Largo E. Fermi 5, 50125, Firenze, Italy

¹⁶³ Dipartimento di Fisica, Sapienza Università di Roma, Piazzale Aldo Moro 2, 00185 Roma, Italy

¹⁶⁴ Centro de Astrofísica da Universidade do Porto, Rua das Estrelas, 4150-762 Porto, Portugal

¹⁶⁵ HE Space for European Space Agency (ESA), Camino bajo del Castillo, s/n, Urbanizacion Villafranca del Castillo, Villanueva de la Cañada, 28692 Madrid, Spain

¹⁶⁶ Theoretical astrophysics, Department of Physics and Astronomy, Uppsala University, Box 516, 751 37 Uppsala, Sweden

¹⁶⁷ Mathematical Institute, University of Leiden, Einsteinweg 55, 2333 CA Leiden, The Netherlands

¹⁶⁸ Institute of Astronomy, University of Cambridge, Madingley Road, Cambridge CB3 0HA, UK

¹⁶⁹ Department of Astrophysical Sciences, Peyton Hall, Princeton University, Princeton, NJ 08544, USA

¹⁷⁰ Space physics and astronomy research unit, University of Oulu, Pentti Kaiteran katu 1, FI-90014 Oulu, Finland

¹⁷¹ Center for Computational Astrophysics, Flatiron Institute, 162 5th Avenue, 10010, New York, NY, USA

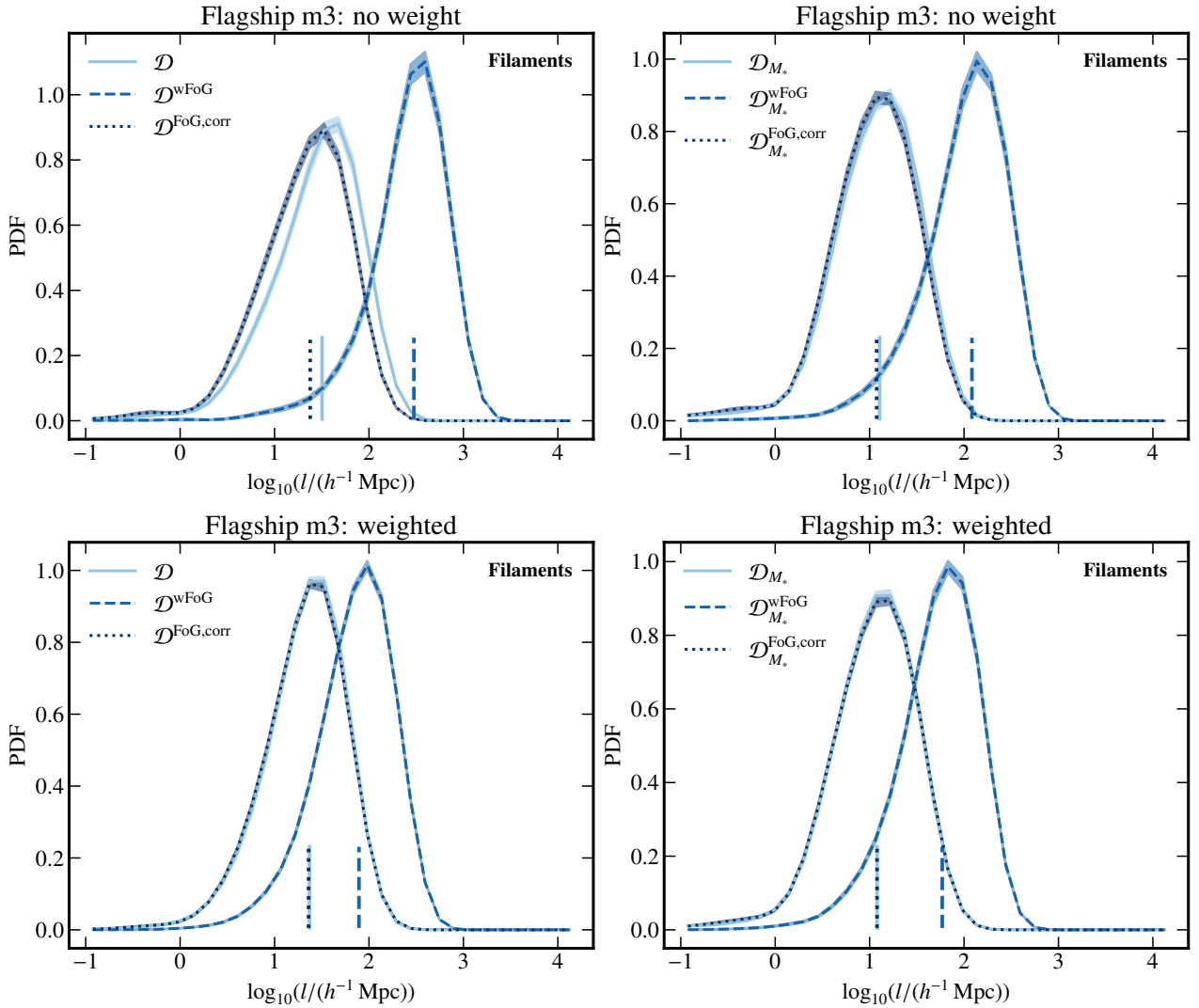


Fig. A.1. PDF of filament lengths for H α - (left) and stellar mass-limited (right) samples. Top and bottom panels compare non-weighted and weighted tessellations, respectively, for the Flagship m3 model. Vertical lines indicate the medians of distributions. Shaded regions correspond to the bootstrap error bars. For the stellar mass-limited galaxy sample, weighting of the Delaunay tessellation for the cosmic web reconstruction is not required to obtain a good agreement for the distribution of filaments' length.

Appendix A: The cosmic web statistics

Figure A.1 illustrates the effect of the selection function of galaxies and the mass weighting of the Delaunay tessellation on the distribution of filament lengths in the Flagship m3 model (see Fig. A.2 for the GAEA ECLH model with weighting). For the H α -limited samples (left panels), weighting of the tessellation by stellar mass is necessary to correct for the FoG effect (compare the top left and bottom left panels). For a M_* -limited sample (right panels), weighting is not needed to obtain a good agreement for the distribution of filaments' length after correcting for the FoG effect (compare top right and middle right panels). This behaviour is recovered in all models used in this work.

Figure A.3 highlights the effect of the reduced sampling on the distribution of filament lengths. As expected, reduced sampling (60%, as estimated for the EDF) shifts the distribution of lengths of filaments to higher values, regardless of sample selection (H α - and M_* -limited sample, left and right panels, respectively).

Appendix B: Connectivity and multiplicity

Figure B.1 shows the PDFs of the connectivity of central galaxies for M_* - limited selection of galaxies in the full sample without redshift error (\mathcal{D}) for Flagship (model m3, top panels) and GAEA (model ECLH, bottom panels), with stellar mass weighting of the Delaunay tessellation (left) and without weighting (right). The stellar mass weighting impacts the PDF of the connectivity to a much lesser degree when the galaxy sample is M_* -limited compared to an H α -limited selection. After correcting for the FoG effect, the shape of the distributions and their medians (vertical lines) are in very good agreement with the measurements in the absence of redshift-space distortions without tessellation weighting for both Flagship and GAEA. Stellar mass weighting introduces some spurious effects, preventing us from completely correcting for the FoG effect in GAEA. However, the distribution of the connectivity

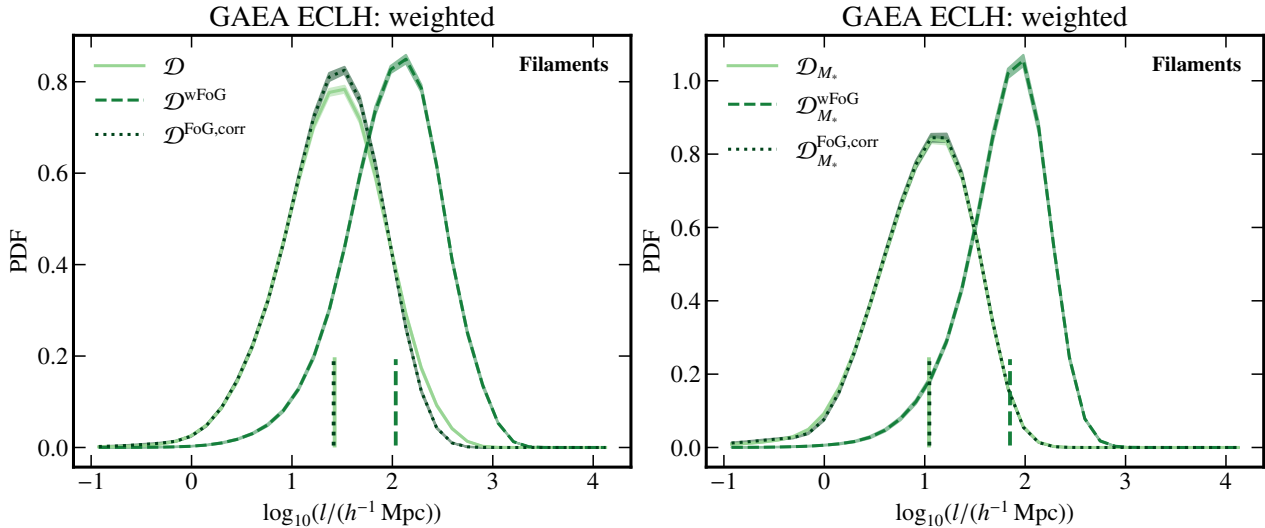


Fig. A.2. As in Fig. A.1, bottom panels, i.e. using the stellar mass-weighted tessellation for the cosmic web reconstruction, but for the GAEA ECLH model.

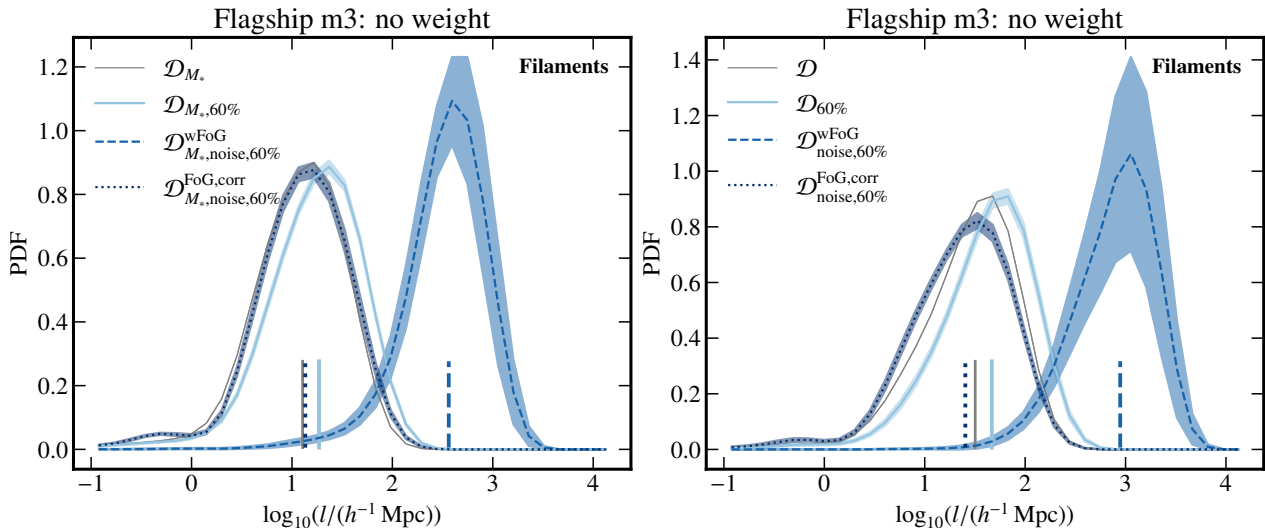


Fig. A.3. PDF of filaments' length for stellar mass- (left) and $H\alpha$ -limited (right) samples with 60% sampling.

and its median are substantially improved. The mean and median values of connectivity for all mocks and selections are reported in Tables B.1 and B.2.

Regarding the multiplicity, in general, PDFs of the multiplicity and their median values are only weakly impacted by the FoG effect when stellar mass-weighted tessellation is used for cosmic web extraction. Without weighting, the applied FoG compression efficiently corrects for the redshift-space distortion for the distribution of the multiplicity and its median value. These conclusions apply to all tested models (i.e., including M_* -limited samples). The mean and median values of multiplicity for all mocks and selections are reported in Tables B.3 and B.4.

Figure B.2 illustrates the mean connectivity of central galaxies as a function of their stellar mass in the model m3 of the Flagship (left) and model ECLH of GAEA (right) for M_* -limited samples with reduced sampling and redshift uncertainties ($D_{noise,60\%}$) with tessellation weighting, but qualitatively similar results are obtained without weighting. Regardless of weighting, the FoG effect increases the connectivity by an order of magnitude at all stellar masses. The method used to correct for the small-scale redshift-space distortions helps bring the connectivity close to the values obtained for the sample without FoG. Weighting the tessellation for the M_* -limited sample does not seem to introduce the bias seen for the selection of galaxies based on their $H\alpha$ flux, that is the increasing connectivity at low stellar masses. Similar conclusions apply to all other models.

Figure B.3 shows the mean multiplicity of central galaxies as a function of their stellar mass in the model m3 of Flagship (left) and model ECLH of GAEA (right) for M_* -limited samples with reduced sampling and redshift uncertainties ($D_{noise,60\%}$) with tessellation weighting, but qualitatively similar results are found without weighting. The multiplicity appears to be a more robust quantity than the connectivity, given that the FoG effect has an overall much weaker impact on its values, in particular when the tessellation is weighted by stellar mass.

Figure B.4 shows the multiplicity of central galaxies as a function of their stellar mass for the Flagship and GAEA mocks (models m3 and ECLH, respectively, with qualitatively similar conclusions for m1 and ECLQ) for the fiducial sample ($D_{noise,60\%}$)

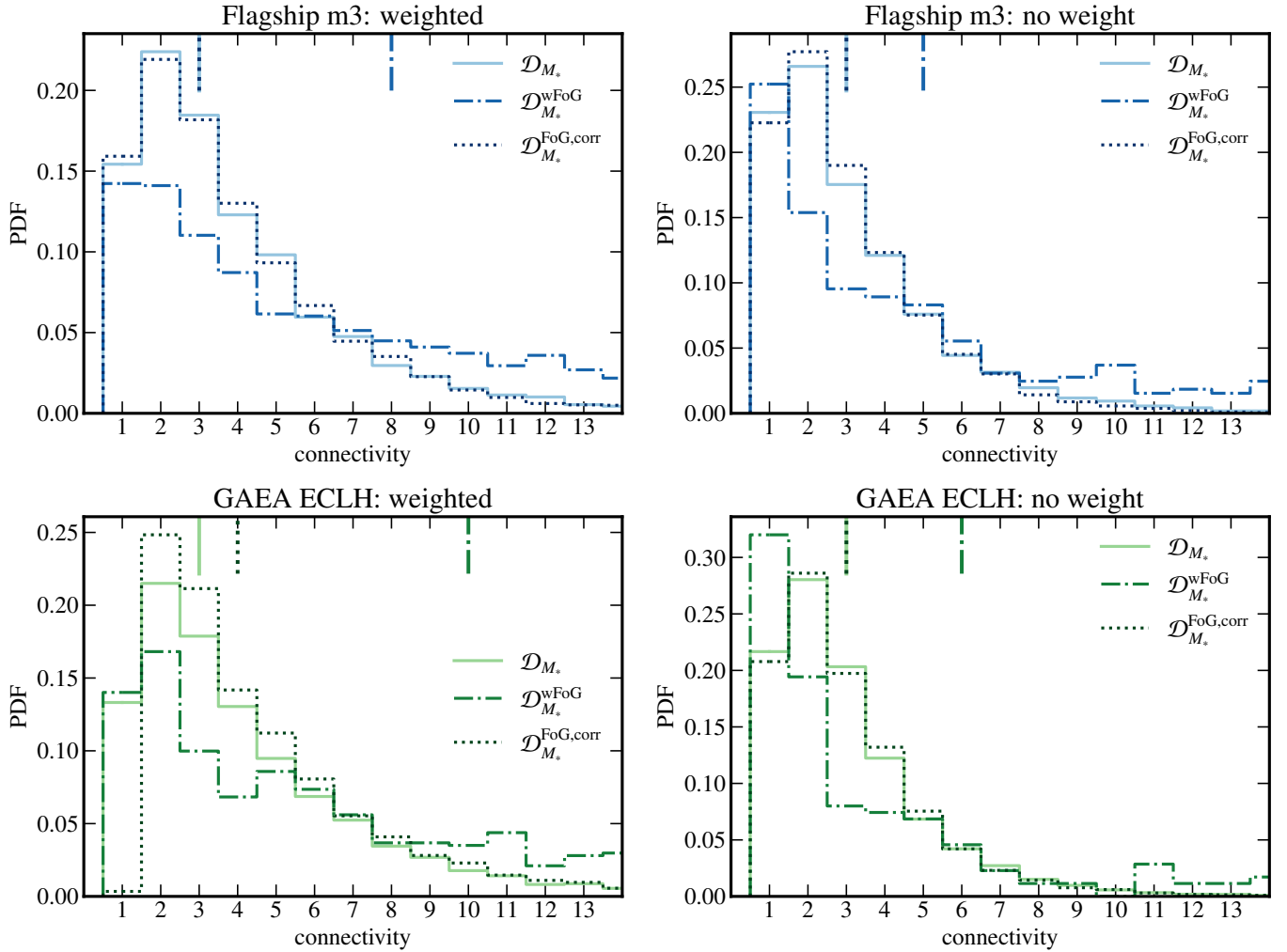


Fig. B.1. As in Fig. 9, but for the M_* -limited galaxy selection. The mean and median values for all distributions are reported in Tables B.1 and B.2.

without stellar mass-weighted tessellation. The multiplicity of central galaxies increases with increasing stellar mass for galaxies in all reference catalogues (\mathcal{D}), catalogues with reduced sampling and redshift uncertainties ($\mathcal{D}_{\text{noise},60\%}$). The applied FoG correction significantly improves our ability to recover the M_* -multiplicity relation.

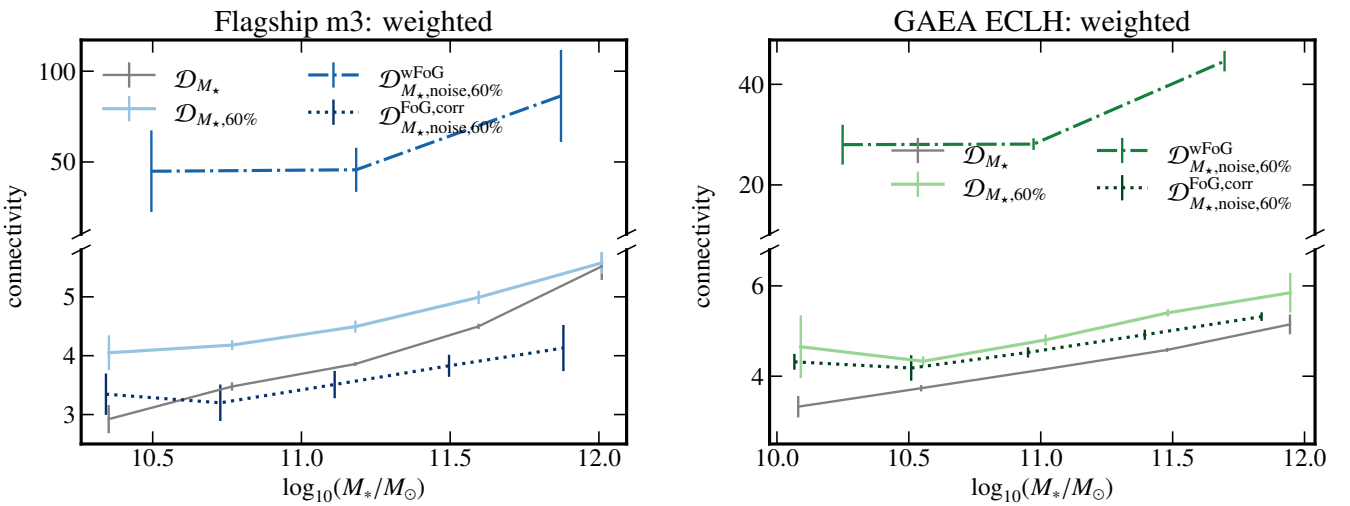


Fig. B.2. Connectivity of central galaxies as a function of their stellar mass in the Flagship (model m3) and GAEA (model ECLH) mocks, right and left panels, respectively, for M_* -limited samples ($\mathcal{D}_{M_*,\text{noise},60\%}$), with M_* -weighted tessellation (qualitatively similar results are obtained without weighting).

Table B.1. Median and mean connectivity for the Flagship m3 and Flagship m1 mocks, for tessellations with and without stellar mass weighting.

	Flagship m3				Flagship m1			
	median		mean		median		mean	
	no weight	weight	no weight	weight	no weight	weight	no weight	weight
\mathcal{D}	3	8	4.95 ± 0.11	10.94 ± 0.17	3	7	4.52 ± 0.06	10.07 ± 0.11
$\mathcal{D}^{\text{wFoG}}$	6	19	50.60 ± 9.31	58.54 ± 3.8	6.5	17	48.83 ± 7.51	53.12 ± 2.47
$\mathcal{D}^{\text{FoG,corr}}$	3	7	4.15 ± 0.06	10.95 ± 0.18	3	7	3.79 ± 0.04	10.55 ± 0.12
\mathcal{D}_{M_*}	3	3	3.18 ± 0.03	3.99 ± 0.03	3	3	3.19 ± 0.02	4.24 ± 0.03
$\mathcal{D}_{M_*}^{\text{wFoG}}$	5	8	17.12 ± 1.49	16.64 ± 0.72	5	8	18.19 ± 1.45	18.51 ± 0.67
$\mathcal{D}_{M_*}^{\text{FoG,corr}}$	3	3	3.04 ± 0.02	3.93 ± 0.03	2	3	2.96 ± 0.02	4.21 ± 0.03
$\mathcal{D}_{60\%}$	4	9	5.51 ± 0.45	14.56 ± 0.87	3	8	5.03 ± 0.29	12.96 ± 0.53
$\mathcal{D}_{\text{noise},60\%}^{\text{wFoG}}$	32	99	160.71 ± 247.66	282.84 ± 156.16	24	86	153.18 ± 270.71	275.60 ± 139.61
$\mathcal{D}_{\text{noise},60\%}^{\text{FoG,corr}}$	3	8	3.25 ± 0.14	13.87 ± 0.81	2	8	2.95 ± 0.09	13.26 ± 0.57
$\mathcal{D}_{M_*,60\%}$	3	4	3.40 ± 0.11	4.62 ± 0.14	3	4	3.38 ± 0.09	5.02 ± 0.12
$\mathcal{D}_{M_*,\text{noise},60\%}^{\text{wFoG}}$	10.5	23.5	46.30 ± 27.75	56.03 ± 23.76	13	28	62.97 ± 50.37	80.22 ± 26.05
$\mathcal{D}_{M_*,\text{noise},60\%}^{\text{FoG,corr}}$	2	3	2.68 ± 0.15	3.64 ± 0.22	2	3	2.59 ± 0.11	4.15 ± 0.19

Table B.2. Median and mean connectivity for the GAEA ECLH and GAEA ECLQ mocks, for tessellations with and without stellar mass weighting.

	GAEA ECLH				GAEA ECLQ			
	median		mean		median		mean	
	no weight	weight	no weight	weight	no weight	weight	no weight	weight
\mathcal{D}	5	11	8.20 ± 0.38	19.09 ± 0.44	6	16	14.97 ± 1.37	34.07 ± 1.45
$\mathcal{D}^{\text{wFoG}}$	3	18	116.33 ± 32.70	129.37 ± 13.09	3	18	128.77 ± 50.96	164.69 ± 20.19
$\mathcal{D}^{\text{FoG,corr}}$	4	11	5.43 ± 0.12	19.24 ± 0.40	5	19	7.75 ± 0.26	37.27 ± 1.19
\mathcal{D}_{M_*}	3	3	3.05 ± 0.02	4.26 ± 0.03	3	4	3.13 ± 0.02	5.21 ± 0.04
$\mathcal{D}_{M_*}^{\text{wFoG}}$	6	10	30.66 ± 4.06	27.13 ± 1.41	8	11	33.85 ± 4.36	35.67 ± 2.26
$\mathcal{D}_{M_*}^{\text{FoG,corr}}$	3	4	3.04 ± 0.02	4.73 ± 0.03	3	4	3.08 ± 0.02	5.18 ± 0.04
$\mathcal{D}_{60\%}$	5	13	9.31 ± 1.61	25.25 ± 2.50	7	19	17.84 ± 6.21	46.69 ± 7.49
$\mathcal{D}_{\text{noise},60\%}^{\text{wFoG}}$	145	253.5	495.88 ± 486.04	852.72 ± 944.33	33	126	616.36 ± 1460.80	1340.72 ± 1704.38
$\mathcal{D}_{\text{noise},60\%}^{\text{FoG,corr}}$	3	14	3.61 ± 0.21	26.30 ± 1.94	3	20	4.18 ± 0.32	43.05 ± 4.45
$\mathcal{D}_{M_*,60\%}$	3	4	3.28 ± 0.10	5.02 ± 0.15	3	5	3.41 ± 0.12	6.55 ± 0.24
$\mathcal{D}_{M_*,\text{noise},60\%}^{\text{wFoG}}$	7	12	35.57 ± 12.73	33.81 ± 5.95	7	12	36.59 ± 14.23	42.94 ± 9.00
$\mathcal{D}_{M_*,\text{noise},60\%}^{\text{FoG,corr}}$	3	4	3.14 ± 0.10	4.71 ± 0.16	3	4	3.20 ± 0.12	5.90 ± 0.25

Appendix C: Stellar-mass gradients

Figure C.1 shows the PDFs of the distances of galaxies to their closest filament for the Flagship m1 model (the results for the Flagship m3 and GAEA models are comparable) and for the reconstruction of the cosmic web with weighting the tessellation as a function of stellar mass and redshift, for H α flux-limited sample with reduced sampling ($\mathcal{D}_{60\%}$, first row) and when redshift error and FoG are added ($\mathcal{D}_{\text{noise},60\%}^{\text{wFoG}}$, second row). Stellar-mass gradients, with more massive galaxies located closer to the filaments than their lower mass counterparts, present in the reference H α flux-limited sample are recovered.

Figure C.2 shows the PDFs of the distances of galaxies to their closest filament for the Flagship m1 model (the results for the Flagship m3 and GAEA models are comparable) and for the reconstruction of the cosmic web without weighting the tessellation as a function of stellar mass and redshift. The distances are normalised by the mean intergalactic separation to take into account the effect of decreasing the density of galaxies with increasing redshift.

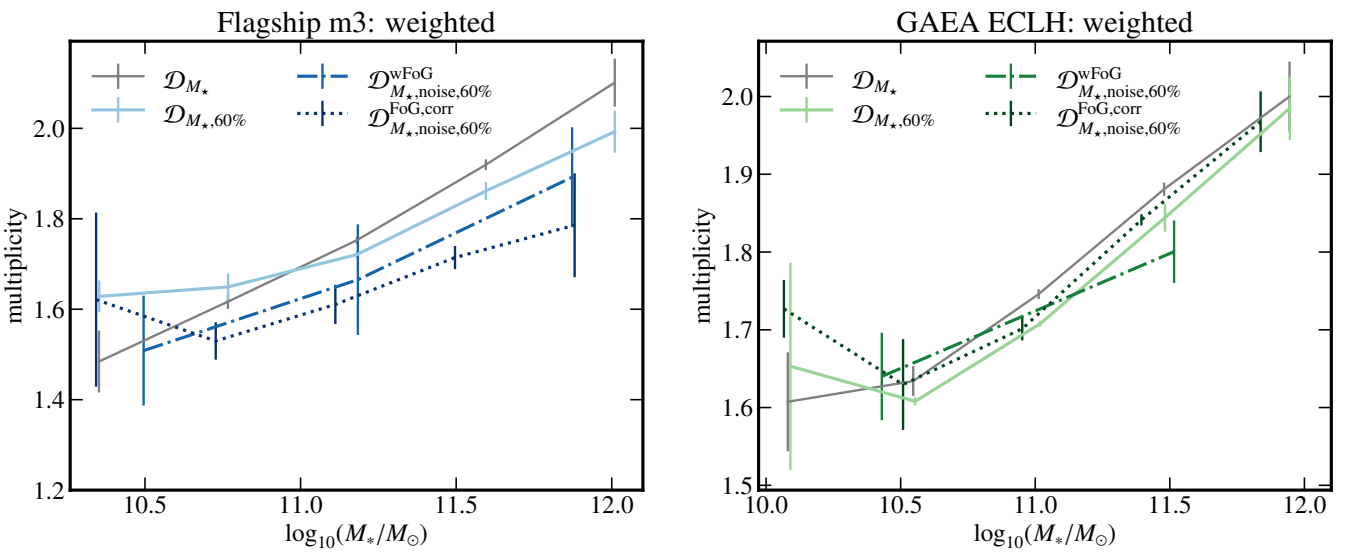
The first row shows the PDFs for the reference sample (\mathcal{D}), while the second row shows the PDFs after correction of the FoG effect ($\mathcal{D}_{\text{noise},60\%}^{\text{FoG,corr}}$). When the cosmic web is reconstructed without weighting the Delaunay tessellation, reduced galaxy sampling tends to decrease the stellar mass gradient signal (not shown), as in the case of the reconstruction including the weighting. Redshift errors have the strongest impact, by significantly reducing our ability to recover the stellar-mass gradients towards filaments of the cosmic web (not shown). Correcting for the FoG effect only mildly improves the signal.

Table B.3. Median and mean multiplicity for the Flagship m3 and Flagship m1 mocks, for tessellations with and without stellar mass weighting.

	Flagship m3				Flagship m1			
	median		mean		median		mean	
	no weight	weight	no weight	weight	no weight	weight	no weight	weight
\mathcal{D}	2	2	1.58 ± 0.01	2.03 ± 0.01	2	2	1.62 ± 0.01	2.07 ± 0.01
$\mathcal{D}^{\text{wFoG}}$	1	2	1.48 ± 0.06	2.07 ± 0.03	1	2	1.48 ± 0.04	2.13 ± 0.02
$\mathcal{D}^{\text{FoG,corr}}$	2	2	1.62 ± 0.01	2.04 ± 0.01	2	2	1.62 ± 0.01	2.07 ± 0.01
\mathcal{D}_{M_*}	2	2	1.62 ± 0.01	1.78 ± 0.01	2	2	1.63 ± 0.01	1.81 ± 0.01
$\mathcal{D}_{M_*}^{\text{wFoG}}$	1	2	1.55 ± 0.03	1.77 ± 0.02	1	2	1.52 ± 0.03	1.83 ± 0.02
$\mathcal{D}_{M_*}^{\text{FoG,corr}}$	2	2	1.65 ± 0.01	1.79 ± 0.01	2	2	1.63 ± 0.01	1.83 ± 0.01
$\mathcal{D}_{60\%}$	1	2	1.56 ± 0.05	2.02 ± 0.04	1	2	1.58 ± 0.04	2.06 ± 0.03
$\mathcal{D}_{\text{noise,60\%}}^{\text{wFoG}}$	1	2	1.57 ± 0.64	2.07 ± 0.25	1	2	1.29 ± 0.35	2.19 ± 0.18
$\mathcal{D}_{\text{noise,60\%}}^{\text{FoG,corr}}$	1	2	1.52 ± 0.04	1.97 ± 0.04	1	2	1.51 ± 0.03	2.04 ± 0.03
$\mathcal{D}_{M_*,60\%}$	2	2	1.59 ± 0.03	1.76 ± 0.03	2	2	1.59 ± 0.02	1.80 ± 0.02
$\mathcal{D}_{M_*,\text{noise,60\%}}^{\text{wFoG}}$	1	2	1.53 ± 0.27	1.74 ± 0.16	1.5	2	1.55 ± 0.27	1.91 ± 0.14
$\mathcal{D}_{M_*,\text{noise,60\%}}^{\text{FoG,corr}}$	1	2	1.56 ± 0.06	1.66 ± 0.05	1	2	1.53 ± 0.04	1.71 ± 0.04

Table B.4. Median and mean multiplicity for the GAEA ECLH and GAEA ECLQ mocks, for tessellations with and without stellar mass weighting.

	GAEA ECLH				GAEA ECLQ			
	median		mean		median		mean	
	no weight	weight	no weight	weight	no weight	weight	no weight	weight
\mathcal{D}	2	2	1.69 ± 0.02	2.21 ± 0.01	2	2	1.61 ± 0.03	2.22 ± 0.02
$\mathcal{D}^{\text{wFoG}}$	1	2	1.36 ± 0.07	2.07 ± 0.04	1	2	1.28 ± 0.07	2.08 ± 0.04
$\mathcal{D}^{\text{FoG,corr}}$	2	2	1.61 ± 0.01	2.14 ± 0.01	2	2	1.62 ± 0.02	2.19 ± 0.02
\mathcal{D}_{M_*}	2	2	1.66 ± 0.01	1.78 ± 0.01	2	2	1.65 ± 0.01	1.80 ± 0.01
$\mathcal{D}_{M_*}^{\text{wFoG}}$	1	2	1.46 ± 0.04	1.78 ± 0.02	1	2	1.54 ± 0.04	1.79 ± 0.03
$\mathcal{D}_{M_*}^{\text{FoG,corr}}$	2	2	1.67 ± 0.01	1.80 ± 0.01	2	2	1.67 ± 0.01	1.85 ± 0.01
$\mathcal{D}_{60\%}$	2	2	1.64 ± 0.07	2.17 ± 0.05	2	2	1.59 ± 0.11	2.15 ± 0.07
$\mathcal{D}_{\text{noise,60\%}}^{\text{wFoG}}$	1	2	1.50 ± 0.81	2.18 ± 0.33	1	2	1.28 ± 0.63	2.15 ± 0.46
$\mathcal{D}_{\text{noise,60\%}}^{\text{FoG,corr}}$	1	2	1.49 ± 0.04	2.10 ± 0.05	1	2	1.47 ± 0.05	2.05 ± 0.06
$\mathcal{D}_{M_*,60\%}$	2	2	1.60 ± 0.03	1.76 ± 0.02	2	2	1.60 ± 0.03	1.80 ± 0.03
$\mathcal{D}_{M_*,\text{noise,60\%}}^{\text{wFoG}}$	1	2	1.43 ± 0.11	1.76 ± 0.08	1	2	1.50 ± 0.13	1.81 ± 0.09
$\mathcal{D}_{M_*,\text{noise,60\%}}^{\text{FoG,corr}}$	2	2	1.63 ± 0.03	1.77 ± 0.03	2	2	1.62 ± 0.04	1.81 ± 0.04

**Fig. B.3.** Multiplicity of central galaxies as a function of their stellar mass in Flagship (model m3) and GAEA (model ECLH) mocks, left and right panels, respectively, for M_* -limited samples ($\mathcal{D}_{M_*,\text{noise,60\%}}$), with M_* -weighted tessellation (qualitatively similar results are obtained without weighting).

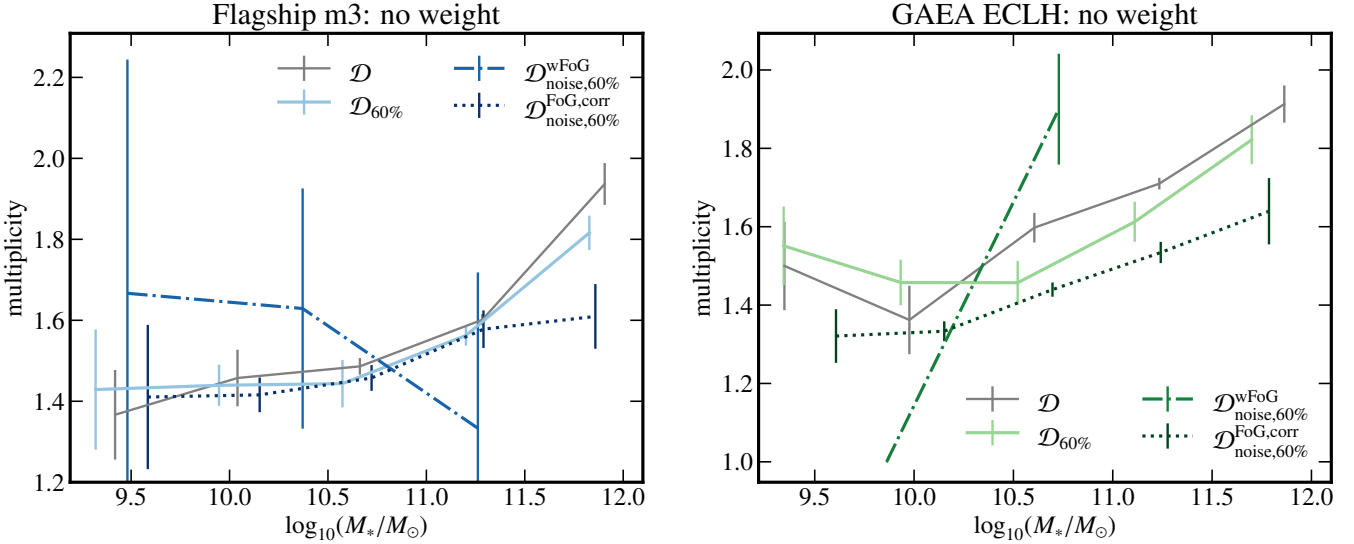


Fig. B.4. As in Fig. 13 but without stellar mass weighting of the skeleton.

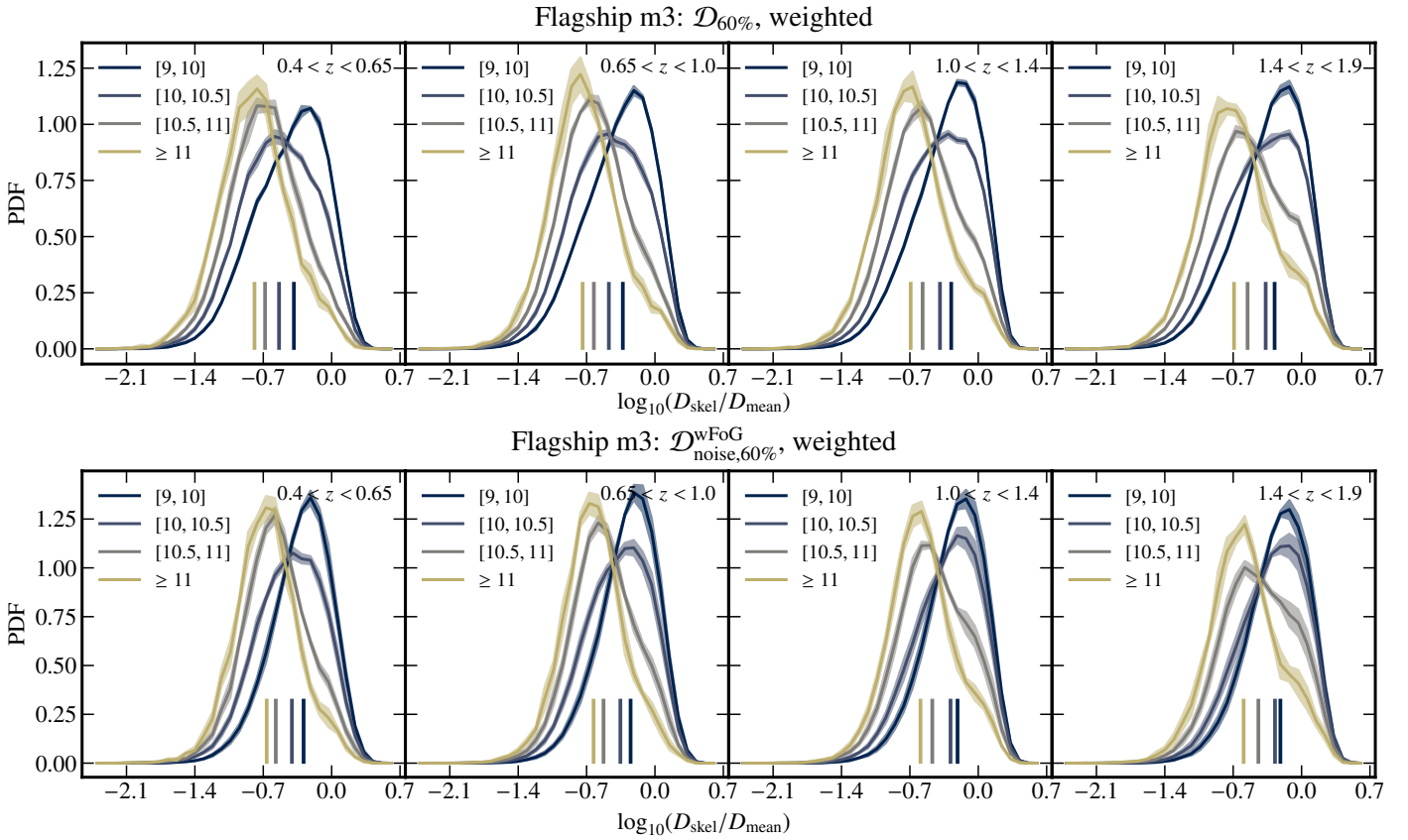


Fig. C.1. As in Fig. 14, but for a catalogue with reduced sampling ($\mathcal{D}_{60\%}$, first row) and with added redshift error and FoG ($\mathcal{D}_{noise,60\%}^{WFoG}$, second row). Stellar-mass gradients are recovered in all configurations.

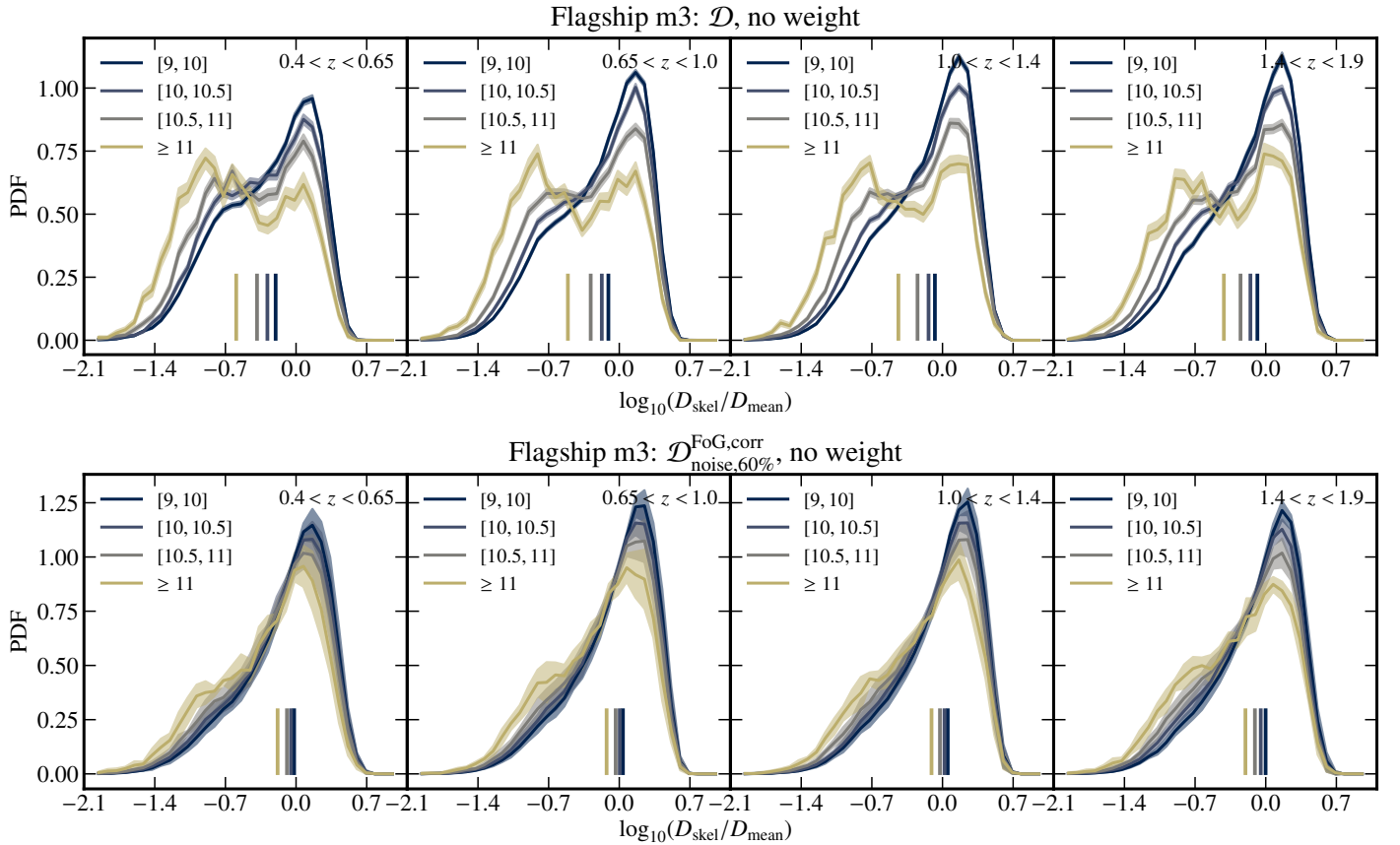


Fig. C.2. As in Fig. 14, but for the reconstruction without stellar mass-weighted Delaunay tessellation. The error on redshift in combination with the redshift-space distortions strongly reduce the stellar-mass gradients, that are only slightly improved after the correction of the FoG effect.